

Computational Methods for the Measurement of Entanglement in Condensed Matter Systems

by

Ann Berlinsky Kallin

A thesis
presented to the University of Waterloo
in fulfillment of the
thesis requirement for the degree of
Doctor of Philosophy
in
Physics

Waterloo, Ontario, Canada, 2014

© Ann Berlinsky Kallin 2014

I hereby declare that I am the sole author of this thesis. This is a true copy of the thesis, including any required final revisions, as accepted by my examiners.

I understand that my thesis may be made electronically available to the public.

Abstract

At the interface of quantum information and condensed matter physics, the study of entanglement in quantum many-body systems requires a new toolset which combines concepts from each. This thesis introduces a set of computational methods to study phases and phase transitions in lattice models of quantum systems, using the Renyi entropies as a means of quantifying entanglement. The scaling of entanglement entropy can give valuable insight into the phase of a condensed matter system. It can be used to detect exotic types of phases, to pinpoint transitions between phases, and can give us universal information about a system.

The first approach in this thesis is a technique to measure entanglement in finite size lattice systems using zero-temperature quantum Monte Carlo simulations. The algorithm is developed, implemented, and used to explore anomalous entanglement scaling terms in the spin- $\frac{1}{2}$ Heisenberg antiferromagnet.

In the second part of this thesis, a new and complementary numerical technique is introduced to study entanglement not just in finite size systems, but as we approach the thermodynamic limit. This “numerical linked-cluster expansion” is used to study two different systems at their quantum critical points — continuous phase transitions occurring at zero temperature, at which these systems exhibit universal properties. Remarkably, these universal properties can be reflected in the scaling of entanglement.

Entanglement offers a new perspective on condensed matter systems, one which takes us closer to genuinely understanding what goes on in these materials at the quantum mechanical level. This thesis demonstrates the first steps in developing an extensive list of computational tools that can be used to study entanglement over a wide range of interacting quantum many-body systems. With the ever increasing computational power available, it may be only a matter of time before these tools are used to create a comprehensive framework for the characterization of condensed matter phases and phase transitions.

Acknowledgements

I would like to thank all those who have helped me along the way in the ~ 2000 days since I began my graduate studies at the University of Waterloo: My supervisor, Roger Melko, who consistently puts the welfare of his students first. My committee members throughout the years from uWaterloo Physics, Chemistry, and Computer Science, as well as the Perimeter Institute and the Institute for Quantum Computing. The Physics Department office staff, my fellow physics graduate students, post-docs, conference and summer school roommates, adopted Santa Barbara research groupmates, collaborators from around the world, teammates (Spin Ice, The Jason Iaconis Experience, PI Monday morning league, etc.), the PI post-docs and faculty and staff, and past and current members of the Melko Collective. A special thanks to my eldest physics brother and fellow first graduate student, Stephen, the only other person to experience the same experimental supervising techniques. Thanks to the City of Waterloo for having a population that is interested in and excited about of physics, as well as such a large concentration of well maintained ice rinks. Thanks to Lori, who has shown me all the best parts of Waterloo, including where to find enough Saskatoon berries to last the winter. Finally, I would like to thank my incredibly supportive parents.

Dedication

This work is dedicated to my parents, Catherine Kallin and A. John Berlinsky, who together provide the perfect balance of inspiration, encouragement, and levelheadedness.

Table of Contents

List of Tables	ix
List of Figures	x
1 Introduction	1
1.1 Entanglement	3
1.2 Lattice Models in Condensed Matter	9
1.2.1 Quantum Critical Points	9
1.2.2 The Heisenberg Model	9
1.2.3 The Heisenberg Bilayer	12
1.2.4 The Transverse-Field Ising Model	13
1.3 Entanglement Scaling in Condensed Matter Systems	15
1.3.1 One Dimension	16
1.3.2 Two Dimensions	16
1.4 Tensor Diagram Notation	20
1.5 Extracting Entanglement Entropy from the groundstate wavefunction . . .	25
2 Valence Bond Projector Quantum Monte Carlo	28
2.1 Review of Valence Bond quantum Monte Carlo	29
2.2 The Loop Algorithm	31
2.2.1 Algorithm	33

2.2.2	Measurements	34
2.3	Measuring Renyi Entanglement Entropies with VB QMC	34
2.3.1	Renyi Entanglement Entropies and the “Replica Trick”	35
2.3.2	The Ratio Trick	38
2.4	The Loop-Ratio Algorithm	40
2.5	Anomalies in the Entanglement Properties of the Square Lattice Heisenberg Model	40
2.5.1	Results	42
2.5.2	Discussion	53
3	Numerical Linked-Cluster Expansion	55
3.1	Relation to High-Temperature Series Expansion	56
3.2	Linked-Cluster Expansions	58
3.3	Clusters	59
3.3.1	Inclusion-Exclusion	60
3.3.2	The Lattice Constant	60
3.3.3	General Clusters	61
3.3.4	Rectangular Clusters	65
3.3.5	Definition of Order	67
3.4	Measuring Entanglement	70
3.5	NLCE Cluster Solvers	77
3.5.1	Lanczos & Full Diagonalization	77
3.5.2	Density Matrix Renormalization Group	78
3.5.3	Quantum Monte Carlo	80
3.6	NLCE in One Dimension	81
3.7	Convergence	82
3.7.1	Finite Size Scaling of Results	82
3.8	The Computational Process	82

3.9	Entanglement Scaling at Quantum Critical Points	85
3.9.1	The Transverse Field Ising Model	86
3.9.2	The Heisenberg Bilayer	92
3.9.3	Discussion	99
3.9.4	Future Work	101
4	Conclusions	103
	References	105

List of Tables

1.1	Energies of 2-spin states for the Heisenberg antiferromagnet	11
2.1	A comparison of the energies for $\mathcal{H}_{\text{Heis}}$ and $\mathcal{H}_{\text{proj}}$	30
2.2	The coefficients from fitting $S_2/\ell = a + \frac{b}{\ell} \log \ell + d/\ell$	48
3.1	The properties and subclusters of clusters up to 4×4	59
3.2	The different definitions of cluster order and length-scale for clusters of up to 4×4	67

List of Figures

1.1	S_α between 2 entangled spins for a range of α from 0.001 to 1000	7
1.2	A $4 \times 4 \times 2$ bilayer lattice	13
1.3	Lattices divided into two regions with an entanglement boundary	15
1.4	Intuition for the area law	19
1.5	Intuition for the corner log	21
2.1	Simulation cell for the loop algorithm.	32
2.2	A 2D view of the loop-ratio simulation cell	41
2.3	A 3D view of the loop-ratio simulation cell	42
2.4	The strip & square region A geometries used to study S_2	43
2.5	Convergence in the number of operators for the VB QMC	44
2.6	The area law and aspect ratio dependence in the 2D Heisenberg model	46
2.7	S_2/ℓ for the Heisenberg model using square and strip region A 's.	47
2.8	Heisenberg Renyi-bows	50
2.9	Heisenberg Renyi-bows plotted using chord length	51
2.10	The coefficient of the shape dependence term for a torus	52
3.1	Illustration of clusters with different lattice constants.	60
3.2	Number of possible clusters on a square lattice	62
3.3	Plots comparing all clusters to rectangular clusters.	65
3.4	Visualizing arithmetic orders using diamonds	68

3.5	Method 1 to visualize the different orders for clusters.	71
3.6	Method 2 to visualize the different orders for clusters	72
3.7	Method 2 in more detail.	73
3.8	Entanglement cuts for the corner term	74
3.9	Entanglement cuts for the corner term	75
3.10	DMRG paths for entanglement measurements	79
3.11	NLCE flowchart.	84
3.12	Line and Corner terms for TFIM.	86
3.13	Corner terms c_α for TFIM.	88
3.14	Corner coefficient for TFIM for different orders	90
3.15	Corner coefficient for TFIM compared with other techniques	91
3.16	The bilayer energy per site at its critical point	93
3.17	Bilayer corner coefficient - Fits for c_α	95
3.18	Bilayer corner coefficient - Convergence in \mathcal{O}_G	96
3.19	Bilayer corner coefficient - Convergence in \mathcal{O}_A	97
3.20	Bilayer corner coefficient	98

Chapter 1

Introduction

Entanglement is the quintessential property distinguishing quantum mechanical and classical systems. In the field of quantum information science, entanglement is used as a resource: to produce incredible speedup in quantum algorithms compared to their classical counterparts; to efficiently break classical cryptographic schemes as well as create new secure quantum encryption, and more.

Despite the importance of entanglement to quantum mechanical systems and quantum information theory, it is notoriously difficult to quantify, both in theory and experimentally. There is not one standard, but instead many possible quantities used to measure entanglement. This thesis will focus on the “entanglement entropy”, an appealing choice for a condensed matter physicist, due to its ties to Boltzmann’s thermodynamic entropy.

Entanglement is a much less familiar concept in condensed matter physics. It is not typically a part of the language used to describe phases of matter. However, increasingly, the language of entanglement has started to find its place in condensed matter theory. It was perhaps first popularized by theorists looking to detect “spin liquid” phases of matter that cannot be described by conventional symmetry breaking or long-range order [40, 44]. The concept of “long-range entanglement” was introduced to describe these quantum spin liquid phases [11, 85]. But what *is* long-range entanglement? Can one define a range for entanglement? How do we quantify these and other properties of entanglement in a condensed matter system?

Entanglement can be physically measured and manipulated with some difficulty in few-body systems. E.g., one can determine that they have pairs of entangled photons by taking a series of measurements to check that Bell’s inequality [4] is violated, but how does this translate over into macroscopic condensed matter systems? We are interested in developing

a set of tools and intuition to study the properties of entanglement in *many-body* quantum systems, such as large lattices of spins, and fortunately computational techniques give us the power to achieve this complicated task.

In this thesis, I will develop a new set of numerical tools to study entanglement scaling in condensed matter systems. I expect the study of entanglement in quantum many-body systems to experience dramatic advances in the future, both due to the development of new, innovative algorithms, like those presented in this thesis, and because of the continuing and increasing availability of high-performance computer hardware. (According to Moore’s law computing power will double every 2 years.)

The applications of this research range from a greater knowledge of the systems studied in this thesis—where unexpected entanglement properties have been found and characterized in models that many would have assumed we already knew everything there was to know about—to the creation of a new framework in condensed matter physics, where entanglement may become the more intuitive standard and complete way of describing phases. This conceptual framework of entanglement scaling, the computational techniques introduced in the following chapters, the concepts—such as the “area law” entanglement scaling, universal subleading corrections, and more—will all be critically important in efforts to fully identify and characterize phases and phase transitions of quantum materials and theories in the future.

This thesis is laid out as follows:

The remainder of this chapter will introduce concepts necessary to understand the subsequent chapters of the thesis, including: a more in-depth qualitative and quantitative explanation of entanglement, an introduction to lattice models in condensed matter (including the specific models studied in later chapters), an overview of the known properties of entanglement scaling in one and two dimensional systems, an introduction to “Tensor Diagram Notation”—a graphical language for linear algebra relations that will facilitate an understanding of many of the otherwise opaque relations needed to extract entanglement, and finally I will use this notation to show how one can extract measurements of entanglement when the system’s wavefunction is known.

Chapter 2 introduces a large-scale zero temperature quantum Monte Carlo algorithm for measuring entanglement in condensed matter systems. In terms of lattices, Monte Carlo simulations are able to reach the largest finite-sized systems out of the different numerical techniques mentioned here. This specific technique works in a basis of valence bonds instead of the standard spin states, and is used to study the entanglement scaling of the two dimensional spin- $\frac{1}{2}$ Heisenberg antiferromagnet groundstate.

Chapter 3 introduces the numerical linked-cluster expansion method, a technique which

uses results from finite size clusters to study the entanglement as a system approaches the thermodynamic limit. The NLCE is used to study a universal subleading term in the entanglement due to the presence of a corner in the entanglement boundary for two different quantum critical systems, the results of which are presented and discussed in this chapter.

Finally, Chapter 4 will contain a summary of this thesis and conclusions.

1.1 Entanglement

What *is* Entanglement?

Entanglement is a fundamentally quantum mechanical property. When two systems are entangled it is impossible to entirely capture the state of both systems by describing the states of each component separately.

We can begin by looking at spin states, for $S = \frac{1}{2}$ spins, an easy choice of qubit coming from a condensed matter background. A quantum spin- $\frac{1}{2}$ entity has complex “up” and “down” components that can be measured in any of the S^x , S^y , and S^z bases, where these S^i s are Pauli matrices multiplied by factors of $1/2$,

$$S^x = \frac{1}{2}\sigma^x = \frac{1}{2} \begin{bmatrix} 0 & 1 \\ 1 & 0 \end{bmatrix}, \quad S^y = \frac{1}{2}\sigma^y = \frac{1}{2} \begin{bmatrix} 0 & -i \\ i & 0 \end{bmatrix}, \quad S^z = \frac{1}{2}\sigma^z = \frac{1}{2} \begin{bmatrix} 1 & 0 \\ 0 & -1 \end{bmatrix}. \quad (1.1)$$

Notice that since the S^z matrix is diagonal, the standard procedure is to work in the terms of the S^z basis. An “up” spin in the S^z basis is represented by $|\uparrow\rangle = [1 \ 0]^\dagger$, and has eigenvalue $+1/2$ for the S^z operator. The spin down state is $|\downarrow\rangle = [0 \ 1]^\dagger$, and has the S^z eigenvalue $-1/2$.

Returning to entanglement, we can start with one of the simplest states of entangled spin- $\frac{1}{2}$ particles,

$$|1, 2\rangle = \frac{1}{\sqrt{2}}(|\uparrow_1\uparrow_2\rangle + |\downarrow_1\downarrow_2\rangle). \quad (1.2)$$

There are two spins labeled by 1 and 2. If we examine each spin separately (by tracing out the state of the other spin) they both have a 50% probability of being up or down,

$$|1\rangle = |2\rangle = \begin{cases} |\uparrow\rangle & 50\% \\ |\downarrow\rangle & 50\% \end{cases}. \quad (1.3)$$

But combining the states of each spin in (1.3) to get the state of both spins,

$$|1\rangle \otimes |2\rangle = \begin{cases} |\uparrow_1\uparrow_2\rangle & 25\% \\ |\uparrow_1\downarrow_2\rangle & 25\% \\ |\downarrow_1\uparrow_2\rangle & 25\% \\ |\downarrow_1\downarrow_2\rangle & 25\% \end{cases}, \quad (1.4)$$

will tell us that the spins are completely uncorrelated and there is some probability of finding the two spin states $|\uparrow_1\downarrow_2\rangle$ and $|\downarrow_1\uparrow_2\rangle$, when in fact we know that in the original state (1.2) there is *no* probability of finding the spins pointing in opposite directions. In describing the quantum mechanical state with respect to each spin separately we have lost the quantum correlation (i.e. *entanglement*) between the two spins.

The choice of spins as the entangled entities is arbitrary, of course. The same entanglement can be found in any pair two-state quantum systems (qubits), for example photons, which can be vertically $|V\rangle$ or horizontally $|H\rangle$ polarized.

The above argument neglects to mention an initially mixed state that could mimic state (1.2) in certain cases,

$$\rho_{\text{mixed}} = \begin{cases} |\uparrow_1\uparrow_2\rangle & 50\% \\ |\downarrow_1\downarrow_2\rangle & 50\% \end{cases}. \quad (1.5)$$

However, this state ρ_{mixed} will not always behave in the same way as the entangled state $|1, 2\rangle$, as can be seen by looking at the expectation value $\langle\sigma^x \otimes \sigma^x\rangle$ for example. The entangled state in (1.2) will result in an expectation value of 1, while the mixed state in (1.5) will give 0. The distinction between these two states can be understood by considering the formal definition of entanglement.

Mathematical definition of Entanglement

A system divided into two regions, A and B , is in an entangled state if its density matrix ρ cannot be written in the form,

$$\rho = \sum_i p_i(\rho_{i_A} \otimes \rho_{i_B}), \quad (1.6)$$

where the p_i 's represent the probabilities of states $\rho_{i_A} \otimes \rho_{i_B}$, and the ρ_{i_A} 's (ρ_{i_B} 's) are density matrices representing the state in region A (B). The work in this thesis is limited to the measurement of entanglement within pure states, which considerably simplifies the

definition of entanglement. A pure state $|\Psi\rangle$ is entangled between regions A and B if it cannot be written in the form,

$$|\Psi\rangle = |\psi_A\rangle \otimes |\psi_B\rangle, \quad (1.7)$$

where $|\psi_A\rangle$ is a wavefunction representing the state in region A and $|\psi_B\rangle$ is a wavefunction representing the state in region B .

Quantification of Entanglement

The quantification of entanglement is not a completely straightforward procedure. First, because it involves the spatial division of a system into two regions A and B . Second, there are many different measures of entanglement that will give different values for the same system. These quantities will normally agree in which systems are more or less entangled, i.e. the “relative” entanglement. However they will not agree on the “absolute” entanglement, except in the cases where the regions are maximally entangled or completely unentangled systems.

The most commonly used measure of entanglement is called the von Neumann entanglement entropy (EE),

$$S_{\text{vN}} = -\text{Tr}(\rho_A \ln \rho_A), \quad (1.8)$$

where $\rho_A = \text{Tr}_B(\rho)$ is the reduced density matrix traced out over region B . The von Neumann EE has many special properties (such as subadditivity [50]) that are not necessarily shared by its generalization into the larger family of Renyi entanglement entropies, defined as,

$$S_\alpha = \frac{1}{1-\alpha} \ln[\text{Tr}(\rho_A^\alpha)]. \quad (1.9)$$

Taking the limit of $\alpha \rightarrow 1$, invoking l’Hôpital’s rule by taking the derivative of the numerator and denominator separately, one recovers the von Neumann EE. The Renyi EEs have the property

$$S_n \geq S_m \quad \text{for } m > n, \quad (1.10)$$

meaning that lower index Renyi EEs will have larger (or equal) values for the same system (see Figure 1.1).

The two cases in which all Renyi EEs agree is for minimal and maximal entanglement. When the two regions are unentangled, tracing out region B will leave us with a pure state, since regions A and B will both begin as independent pure states $|A\rangle \otimes |B\rangle$. Then ρ_A will have eigenvalues $\{1, 0, \dots, 0\}$, leading to $\text{Tr}\rho_A^\alpha = 1$ no matter which value of α is used. Taking $\ln(1)$ gives zero for all of the Renyi EEs.

The maximally entangled state, on the other hand, gives a reduced density matrix with eigenvalues $\{\frac{1}{n}, \frac{1}{n}, \dots, \frac{1}{n}\}$ where n is the lesser of the dimensions of the Hilbert space of region A and region B . From there we have

$$\begin{aligned}
S_\alpha^{\max} &= \frac{1}{1-\alpha} \ln \left[\sum_{i=1}^n \left(\frac{1}{n}\right)^\alpha \right] \\
&= \frac{1}{1-\alpha} \ln \left[n \left(\frac{1}{n}\right)^\alpha \right] \\
&= \frac{1}{1-\alpha} \ln \left[\frac{1}{n^{\alpha-1}} \right] \\
&= \frac{1}{1-\alpha} (\ln[1] - \ln[n^{\alpha-1}]) \\
&= \frac{-1}{1-\alpha} \ln[n^{\alpha-1}] \\
&= \frac{-(\alpha-1)}{1-\alpha} \ln[n] \\
&= \ln[n],
\end{aligned} \tag{1.11}$$

which is again independent of the Renyi index α . This can be seen in Figure 1.1 where all values of α give the same $\ln 2$ for the maximally entangled state between two spins. The dimension of the Hilbert space of a spin- $\frac{1}{2}$ spin is 2, and so the result of $\ln 2$ is consistent with equation (1.11).

The Renyi entanglement entropies (and entanglement in general) are symmetric between regions A and B . That is,

$$S_\alpha^A = S_\alpha^B, \tag{1.12}$$

which really implies that $\text{Tr}(\rho_A^\alpha) = \text{Tr}(\rho_B^\alpha)$. The eigenvalues of the reduced density matrix are the same whether region B or region A is traced out. This should not be unexpected, as entanglement is a property between the two systems, not a property of either system on its own. This symmetry is only present when the initial system (the union of regions A and B) is in a pure quantum state, where the eigenvalues of the full density matrix ρ are $\{1, 0, \dots, 0\}$, otherwise the EEs will capture the thermodynamic entropy of the state along with the entanglement. In fact, the Renyi EEs cannot be used to measure entanglement of an initially mixed state, and one must look to other measures such as the mutual information, to study systems in mixed states [50].

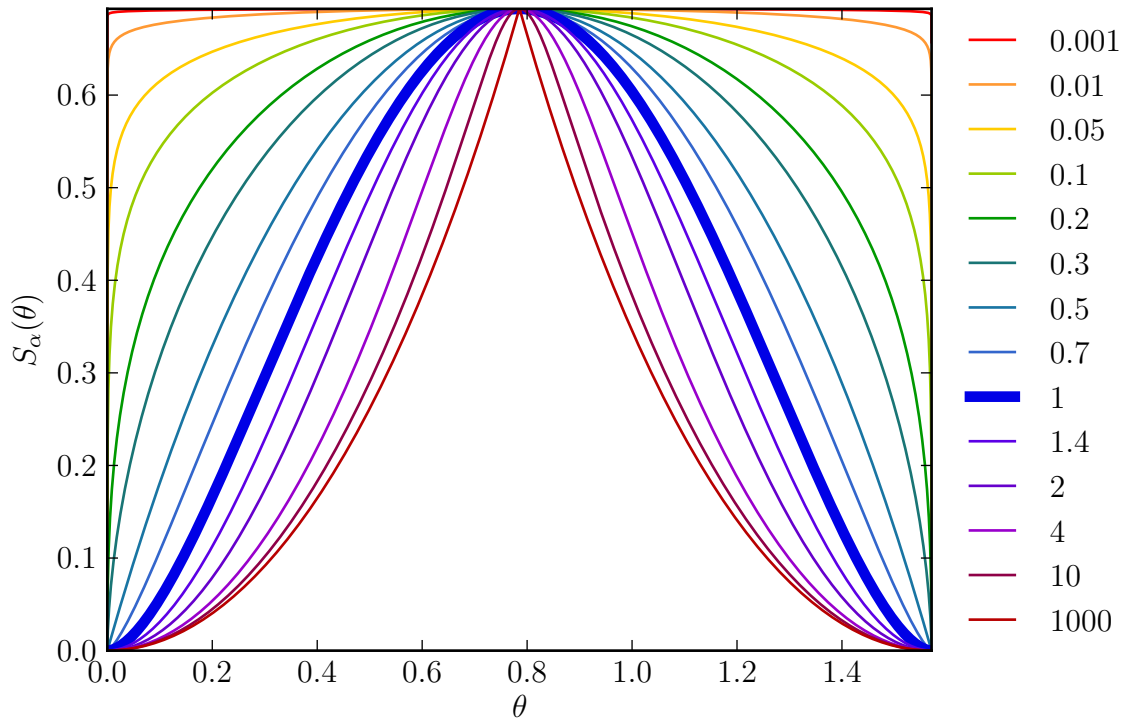


Figure 1.1: The Renyi entanglement entropies S_α between two spins in the state $|\psi\rangle = \cos\theta|\downarrow\downarrow\rangle + \sin\theta|\uparrow\uparrow\rangle$, where θ is an arbitrary parameter that tunes the entanglement between the two spins. The legend to the right specifies the different values of α used. The von Neumann entanglement entropy is represented by the thick blue line.

Intuition for entanglement

The concept of entanglement entropies can seem somewhat abstract at first. The Renyi EEs are a quantification of the uncertainty of the state after tracing out region B . If the two regions are unentangled then tracing out region B has no effect on the state in region A . On the other hand, if the regions *are* entangled then the result of the partial trace is a density matrix for region A which gives a list of classical probabilities of the different possible states. This is analogous to the thermodynamic entropy $S = k_B \sum_i p_i \ln p_i$ where p_i is the probability of the system being in microstate i , the difference being that the state considered for entanglement is not the *whole* system, but rather one region of the system with the rest traced out. The more entangled the initial state was, the more uncertain we are in the resulting state after one region is traced out.

In the case of the state in (1.2), when spin 2 is traced out we have the maximal possible uncertainty in the resulting state, equivalent to $\theta = \pi/4$ in Figure 1.1. The entanglement is limited by the maximal amount of uncertainty one could have in a state. In principle this seems unlimited, but with these systems of spins we know what type of spins we are working with and how many we have. For example, in a region A containing three spin-2 particles, each with five possible states, the maximal entanglement with some larger number of spins in region B is $3 \ln 5$, or three times the logarithm of the dimension of the Hilbert space for one of the spins (or the logarithm of the total dimension of the Hilbert space for region A).

Entanglement Monogamy: *Why everything can't be maximally entangled with everything else*

An interesting concept relating specifically to entanglement is *monogamy* [13]. One spin, site, or qubit only has so much entanglement to give, and once that is shared with another spin or group of spins, the original spin cannot share any more entanglement with any other object. This is related to the maximal possible amount of uncertainty in a spin state, mentioned above, and has implications for the groundstate of the Heisenberg antiferromagnet, discussed in Section 1.2.2. The maximum amount of entanglement, as shown in Equation (1.11), is equal to the logarithm of the dimensions of the smaller of the two Hilbert spaces for region A and B .

1.2 Lattice Models in Condensed Matter

The work in this thesis pertains to condensed matter lattice models—interactions between “sites” arranged in a repeating pattern. The lattices discussed will mainly be two dimensional square lattices of interacting quantum spins. See Figure 1.3 for an example of a square lattice. The interaction of these spins is governed by a Hamiltonian. Interactions considered in this thesis will be between neighbouring sites, though longer range interactions may also be studied with many of the numerical techniques discussed.

1.2.1 Quantum Critical Points

A quantum critical point is a point in a phase diagram at *zero temperature*, where there is a continuous phase transition. Because the transition occurs at zero temperature it cannot be driven by thermodynamic fluctuations and is instead driven by quantum fluctuations.

Continuous phase transitions show a divergent correlation length and exhibit scale-invariance. Unlike a first order transition with “coexistence”, i.e. the water–ice transition where some regions are in phase X and the other regions are in phase Y, at a critical point the system is in a state where the two phases are no longer distinct from each other.

Quantum critical points can be found in lattice models governed by quantum mechanical Hamiltonians with multiple parameters, including some of those mentioned below. The zero temperature groundstate of the system will be driven through a phase transition at special critical values of the Hamiltonian parameters.

1.2.2 The antiferromagnetic spin- $\frac{1}{2}$ Heisenberg model

The Heisenberg model is a quantum mechanical generalization of the classical Ising model. (The Ising model itself is not explicitly covered here, but readers may glance down to the transverse-field Ising model section (1.2.4) for a reminder.)

The Hamiltonian for the antiferromagnetic Heisenberg model is

$$\mathcal{H}_{\text{Heis}} = J \sum_{\langle ij \rangle} \mathbf{S}_i \cdot \mathbf{S}_j, \quad (1.13)$$

where J is a positive constant (negative for the ferromagnetic case), and $\mathbf{S}_i = (S_i^x, S_i^y, S_i^z)$ is the spin- $\frac{1}{2}$ operator on site i (see Equation (1.1)). The spin interaction can be rewritten

and understood in many different ways,

$$\mathbf{S}_i \cdot \mathbf{S}_j = S_i^x S_j^x + S_i^y S_j^y + S_i^z S_j^z \quad (1.14)$$

$$= \frac{1}{2} (S_i^+ S_j^- + S_i^- S_j^+) + S_i^z S_j^z \quad (1.15)$$

$$= \frac{1}{2} \left((S_i + S_j)^2 - S_i^2 - S_j^2 \right). \quad (1.16)$$

The groundstate of the ferromagnetic (FM) case of the Heisenberg model shows a spontaneous symmetry breaking, similar to the Ising model, as all spins will align ferromagnetically. The distinction is that the spins need not point in the $\pm z$ direction, but can be aligned in any direction.

The antiferromagnetic case (AFM) bears a less striking resemblance to that of the Ising model, where neighbouring spins are exactly anti-aligned so that z component of the spins the lattice will form an up, down, up, down $|\uparrow\downarrow\uparrow\downarrow\rangle$ pattern (and the x and y components will be zero). For the AFM Heisenberg model, this state minimizes the third term of (1.14), but not necessarily the other two terms.

Let us begin by examining the energies of a two spin system (setting $J = 1$). One would expect that since the model has a low energy when the dot product of spins is minimized, the highest energy state would be when the spins are completely aligned, maximizing $\mathbf{S}_1 \cdot \mathbf{S}_2$. We will start with a pair of sites aligned in the FM state $|\uparrow\uparrow\rangle$,

$$\begin{aligned} E_{|\uparrow\uparrow\rangle} &= \langle\uparrow\uparrow|\mathbf{S}_1 \cdot \mathbf{S}_2|\uparrow\uparrow\rangle = \langle\uparrow\uparrow|\frac{1}{2} [S_1^+ S_2^- + S_1^- S_2^+] + S_1^z S_2^z|\uparrow\uparrow\rangle \\ &= \frac{1}{2}(0 + 0) + (\frac{1}{2})(\frac{1}{2}) \\ &= \frac{1}{4}. \end{aligned} \quad (1.17)$$

The energy for these two aligned spins is $\frac{1}{4}$. We can extend this to a large lattice of aligned spins and say that the energy for the ferromagnetic state is $E_{FM} = N_b/4$, where N_b is the number of nearest-neighbour lattice bonds.

Analogously, we can take a pair of anti-aligned spins and calculate their energy:

$$\begin{aligned} E_{|\uparrow\downarrow\rangle} &= \langle\uparrow\downarrow|\mathbf{S}_1 \cdot \mathbf{S}_2|\uparrow\downarrow\rangle = \langle\uparrow\downarrow|\frac{1}{2} [S_1^+ S_2^- + S_1^- S_2^+] + S_1^z S_2^z|\uparrow\downarrow\rangle \\ &= \frac{1}{2}(0 + 0) + (\frac{1}{2})(-\frac{1}{2}) \\ &= -\frac{1}{4}. \end{aligned} \quad (1.18)$$

If this state were extended to a full lattice (which is not possible on all types of lattices, only bipartite lattices) we would find that $E_{AFM} = -E_{FM} = -N_b/4$. A bipartite lattice is a lattice that can be divided into two sublattices. For the case of the square lattice,

State	$ \uparrow\uparrow\rangle, \downarrow\downarrow\rangle$	$\frac{1}{\sqrt{2}}(\uparrow\downarrow\rangle + \downarrow\uparrow\rangle)$	$ \uparrow\downarrow\rangle, \downarrow\uparrow\rangle$	$\frac{1}{\sqrt{2}}(\uparrow\downarrow\rangle - \downarrow\uparrow\rangle)$
Energy	1/4	1/4	-1/4	-3/4
Lattice Energy	$N_b/4$	$E < N_b/4$	$-N_b/4$	$-N_b/4 \geq E > -3N_b/4$
$\langle (S_1 + S_2)^2 \rangle$	2	2	1	0
Eigenstate	Yes	Yes	No	Yes

Table 1.1: A summary of properties for some 2-site states in the AFM Heisenberg model. The first row shows the energies (in units of J) of the 2-spin state. The second row gives the energy one would obtain if this state was extended to a bipartite lattice of sites with N_b bonds. The third row shows the expectation value of the total spin operator for the two spins combined. The final row indicates which of the spin states are eigenvalues of the 2-site Heisenberg Hamiltonian.

divided into sublattices X and Y , all sublattice X sites are surrounded by sublattice Y sites, and vice versa.

Now, if you are familiar with the Heisenberg antiferromagnet then you will know that the state of anti-aligned pairs of nearest-neighbour sites is not the lowest energy state of the system. For a pair of spins the lowest energy state is the singlet (also called a valence bond) state: $|\psi\rangle = \frac{1}{\sqrt{2}}(|\uparrow\downarrow\rangle - |\downarrow\uparrow\rangle)$. Its energy is,

$$\begin{aligned}
E_{\text{VB}} &= \langle \psi | \mathbf{S}_1 \cdot \mathbf{S}_2 | \psi \rangle = \langle \psi | \frac{1}{2} [S_1^+ S_2^- + S_1^- S_2^+] + S_1^z S_2^z | \psi \rangle \\
&= \frac{1}{2}(-1) - \frac{1}{4} \\
&= -\frac{3}{4}.
\end{aligned} \tag{1.19}$$

The results of these energy calculations are summarized in Table 1.1.

Unlike the previously discussed spin states in Equations (1.17) and (1.18) it is not possible to directly extend this singlet state to a larger lattice while still minimizing the energy of every pair of spins. According to the rule of entanglement monogamy (see Section 1.1) a spin can only share up to $\ln 2$ entanglement with the outside environment. Since the two spins in the singlet $|\psi\rangle$ are maximally entangled, neither can be entangled with any other spin. A spin can only be in one valence bond at a time, so though one could tile these states on a lattice, there would be many neighbouring sites that were not in an energetically minimized state.

From these two-site calculations it can be inferred that the energy for the groundstate of the AFM Heisenberg model on a lattice must be greater than $-3N_b/4$ and less than or equal to $-N_b/4$. The actual value is around $-0.335N_b$ on a 2D square lattice [59].

The Valence Bond picture

The AFM Heisenberg groundstate on a bipartite lattice can be described in the valence bond picture, instead of the S^z spin picture. In this language, states are represented by sums of many valence bonds on a lattice, where each site is part of exactly one valence bond. Each valence bond must originate on a sublattice X site, and terminate on a sublattice Y site.

The AFM Heisenberg groundstate, which I will now refer to as the “Néel” state (not to be confused with the AFM spin state in which neighbouring spins are precisely antiparallel), can be exactly represented as a sum of VB states with coefficients weighted toward states which on average contain the shortest-ranged bonds, but still including every possible bipartite VB state [59].

Criticality of the Néel state

Though the Néel state has a diverging correlation length it is not a quantum critical system. This is in part because no parameter is being varied to take us to a critical value for the system, so it does not meet the criterion of being at a transition between phases.

Additionally the state shows a type of order, which would tend to clash with any sort of scale-invariance, though the system may exhibit scale-invariance in the entanglement properties and correlations. The order is observed through the staggered magnetization,

$$m_s^2 = \left(\frac{1}{N} \sum_{i=1}^N (-1)^{x_i} \mathbf{S}_i \right)^2, \quad (1.20)$$

where x_i is 0 for spins on sublattice X and 1 for sites on sublattice Y . The expectation value of this quantity is non-zero when sites on different sublattices are likely to have anti-correlated spins, while those on the same sublattice are somewhat correlated. This correlation is not perfect, but rather a reduced value of $\sqrt{\langle m_s^2 \rangle} = 0.3074$ is obtained [60] instead of the maximal value of 0.5.

1.2.3 The Heisenberg Bilayer

The Heisenberg bilayer model is a system of two 2D Heisenberg model planes with another Heisenberg interaction between them [83, 39]. The interplane (J_\perp) and intraplane (J)

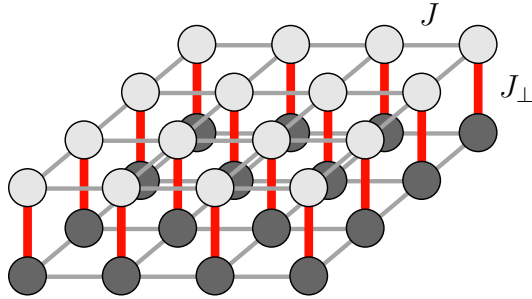


Figure 1.2: A 4×4 bilayer lattice. The thick red bonds indicate the interlayer coupling J_{\perp} and the thin grey bonds show the intralayer coupling J .

couplings can be varied independently. The Hamiltonian of this system is,

$$\mathcal{H}_{\text{Bi}} = J \sum_{\langle ij \rangle} (\mathbf{S}_{1i} \cdot \mathbf{S}_{1j} + \mathbf{S}_{2i} \cdot \mathbf{S}_{2j}) + J_{\perp} \sum_i \mathbf{S}_{1i} \cdot \mathbf{S}_{2i}, \quad (1.21)$$

where $\langle ij \rangle$ only indicates nearest-neighbour pairs of spins *within* planes. The labels 1 or 2 indicate in which layer a spin is found. The interactions between planes are confined to the final term of the Hamiltonian.

This work is limited to the study of the antiferromagnetic side of this Hamiltonian, where both J and J_{\perp} are positive. Both terms will favour spin singlets (VB states) between neighbouring sites in the groundstate, where a large J_{\perp} term will favour singlets between layers while a large J term would tend to create two independent 2D Néel groundstates.

Due to these two competing Hamiltonian terms, which will favour the formation of VBs either in-plane or perpendicular to the plane, *and* the property of entanglement monogamy, which will not allow both of these terms to be energetically satisfied, the system has a quantum phase transition between these two phases. The quantum critical point has been studied with both series expansion [84, 22] and quantum Monte Carlo, and found by the QMC to be at $(J_{\perp}/J)_c = 2.5220(2)$ [83]. In Section 3.9.2 we examine with the entanglement scaling at this quantum critical point.

1.2.4 The Transverse-Field Ising Model

The transverse-field Ising model (TFIM) begins with one of the simplest classical spin Hamiltonians, the Ising model,

$$\mathcal{H}_{\text{Ising}} = -J \sum_{\langle ij \rangle} \sigma_i^z \sigma_j^z, \quad (1.22)$$

where spins take values of ± 1 . The Ising model is considered classical because all of its eigenstates can be represented using classical bits rather than qubits. Adding a transverse field in the σ^x direction gives us the TFIM,

$$\mathcal{H}_{\text{TFIM}} = -J \sum_{\langle ij \rangle} \sigma_i^z \sigma_j^z - h \sum_i \sigma_i^x \quad (1.23)$$

$$= -4J \sum_{\langle ij \rangle} S_i^z S_j^z - 2h \sum_i S_i^x. \quad (1.24)$$

This field adds off-diagonal elements to the Hamiltonian so that the system can no longer be expressed classically. The transverse-field Ising model differs from the previously mentioned Heisenberg Hamiltonians in that it uses Pauli matrices instead of spin- $\frac{1}{2}$ operators. However, it is possible to translate between the two languages (see Equation (1.1)).

The classical Ising model Hamiltonian can be represented as a diagonal matrix, where every possible spin state is an eigenstate with a definite energy. For N spins, any of the eigenstates can be represented by an integer from 0 to $2^N - 1$, which is equivalent to N different \mathbb{Z}_2 objects (each is 0 or 1), so we have $\mathbb{Z}_2^{\otimes N}$. Adding in the transverse field gives off-diagonal terms in the Hamiltonian, and the eigenstates are no longer as simply represented in the S^z or σ^z basis. The spins are now $SU(2)$ objects, so we have $SU(2)^{\otimes N}$. These spins can be represented as superpositions of any of the possible 2^N states, and a vector representing an eigenstate has 2^N elements, meaning that 2^N $U(1)$ numbers are required to specify the state. This statement says that we can represent a $SU(2)^{\otimes N}$ state using $U(1)^{\otimes 2^N}$. Comparing $\mathbb{Z}_2^{\otimes N}$ to $U(1)^{\otimes 2^N}$ is basically the difference in complexity between representing classical and quantum (spin- $\frac{1}{2}$) bits.

Taking both J and h as positive, when $J > h$ the Hamiltonian favours a phase where all spins are aligned in a ferromagnetic phase, but the two ferromagnetic states: all spins up $|\uparrow\rangle^{\otimes N}$ and all spins down $|\downarrow\rangle^{\otimes N}$, are degenerate in energy. When $h > J$, the transverse field term becomes more important and the spins will align in the $+x$ direction, $|+\rangle = \frac{1}{\sqrt{2}}(|\uparrow\rangle + |\downarrow\rangle)$. As in the Heisenberg bilayer, the TFIM has two competing interactions. A state minimizing the first term cannot simultaneously minimize the second, and this leads to a quantum phase transition at the critical value $(h/J)_c = 3.044$ in 2D systems [54], and $(h/J)_c = 1$ in 1D systems.

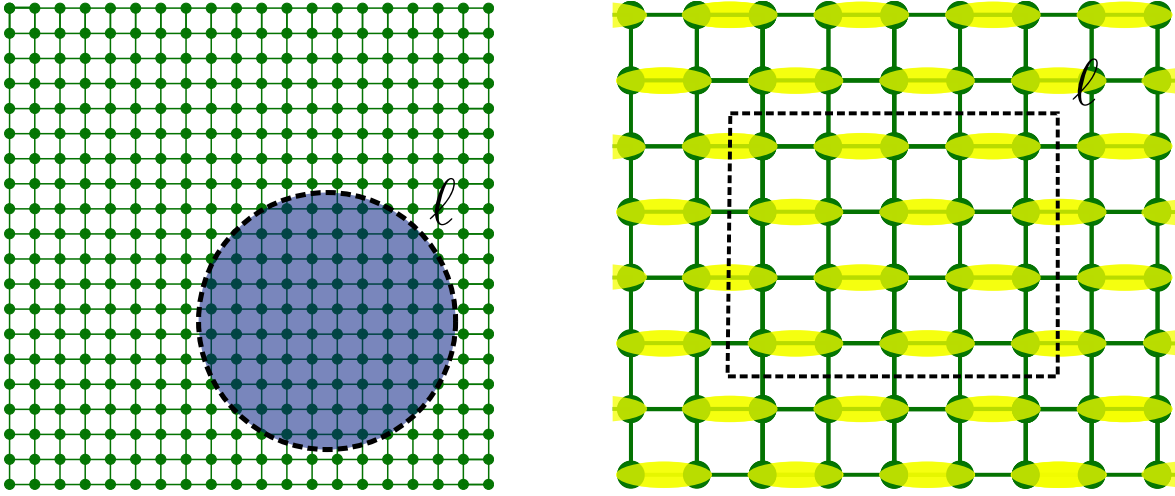


Figure 1.3: **(Left)** A square lattice separated into two regions by a round boundary of length ℓ . **(Right)** A square lattice in a valence bond solid state divided into two regions by a rectangular boundary of length ℓ . The yellow ovals represent a valence bond state $(|\uparrow\downarrow\rangle - |\downarrow\uparrow\rangle)/\sqrt{2}$.

1.3 Entanglement Scaling in Condensed Matter Systems

Entanglement scaling refers to how entanglement acts as we vary the two regions, A and B (see Figure 1.3). Sometimes entanglement scales as the size of the regions, and other times as a function of the size of the boundary ℓ between the regions. This can be studied by looking at finite system sizes and increasing the boundary length in some systematic way, or by choosing a fixed system and boundary geometry and then systematically increasing the size of the system and boundary proportionally.

Because of the gapless nature of the systems studied in this thesis, the second technique will make it much easier to study the quantities we are interested in. The reasons for this will be discussed below and in Section 2.5.1.

Beyond two sites, not much is known about the entanglement of larger systems with *interacting* Hamiltonians. There are some special cases where the scaling of entanglement is exactly known [6, 89, 18], but in most systems we are left to speculate or make predictions using approximate methods.

Gapped vs Gapless Systems

A gapped system has a gap between the energy of the groundstate and the next excited state, even in the thermodynamic limit. Gapless systems, on the other hand have an infinitesimal difference in energy between the groundstate and the first excited state, so instead of a finite energy gap there is a continuum of low energy states.

The entanglement scaling in the groundstates of gapped versus gapless systems is fundamentally different. Generally gapped systems will follow much simpler entanglement scaling relations, while gapless systems have extra unknown terms, making it difficult to extract specific subleading terms of interest. The systems studied in this thesis are exclusively gapless.

1.3.1 One Dimension

At special gapless one dimensional quantum critical points with conformal invariance (i.e. the system is invariant under transformations which preserve the lattice angles), the entanglement scales with the known function from conformal field theory (CFT) [28, 82, 41, 5],

$$S_\alpha = \frac{c}{6} \left(1 + \frac{1}{\alpha} \right) \ln \left[\frac{L}{\pi} \sin \left(\frac{\pi x}{L} \right) \right], \quad (1.25)$$

where L is the total length of the 1D open boundary chain, and x is the length of region A , where region B would have length $L - x$. The quantity $x' = (L/\pi) \sin(\pi x/L)$ is called the “chord length”. The coefficient c is known as the *central charge* [7], a universal number that can be used to characterize and classify different quantum critical points. Its numerical or analytical determination provides an invaluable tool in identifying which, if any, CFT describes the scaling limit of a given critical Hamiltonian in 1D.

Away from these conformal critical points, gapped systems are known to scale with the *area law*, meaning that the entanglement scales proportionally to the size of the boundary between regions A and B . In 1D, the result is that the entanglement has a constant value for any x (except, usually, when x or $L - x$ is very small).

1.3.2 Two Dimensions

In higher dimensions, the scaling behaviour of the entanglement entropy is much less well-understood. Groundstates of local Hamiltonians are generally believed to produce *area*

law scaling as in 1D, though in 2D the boundary is a 1D object and thus the area law [15] (the name of which originated in three dimensional systems) becomes a boundary law, with subleading terms.

$$S_\alpha = a\ell + \dots \tag{1.26}$$

The subleading corrections to the area law may harbour universal quantities that can be used to identify and characterize quantum phases and phase transitions. A well established example is the topological entanglement entropy [16, 23, 40, 44, 53] of a gapped state with topological order. In gapless states, the subleading corrections may still potentially harbour universal quantities, but they can become obscured by other non-universal subleading contributions.

In the 2D Heisenberg model and the 2D nearest-neighbour resonating valence bond state, a shape dependent term analogous to the 1D CFT scaling (Equation (1.25)) was found [35]. This term depends on the ratio of x/L for a cylindrical region A on a torus, and leads to a deviation from the area law when looking at region A s with different widths for a given $L \times L$ system. This aspect-ratio dependence for the 2D Heisenberg model is discussed in Section 2.5.1.

Additionally, discussed in Section 2.5.1, a logarithmic correction to the area law was found for the Heisenberg model in 2D, and is posited to be due to the gapless Goldstone modes of that model [25, 37, 49].

Another subleading contribution to the entanglement entropy is a logarithm due to the presence of a corner in the boundary between regions A and B [10, 17, 48]. In some cases this contribution is combined with the Goldstone mode logarithm and thus both terms must be studied concurrently. The numerical linked-cluster expansion technique, however, provides a method to exactly cancel off any terms not due to the presence of a corner in the boundary, facilitating the study of this term. The coefficient of this corner term is expected to be universal [10]. This is because the term scales as the logarithm of a ratio of the length scale and a short-scale cutoff (in field theories this cutoff corresponds to limiting the wavelength to be above a certain magnitude, while in condensed matter lattice systems this cutoff is equivalent to the lattice spacing, which we set to unity). Because this ratio is contained inside of a logarithm it is possible to separate out the two different terms,

$$c \ln(\ell/\Lambda) = c \ln(\ell) - c \ln(\Lambda), \tag{1.27}$$

and the non-universal, lattice-dependant cutoff is relegated to another term, while the piece that scales with the length enjoys a universal coefficient which should in principle distinguish between models in different universality classes. It is one of the goals of this thesis to test this prediction.

This corner term is discussed in the context of the 2D Heisenberg model in Section 2.5.1, for in 2D transverse-field Ising model at its quantum critical point in Section 3.9.1, and for the Heisenberg model bilayer at its quantum critical point in Section 3.9.2.

Entanglement Scaling Intuition

There are intuitive arguments that one can make as to why entanglement might scale in a certain way. The pervasive area law has one such argument for gapped systems and one for gapless systems. The area law (boundary law in 2D) states that for systems with only local interactions, entanglement between two regions will scale proportional to the length of the boundary ℓ between those regions. In a gapped state such as the valence bond solid state pictured in Figure 1.3, the entanglement across the boundary from each valence bond that is cut by the boundary gives a contribution of $\ln 2$. Thus we can simply add up the number of valence bonds cut, which is proportional to the length of the boundary (at least in the y -direction of the case shown).

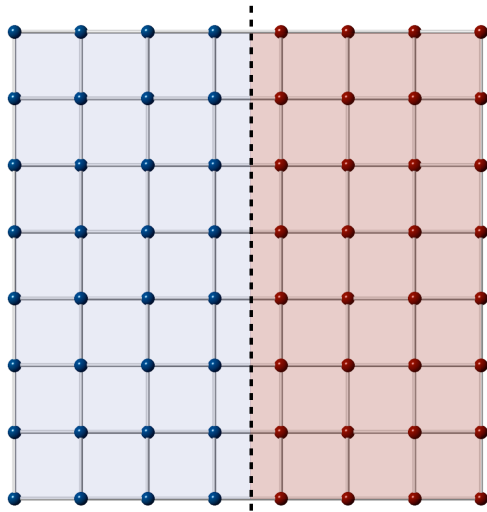
The two following examples apply to scale invariant gapless systems, such as those at a critical point. These simple pictures of area law scaling and corner entanglement assume that entanglement in a system gives an order one contribution per site, and the same contribution for each “renormalized” site, where the renormalization takes every block of $n \times n$ sites and those together effectively behave as one site. In this example $n = 2$, so a 2×2 block of sites becomes the new renormalized site [24].

Intuition for the Area Law at a quantum critical point

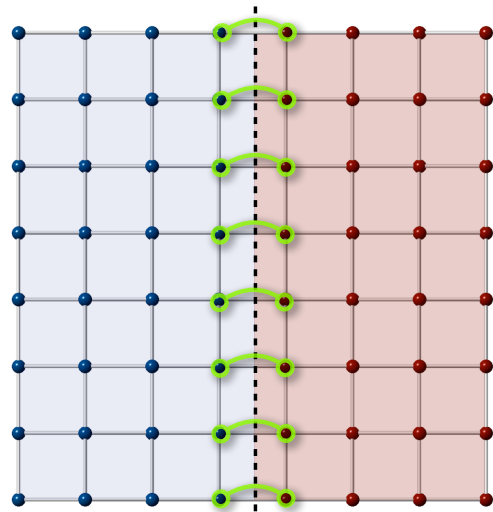
Figure 1.4 shows entanglement contributions from successive renormalizations applied to a system with a straight boundary. The sum of contributions from each length scale is

$$\begin{aligned}
 S &\sim \ell + \frac{\ell}{n} + \frac{\ell}{n^2} + \dots = \ell \left(1 + \sum_{x=1}^{\infty} \left(\frac{1}{n} \right)^x \right) \\
 &= \ell \left(1 + \frac{1}{n-1} \right) \text{ for } |n| > 1 \\
 &= \frac{n}{n-1} \ell
 \end{aligned} \tag{1.28}$$

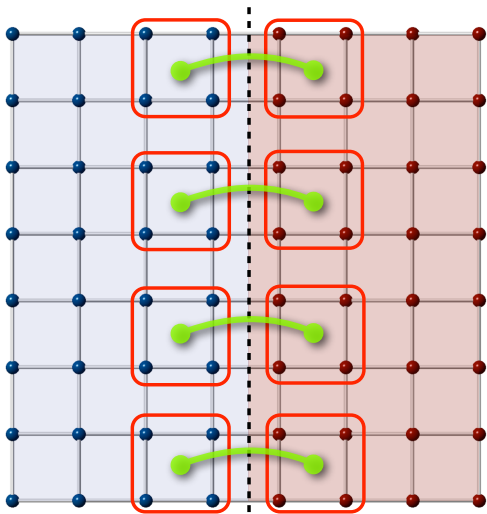
and of course n would always be greater than 1 for the renormalization to make sense. In the end we obtain a term proportional to the length of the boundary, i.e. the area law.



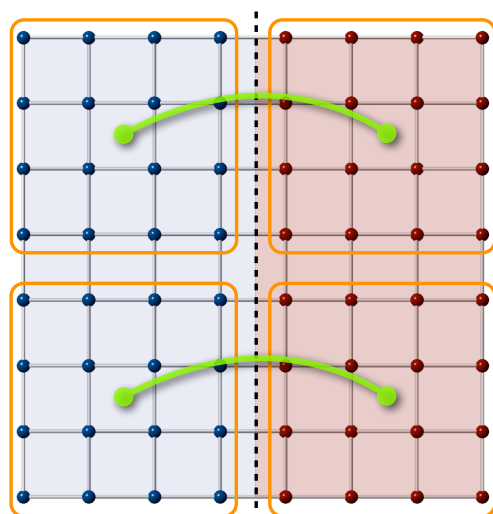
(a) A square lattice divided into two regions, A and B .



(b) Each pair of sites adjacent to the boundary gives one unit of entanglement, for a total of ℓ units.



(c) After one renormalization each new pair of sites gives one unit of entanglement, but now there are only $\ell/2$.



(d) After the second renormalization there are $\ell/4 = \ell/n^2$ units of entanglement.

Figure 1.4: A picture to give some intuition for the area law in a scale invariant system. The sum of contributions from each length scale is $S \sim \ell + \frac{\ell}{n} + \frac{\ell}{n^2} + \dots$

We can also look at what would happen if the series does not extend forever,

$$\begin{aligned}
S &\sim \ell \left(1 + \sum_{x=1}^{\log_n \ell} \left(\frac{1}{n} \right)^x \right) = \ell \left(1 + \frac{1 - \left(\frac{1}{n} \right)^{\log_n \ell}}{n - 1} \right) \\
&= \ell \left(1 + \frac{1 - \left(\frac{1}{\ell} \right)}{n - 1} \right) \\
&= \frac{n}{n - 1} \ell - \frac{1}{n - 1}.
\end{aligned} \tag{1.29}$$

The series is limited by the number of times the renormalization can be performed, $\log_n \ell$, i.e. the number of times the length ℓ can be divided by n until the result is 1. The same area law piece is recovered, but this time there is subleading constant term.

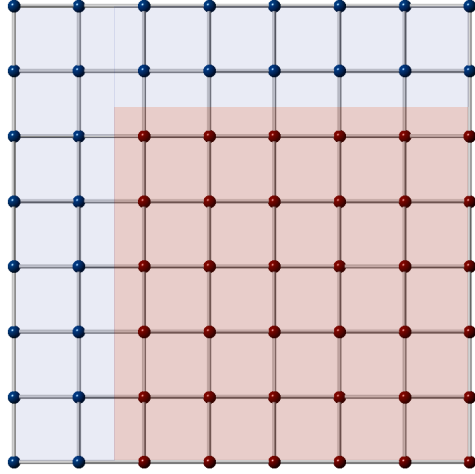
Intuition for the Corner Logarithm

Figure 1.5 shows the analogous example for the contribution due to the presence of a corner in the boundary (ignoring any contributions from the linear regions of the boundary). We assume that on each length scale there will be an order one contribution due to the presence of a corner. Then the number of times that the finite sized system can be rescaled is again equal to $\log_n \ell$. Therefore, for finite systems, we expect a corner to give a logarithmic contribution to the scaling of the entanglement entropy, proportional to $\ln \ell$

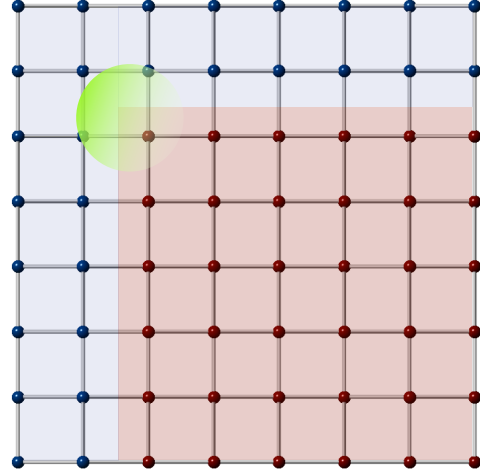
The coefficient of this logarithmic term will tell us about the decay of entanglement in the system. It will give insight into by what factor the system should be renormalized to get the same level of contribution to the entanglement.

1.4 Tensor Diagram Notation

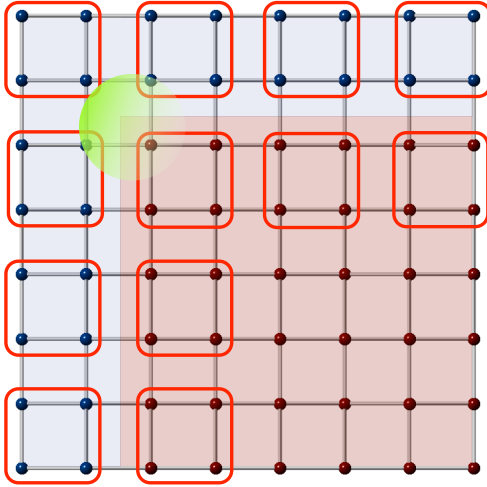
Tensor diagram notation (TDN) (or Penrose graphical notation, as it is also known) is a graphical language to describe operations between vectors, matrices, and higher dimensional tensors [12, 52, 87]. Its greatest asset is that it makes sometimes complicated identities easy to understand, since equivalence in this diagrammatic language is determined by whether two diagrams are topologically the same or not. Though this language can be used to describe higher dimensional objects, in this thesis we need only deal with matrix and vector operations.



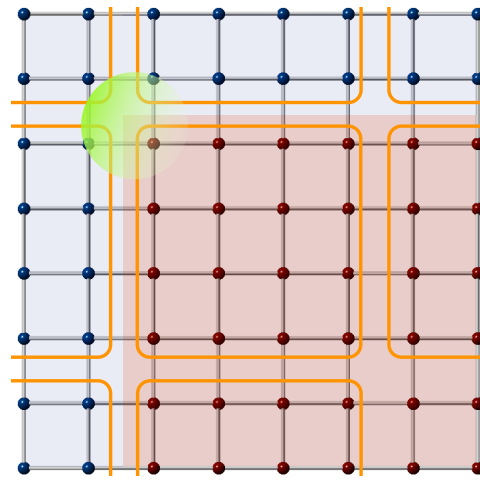
(a) A square lattice divided into regions A and B by a boundary with a corner.



(b) The corner gives one unit of contribution for each length scale.



(c) After one renormalization we get one more contribution.



(d) Another unit of entanglement from the second renormalization.

Figure 1.5: Each renormalization gives one contribution to the entanglement due to a corner. The number of times one can renormalize is equal to $\log_n \ell$ where ℓ is the length of the boundary in either the x or y direction in this picture.


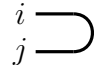
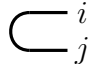
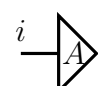

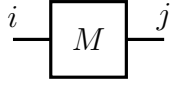
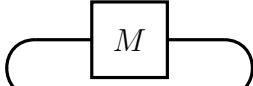
Tensor Diagram	Abstract Index	Bra/Ket	Matrix/Vector
	δ_j^i	$\sum_i e_i\rangle\langle e_i $	$\mathbf{1}$
	g^{ij}	$\sum_i e_i\rangle \otimes e_i\rangle$	n/a
	g_{ij}	$\sum_i \langle e_i \otimes \langle e_i $	n/a
	A^i	$ A\rangle$	$A = \begin{bmatrix} A_1 \\ \vdots \\ A_n \end{bmatrix}$
	A_i	$\langle A $	$A^\dagger = [A_1^* \ \cdots \ A_n^*]$
	M_j^i	\hat{M}	$M = \begin{bmatrix} M_{11} & \cdots & M_{1n} \\ \vdots & \ddots & \vdots \\ M_{n1} & \cdots & M_{nn} \end{bmatrix}$
	$\delta_i^j M_j^i = M_i^i$	$\sum_i \langle e_i \hat{M} e_i \rangle$	$\text{Tr}(M)$

Table 1.2: A table translating between four different types of mathematical notation: tensor diagram notation, abstract index notation, bra/ket notation, and the standard matrix/vector notation of linear algebra.

In an attempt to help readers from different backgrounds to understand TDN, in this section I will relate three different notations: TDN, abstract index notation (which is fundamental to understanding TDN), and the standard bra/ket/matrix notation of quantum mechanics. Table 1.2 also summarizes the notational equivalencies in this section.

The simplest element of TDN is a “wire”,

$$\overset{i}{\text{---}} \overset{j}{\text{---}} = \delta_j^i = \sum_i \sum_j |e_i\rangle \langle e_i| e_j \rangle \langle e_j| = \sum_i |e_i\rangle \langle e_i| = \mathbf{1}. \quad (1.30)$$

The two indices, i and j , are like the rows and columns of the this object. The wire can be thought of as a Kroneker delta or an identity matrix. In general, an open wire to the left is in the space of column vectors, and an open wire to the right is in the space of row vectors, thus a wire is the diagonal outer product between basis vectors of a system. If there are no open wires (free indices) then the resulting product is just a scalar. Otherwise it is a vector (1 open wire), matrix (2 open wires), or a higher dimensional tensor (≥ 3 open wires).

A column vector is represented by a shape with an open wire on the left.

$$\overset{i}{\text{---}} \triangleleft \Psi \triangleright = \Psi^i = |\Psi\rangle \quad (1.31)$$

The shape need not be triangular or anything specific, but I have chosen them to resemble the bra/ket notation.

Similarly, a row vector is represented by a shape with an open wire on the right.

$$\triangleleft \Psi \text{---} \overset{j}{\text{---}} = \Psi_j = \langle \Psi| \quad (1.32)$$

We can connect these three objects to get an inner product,

$$\triangleleft \Psi \text{---} \text{---} \Psi \triangleright = \Psi_i \delta_j^i \Psi^j = \Psi_i \Psi^i = \langle \Psi | \Psi \rangle. \quad (1.33)$$

This diagram does not require indices because there are no free wires. Any indices are implicitly summed over by the Einstein summation convention. It should also be noted that by connecting wires in these diagrams it is assumed that their dimensions over that index are the same.

Placing two unconnected diagrams side by side is equivalent to a tensor multiplication of the two objects. The tensor product of (1.31) and (1.32) (an outer product in the case of two vectors) gives us,

$$i \text{---} \Psi \text{---} \Psi \text{---} j = \Psi^i \Psi_j = |\Psi\rangle \otimes \langle\Psi| = |\Psi\rangle\langle\Psi| = \rho, \quad (1.34)$$

where we recognize this as the density matrix of a system in state $|\Psi\rangle$. In terms of this graphical language, it is always possible to draw a box around any area of the diagram and call that “one object”. As long as the number of open wires stays the same, this relabelling is allowed. As a very simple example,

$$i \text{---} \Psi \text{---} \Psi \text{---} j = i \text{---} \rho \text{---} j, \quad (1.35)$$

we relabel this tensor product of wavefunctions as the matrix ρ .

As discussed in Section 1.1, to measure the entanglement we need to extract $\text{Tr}(\rho_A^\alpha)$, for a system divided into two spatial regions A and B . This quantity can be described using TDN. First we must separate the descriptions of regions A and B . Though the wavefunction is generally not separable in this way, it is possible to define a full basis for the possible states in region A , and the same for region B . The wavefunction can then be rewritten in terms of these *two* indices instead of just one,

$$\begin{matrix} a \\ \text{---} \\ \Psi \\ \text{---} \\ b \end{matrix} = \Psi^{ab} = \sum_i \sum_j c_{ij} |a_i\rangle |b_j\rangle. \quad (1.36)$$

Here the portions related to region A are coloured in red. This is a Schmidt decomposition of the wavefunction Ψ . The states $\{|a_i\rangle\}$ and $\{|b_j\rangle\}$ are sets of basis states for region A and B respectively, and c_{ij} is a scalar coefficient. Using the above expression for the wavefunction we can now take a partial trace over only the states in region B ,

$$\begin{matrix} i & & j \\ \text{---} & & \text{---} \\ \Psi & & \Psi \\ \text{---} & & \text{---} \\ \text{---} & & \text{---} \end{matrix} = \begin{matrix} i & & j \\ \text{---} & & \text{---} \\ \rho \\ \text{---} & & \text{---} \\ \text{---} & & \text{---} \end{matrix} = \Psi^{ik} \Psi_{jk} = \text{Tr}_B(\rho) = \rho_A. \quad (1.37)$$

The wire connecting the two region B indices acts as a trace, exactly as in equation (1.33).

To get ρ_A^2 we must multiply two copies of ρ_A together. Matrix multiplication takes two matrices and yields another matrix, and so we know that our final diagram will have two free wires. Much like an inner product one simply connects the inner wires,

$$\begin{array}{c} i \\ \text{---} \end{array} \boxed{M} \text{---} \boxed{M} \begin{array}{c} \text{---} \\ j \end{array} = M_k^i M_j^k = M^2. \quad (1.38)$$

We do the same to the result of equation (1.37),

$$\begin{array}{c} i \\ \text{---} \end{array} \begin{array}{c} \Psi \\ \times \\ \Psi \end{array} \begin{array}{c} \Psi \\ \times \\ \Psi \end{array} \text{---} \begin{array}{c} \Psi \\ \times \\ \Psi \end{array} \begin{array}{c} \Psi \\ \times \\ \Psi \end{array} \begin{array}{c} \text{---} \\ j \end{array} = \Psi^{ik} \Psi_{lk} \Psi^{lm} \Psi_{jm} = \rho_A^2. \quad (1.39)$$

The final step is to connect the remaining wires and complete the overall trace,

$$\begin{array}{c} \text{---} \\ \text{---} \end{array} \begin{array}{c} \Psi \\ \times \\ \Psi \end{array} \begin{array}{c} \Psi \\ \times \\ \Psi \end{array} \begin{array}{c} \Psi \\ \times \\ \Psi \end{array} \begin{array}{c} \Psi \\ \times \\ \Psi \end{array} \begin{array}{c} \text{---} \\ \text{---} \end{array} = \Psi^{ik} \Psi_{lk} \Psi^{lm} \Psi_{im} = \text{Tr}(\rho_A^2). \quad (1.40)$$

Also note that by exchanging the two kets we have an equivalent expression,

$$\begin{array}{c} \text{---} \\ \text{---} \end{array} \begin{array}{c} \Psi \\ \times \\ \Psi \end{array} \begin{array}{c} \Psi \\ \times \\ \Psi \end{array} \begin{array}{c} \Psi \\ \times \\ \Psi \end{array} \begin{array}{c} \Psi \\ \times \\ \Psi \end{array} \begin{array}{c} \text{---} \\ \text{---} \end{array} = \text{Tr}(\rho_B^2) = \text{Tr}(\rho_A^2), \quad (1.41)$$

which also holds true for higher powers of the density matrices.

1.5 Extracting Entanglement Entropy from the ground-state wavefunction

Numerical techniques such as exact diagonalization give us the full groundstate wavefunction to work with, without having to sample it, as is necessary in quantum Monte Carlo.

But to extract the entanglement entropy we still need to get from $\begin{array}{c} i \\ \text{---} \end{array} \begin{array}{c} \Psi \\ \triangleright \end{array}$ to $\begin{array}{c} a \\ \text{---} \\ b \\ \text{---} \end{array} \begin{array}{c} \Psi \\ \triangleright \end{array}$.

which is exactly what is done computationally.

From this point, with access to the reduced density matrix ρ_A , *any* of the Renyi entropies can be obtained by numerically calculating any power of ρ_A directly (even non-integer powers) using Equation (1.9). With Monte Carlo simulations, as discussed in Chapter 2, we can only calculate quantities representable by tensor diagrams (see Section 1.4 for more information on tensor diagram notation). Additionally, the more copies of the wavefunction that are used in the diagram, the more difficult the Monte Carlo calculation becomes.

Chapter 2

Valence Bond Projector Quantum Monte Carlo

The algorithm portion of this chapter was heavily covered in the author's M.Sc. thesis [36] though many additional details have been added. For a more thorough background please refer there. Results from the author's work on references [37] and [35] are presented here along with updated results and original content.

The valence bond (VB) quantum Monte Carlo (QMC) method developed by Sandvik in 2005 is a technique used to simulate the groundstate wavefunction of the Heisenberg model (and similar models) using a basis of VB states (briefly discussed in Section 1.2.2) instead of the traditional S^z spin basis [59]. This highly-efficient method projects out the model's groundstate by repeated application of the Hamiltonian to a trial wavefunction, through a Monte Carlo sampling of bond operators.

Section 2.1 will cover the basics of VB QMC algorithms. The following section will discuss the loop algorithm, an extremely efficient form of the VB QMC. Section 2.3 outlines the method used to measure the Renyi entanglement entropies in a groundstate projector QMC, such as the VB QMC. Then in Section 2.4 we discuss how this measurement is efficiently used in a modified version of the loop algorithm [63] called the loop-ratio algorithm. Finally, in Section 2.5 the loop-ratio algorithm for VB QMC, is used to study entanglement scaling in the 2D Heisenberg model groundstate [37, 35].

2.1 Review of Valence Bond quantum Monte Carlo

For a more detailed explanation of this technique I would direct the reader to the author's M.Sc. Thesis [36] or [3, 59, 62, 63].

The VB QMC method projects out the groundstate wavefunction of a system by applying a high power of the Hamiltonian \mathcal{H}^M to a trial wavefunction. If we expand the trial wavefunction out in terms of energy eigenstates, where the magnitude of the eigenvalue is largest for state $|0\rangle$ then we have,

$$\mathcal{H}^M|\psi\rangle = \sum_{n=0} c_n \mathcal{H}^M|n\rangle = \sum_{n=0} c_n E_n^M |n\rangle = E_0^M \left(c_0|0\rangle + \sum_{n=1} c_n \left(\frac{E_n}{E_0}\right)^M |n\rangle \right), \quad (2.1)$$

where $E_0 > E_n$ for $n > 0$. The fraction E_n/E_0 is always less than 1, so as it is raised to higher powers these terms vanish leaving only,

$$\mathcal{H}^M|\psi\rangle \approx E_0^M c_0|0\rangle, \quad (2.2)$$

a state proportional to $|0\rangle$. Outside of condensed matter physics this is simply called “the power method”.

In this chapter the VB QMC method is applied to the antiferromagnetic (AF) spin- $\frac{1}{2}$ Heisenberg model,

$$\mathcal{H}_{\text{Heis}} = J \sum_{\langle ij \rangle} \mathbf{S}_i \cdot \mathbf{S}_j, \quad (2.3)$$

discussed in Section 1.2.2.

The power method works to project out the eigenstate corresponding to the eigenvalue of largest magnitude. To project out the groundstate for the Heisenberg model the Hamiltonian must be modified,

$$\mathcal{H}_{\text{Heis}} \Rightarrow \mathcal{H}_{\text{proj}} = \sum_{\langle ij \rangle} \left(\frac{1}{4} - \mathbf{S}_i \cdot \mathbf{S}_j \right), \quad (2.4)$$

by subtracting it from $\frac{1}{4}$ per pair of nearest-neighbour sites. Table 2.1 shows how this new Hamiltonian $\mathcal{H}_{\text{proj}}$ affects the energies of different 2-spin and full lattice states.

Thus the modification in equation (2.4) takes the groundstate of the 2-site system from the lowest possible energy to the largest possible energy, causing the original groundstate to be the state which is eventually projected out through repeated application of this

State	$ \uparrow\uparrow\rangle, \downarrow\downarrow\rangle$	$\frac{1}{\sqrt{2}}(\uparrow\downarrow\rangle + \downarrow\uparrow\rangle)$	$ \uparrow\downarrow\rangle, \downarrow\uparrow\rangle$	$\frac{1}{\sqrt{2}}(\uparrow\downarrow\rangle - \downarrow\uparrow\rangle)$
2-site $\langle \mathcal{H}_{\text{Heis}} \rangle$	1/4	1/4	-1/4	-3/4
Lattice $\langle \mathcal{H}_{\text{Heis}} \rangle$	$N_b/4$	$E < N_b/4$	$-N_b/4$	$-N_b/4 \geq E > -3N_b/4$
2-site $\langle \mathcal{H}_{\text{proj}} \rangle$	0	0	1/2	1
Lattice $\langle \mathcal{H}_{\text{proj}} \rangle$	0	$E > 0$	$N_b/2$	$N_b/2 \leq E < N_b$

Table 2.1: The energies for the 2-site and full lattice Heisenberg interactions along with the energies for the modified projector Hamiltonian in Equation (2.4).

Hamiltonian $\mathcal{H}_{\text{proj}}$ to a trial state. In the case of a lattice of more than two sites, not every nearest-neighbour bond can have this singlet groundstate (as discussed in Section 1.2.2), but we do know that the energy per bond must be between that of $|\uparrow\downarrow\rangle$ (which *can* be extended to a square lattice) and the valence bond state. Thus the groundstate of $\mathcal{H}_{\text{Heis}}$, which is necessarily the lowest energy state on the full lattice, will have the largest energy for the projector Hamiltonian $\mathcal{H}_{\text{proj}}$.

Setting $J = 1$ we rewrite $\mathcal{H}_{\text{proj}}$ as a series of *bond operators* H_{ij} acting on pairs of nearest-neighbour sites,

$$\mathcal{H}_{\text{proj}} = \sum_{\langle ij \rangle} H_{ij}, \quad H_{ij} = \frac{1}{4} - \mathbf{S}_i \cdot \mathbf{S}_j. \quad (2.5)$$

Then the Hamiltonian raised to the power M can be written as a sum of all possible arrangements of M bond operators including repetitions,

$$\mathcal{H}_{\text{proj}}^M = \left(\sum_{\langle ij \rangle} H_{ij} \right)^M = \sum_{k_1=1}^{N_b} \cdots \sum_{k_M=1}^{N_b} H_{k_1} \cdots H_{k_M}, \quad (2.6)$$

where in the final portion of the equation a pair of sites i, j is represented by a single number k_x , and N_b is the total number of nearest-neighbour bonds in the lattice. This will yield $(N_b)^M$ different combinations of bond operators.

From this point, there are three different types of VB QMC algorithms:

- Single Projector – a VB QMC technique used to project out one copy of the groundstate wavefunction. This method is ideal for studying the groundstate energy, but not much else [59].

- Double Projector – a technique which projects out two independent copies of the groundstate wavefunction. This method can be used to measure expectation values of operators [3].
- Loop Algorithm – a more efficient double projector method in which Monte Carlo moves are always accepted [63].

All three methods are discussed in the author’s M.Sc. thesis [36], and it has previously been shown that the entanglement entropy can be measured in the double projector method by calculating the expectation value of a *Swap* operator [25]. Since the initial discovery of this method to measure the Renyi EEs, a new technique has been developed to efficiently measure these EEs using the loop algorithm.

2.2 The Loop Algorithm

The loop update for VB QMC simulations was introduced in Ref. [63] as a highly efficient way of carrying out the sampling procedure. This scheme samples over states in the valence bond basis, but also over states in the spin basis. The combined spin/bond basis eliminates the need for a rejection step in the Monte Carlo algorithm, and thus samples operators and basis states with high efficiency.

To begin, operators in this case are divided into two types,

$$H_{ij}(1) = \left(\frac{1}{4} - S_i^z S_j^z\right) \quad (2.7)$$

$$H_{ij}(2) = -\frac{1}{2}(S_i^+ S_j^- + S_i^- S_j^+) \quad (2.8)$$

called diagonal and off-diagonal operators respectively, where the sum $H_{ij}(1) + H_{ij}(2)$ is equal to the bond operators H_{ij} from the standard VB QMC algorithms, defined in Equation (2.5) above [3, 59, 62]. Following Equation (2.6), this separation of diagonal and off-diagonal terms gives us,

$$\mathcal{H}_{\text{proj}}^M = \left(\sum_{\langle ij \rangle} H_{ij}(1) + H_{ij}(2) \right)^M = \sum_{k_1=1}^{N_b} \sum_{y_1=1}^2 \cdots \sum_{k_M=1}^{N_b} \sum_{y_M=1}^2 H_{k_1}(y_1) \cdots H_{k_M}(y_M), \quad (2.9)$$

resulting in a multiplicative factor of 2^M times as many terms in the list of possible strings of Hamiltonian operators.

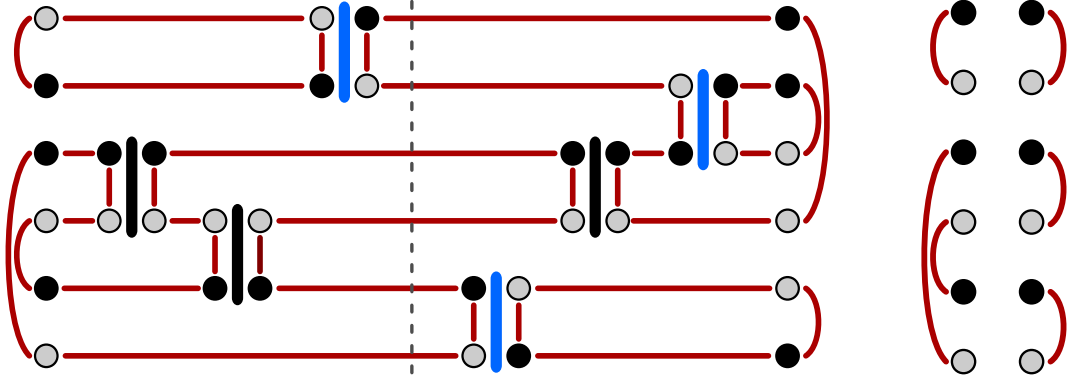


Figure 2.1: **(Left)** A possible simulation cell diagram for a one dimensional 6-site system, including loops, operators, the initial valence bond states, and the compatible initial spin states. Up (down) spins are shown in grey (black). (Off-) diagonal operators are shown in (blue) black, giving a total of $M = 3$ operators in this example. The dashed line denotes $\langle V_L|$ (propagated from the trial state on left) and $|V_R\rangle$ (similarly from the right). **(Right)** The propagated VB states extracted from the simulation cell on the right. Note that the propagated spin states, $\langle Z_L|$ and $|Z_R\rangle$, must always agree.

The projected groundstate of the system is then

$$\begin{aligned}
 |\Psi\rangle &= \mathcal{H}_{\text{proj}}^M |T_R\rangle = \left(\sum_{\langle ij \rangle} H_{ij}(1) + H_{ij}(2) \right)^M |T_R\rangle \\
 &= \sum_{k_1=1}^{N_b} \sum_{y_1=1}^2 \cdots \sum_{k_M=1}^{N_b} \sum_{y_M=1}^2 H_{k_1}(y_1) \cdots H_{k_M}(y_M) |T_R\rangle \\
 &= \sum_{i=1}^{(2N_b)^M} P_i |T_R\rangle = \sum_{i=1}^{(2N_b)^M} |V_R^i\rangle. \tag{2.10}
 \end{aligned}$$

In other words, the Hamiltonian is applied to the trial state $|T_R\rangle$, M times, which can be written as a sum of lists of M operators. These $(2N_b)^M$ lists of M operators can be consolidated under the label P_i . Applying the i^{th} list of these operators to the trial state $|T_R\rangle$ results in a new projected state $|V_R^i\rangle$. The loop algorithm samples the different lists of operators (i.e. the different P_i 's) and thus samples the various projected states $|V_R^i\rangle$. The normalized sum of these projected states, proportional to how often they are sampled, is equal to the groundstate wavefunction of the system (the 2D Néel state).

The loop algorithm is best visualized using a diagram of the simulation cell showing the placement of valence bonds, spins, and operators, as depicted in Figure 2.1. This diagram

represents two VB trial states $\langle T_L |$ and $|T_R\rangle$ (the left and right edges of the left panel of the figure) where each red line corresponds to a VB between the sites at its end points, and up (down) spins are represented by grey (black) circles. Each of the two trial states is projected “inwards” (by $M = 3$ operators in this case). The operators act to join the two incoming sites in a valence bond. Diagonal (off-diagonal) operators are shown in black (blue). The off-diagonal operators swap the spins between the two incoming sites, while the diagonal ones will leave the spin states as they were.

The projected states occur in the centre of the diagram, denoted by the dashed line. One can find the projected VB state by cutting the diagram along the dashed line and then tracing the VB lines from a starting site along the cut to its final site on the left side for $\langle V_L | = \langle T_L | H_{i,j}^3(y)$ and on the right side for $|V_R\rangle = H_{i,j}^3(y) |T_R\rangle$. Spins along a horizontal red line are always the same, whereas spins flip along a vertical connecting line. The projected states are shown on the right side of Figure 2.1.

2.2.1 Algorithm

Along with the trial VB states, initial spin states are selected at random, with the condition that the two spins in a single VB must be antiparallel. For each trial state, M operators are chosen such that they each act on a neighbouring pair of antiparallel spins (in the initial step of the algorithm, these are all diagonal operators). There are then two types of updates: spin updates and operator updates.

For the spin update, loops are first constructed by linking the operators and valence bonds (shown in Figure 2.1). Then, for each loop that is built, with probability $1/2$ all spins in the loop are flipped. This update samples possible spin states for the given valence bond configuration, and can change bond operator types from diagonal to off-diagonal (and vice versa) if only part of the operator is contained in a flipped loop.

In the second type of update, diagonal operators taken and re-sampled at random (i.e. they are replaced by another diagonal operator which may or may not be acting on the same pair of sites), subject to the condition that they remain acting on nearest-neighbour pairs of sites with antiparallel spins. This update will change the configuration of the loops and thus samples the possible valence bond states for a given spin configuration.

Switching back and forth between the spin and VB picture allows the algorithm to efficiently sample the groundstate without the need to ever reject an update.

2.2.2 Measurements

Measurements can be computed as expectation values using the propagated valence bond states, $|V_L\rangle$ and $|V_R\rangle$, which can be extracted from the simulation cell diagram as demonstrated in Figure 2.1. For an operator \mathcal{O} , its groundstate expectation value is

$$\langle \mathcal{O} \rangle = \frac{\langle \Psi | \mathcal{O} | \Psi \rangle}{\langle \Psi | \Psi \rangle}, \quad (2.11)$$

where $|\Psi\rangle$ represents the full groundstate wavefunction of the system as in Equation (2.10). During the simulation both the numerator and denominator are sampled at each measurement step, not the combined fraction. That is, we look at the overlap of $\langle V_L^i | V_R^j \rangle$ and measure the expectation value of the operator $\langle V_L^i | \mathcal{O} | V_R^j \rangle$, adding each to their own separate tally. This is the proper way to do measurements, since we are not measuring the full wavefunction at each step in the simulation, but instead sampling terms from the wavefunction, and in general,

$$\frac{\sum_{i=1}^N a_i}{\sum_{j=1}^N b_j} \neq \frac{1}{N} \left(\sum_{i=1}^N \frac{a_i}{b_i} \right). \quad (2.12)$$

Measurements are taken after some number of steps after which the new projected states are no longer correlated with the old projected states. For the loop algorithm this is on the order of one to ten steps, while for the double or single projector algorithm this could take 10s to 1000s of steps depending on one's choice of simulation parameters [63]. The autocorrelation should be checked when writing any new Monte Carlo algorithm, as it is ideal to measure after the minimum number of steps for which the states are uncorrelated. Waiting too long between measurements is a waste of resources as relevant data is not being recorded.

2.3 Measuring Renyi Entanglement Entropies with VB QMC

Numerical techniques such as exact diagonalization or Lanczos are able to directly measure the Renyi entanglement entropies using the method described in Section 1.5. Density matrix renormalization group (DMRG) calculations give direct access to the reduced density matrices of different region A s and it is therefore even easier to extract the EEs from DMRG [64, 86].

In contrast, it is typically a challenge to measure EE with QMC, as the density matrix is not obtained in a straightforward way, but rather terms from the wavefunction are sampled throughout the simulation. There have been many proposals over the years for Monte Carlo measurements that in some special cases will give information about a system’s entanglement [2, 71, 45]. Recently a method to measure integer Renyi entanglement entropy (for $\alpha > 1$) using a “swap” [25] (or more generally a permutation [8]) operator has been developed and implemented in several types of QMC [25, 47, 37].

The remainder of this section will outline the basic methodology for extracting the entanglement entropy using VB basis QMC [25], based on the expectation value of the *Swap* operator, as well as a method of improve the efficiency of that measurement.

2.3.1 Renyi Entanglement Entropies and the “Replica Trick”

The Renyi entanglement entropies, discussed in Section 1.1, which quantify entanglement between a system divided into two regions, A and B , are defined as

$$S_\alpha = \frac{1}{1 - \alpha} \ln [\text{Tr}(\rho_A^\alpha)]. \quad (2.13)$$

For more on the properties of the Renyi EEs see Section 1.1 and the text surrounding Equation (1.9).

Despite the inaccessibility of the full wavefunction of a system when using Monte Carlo techniques, it is possible to sample $\text{Tr}(\rho_A^\alpha)$ for integer $\alpha > 1$. This is accomplished by taking the expectation value of a *Swap* operator [25] for $\alpha = 2$ or permutation operator for $\alpha > 2$; [8, 37] e.g.

$$S_2 = -\ln(\langle \text{Swap}_A \rangle) = -\ln(\langle \Pi_2^A \rangle) \quad (2.14)$$

$$S_3 = -\frac{1}{2} \ln(\langle \Pi_3^A \rangle) \quad (2.15)$$

$$S_\alpha = \frac{1}{1 - \alpha} \ln(\langle \Pi_\alpha^A \rangle). \quad (2.16)$$

To measure the α^{th} entropy, each of the projected states $\langle V_L |$ and $|V_R\rangle$ must be composed of α non-interacting copies of the system (“replicated” α times), for a total of 2α copies of the system in the simulation. This procedure is called the “replica trick”. The permutation operators Π_α^A act to cyclically exchange the state in region A between the α different copies of the system, and are constructed such that $\langle \Pi_\alpha^A \rangle = \text{Tr}(\rho_A^\alpha)$ (see Equation

2.22). In the case of spin states (which for each MC step in the simulation is an unentangled product state) we can simply swap the states within region A between copies of the system. For valence bond states the application of the permutation operator also has a simple result; it acts to exchange the endpoints of valence bonds within region A between copies of the system, and as such can create bonds between the non-interacting copies [25], see e.g. Figure 2.3.

It can be shown using the tensor diagram notation (TDN) from Section 1.4, how the expectation values of operators in (2.14) - (2.16) are equivalent to the measurement of $\text{Tr}(\rho_A^\alpha)$. Note that the same derivation is done in Reference [25] without the use of TDN.

Expectation values are calculated as in equation (2.11), sampling the overlap between independently projected terms in the wavefunction $\langle V_L^i |$ and $|V_R^j\rangle$, before and after the operator in question is applied to $|V_R^j\rangle$. The difference with the $Swap_A$ operator (for S_2) and the permutation operator Π_α^A (for $S_\alpha, \alpha \geq 3$), compared to standard operators, is that they act on α copies of the groundstate wavefunction, $|\Psi\rangle^{\otimes\alpha}$.

Using TDN, a QMC simulation measuring an operator \mathcal{O} looks like,



A tensor diagram representing the measurement of an operator \mathcal{O} . It consists of a central square box labeled \mathcal{O} . To the left of the box is a double-headed arrow pointing left, containing the symbol Ψ . To the right of the box is a double-headed arrow pointing right, also containing the symbol Ψ . A horizontal line connects the left arrow to the box, and another horizontal line connects the box to the right arrow.

(2.17)

forgetting about the normalization for now. The measurement of the $Swap_A$ operator looks like this:



A tensor diagram representing the measurement of the $Swap_A$ operator. It shows two rows of double-headed arrows, each containing the symbol Ψ . The top row has two arrows pointing left and right. The bottom row also has two arrows pointing left and right. Black horizontal lines connect the left arrows of the top and bottom rows, and the right arrows of the top and bottom rows. Two red curved lines cross each other in the center, connecting the left arrow of the top row to the right arrow of the bottom row, and the right arrow of the top row to the left arrow of the bottom row.

(2.18)

where the red lines denote the wavefunction in region A , and the black lines represent the state in region B . The $Swap_A$ operator *swaps* the states in region A between the two copies of the system. The TDN diagram can be rearranged as long as the connections are unchanged, and it will represent an equivalent expression. It can be shown that this diagram is equivalent to that in (1.40) representing $\text{Tr}(\rho_A^2)$.

(2.19)

First the bottom left bra is shifted to the right.

(2.20)

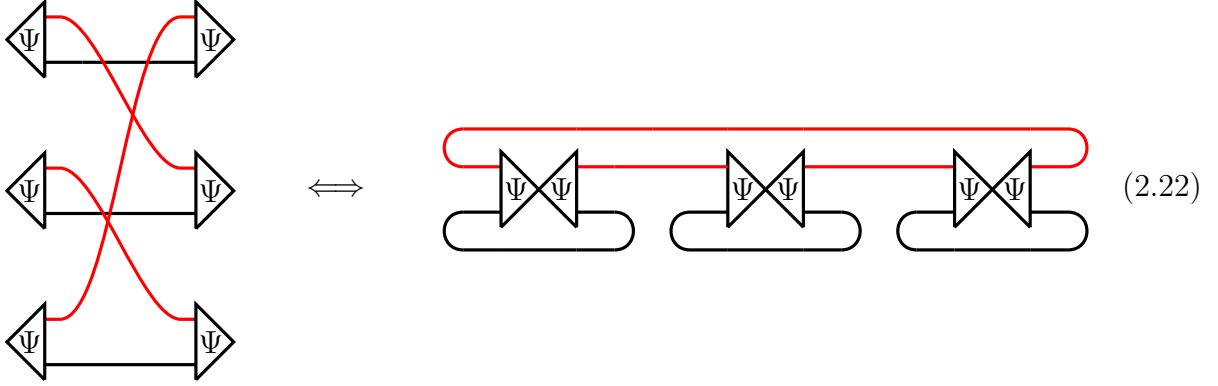
The top right ket is shifted to the left.

(2.21)

Finally the lower bra and ket are shifted up to recover the tensor diagram for $\text{Tr}(\rho_A^2)$. As in Equation (1.41), it is also possible to show that $\text{Tr}(\rho_A^2) = \text{Tr}(\rho_B^2)$, as in Equation (1.41), and thus either the $Swap_A$ or the $Swap_B$ operator can be applied to get the correct expectation value.

Below the permutation operator picture (left) and the equivalent $\text{Tr}(\rho_A^\alpha)$ picture (right)

are shown for $\alpha = 3$.



The same type of relation holds for higher α Renyi entropies, though they become increasingly computationally difficult to measure since they require 2α independently sampled groundstate wavefunctions.

The “bare” measurement of the $Swap_A$ operator (2.18) has been shown [25] to have problems with convergence for a larger region A , while in principle the measurement should be symmetric such that $\langle Swap_A \rangle = \langle Swap_B \rangle$, since the two density matrices ρ_A and ρ_B have the same eigenvalues. This is because the exchange of a larger region gives a larger number of different states as a result of that swap, and thus a larger range and number of possible values in the expectation value. It simply takes more Monte Carlo steps to converge upon the same result. Another way to think of it is that, even though $\text{Tr}(\rho_A^2) = \text{Tr}(\rho_B^2)$, if region A is much larger than region B then ρ_A (and by extension ρ_A^2 and $\text{Tr}(\rho_A^2)$) contains exponentially more terms than ρ_B , ρ_B^2 and $\text{Tr}(\rho_B^2)$. Getting the value to converge by a stochastic sampling of these terms takes much longer. However, it is possible to instead sample a series of smaller regions and greatly improve the convergence time. This technique is called the *Ratio Trick*.

2.3.2 The Ratio Trick

The convergence issue mentioned above can be addressed by a reweighting of the Monte Carlo sampling scheme. In the loop algorithm the expectation value of the $Swap$ operator is measured by sampling terms from

$$\langle Swap_A \rangle = \frac{\langle \Psi \otimes \Psi | Swap_A | \Psi \otimes \Psi \rangle}{\langle \Psi \otimes \Psi | \Psi \otimes \Psi \rangle} = \frac{\sum_i \sum_j \langle V_L^i | Swap_A | V_R^j \rangle}{\sum_k \sum_l \langle V_L^k | V_R^l \rangle} \quad (2.23)$$

where $|\Psi\rangle$ is the groundstate wavefunction and $|V_L\rangle, |V_R\rangle$ are the states obtained by applying lists of bond operators to the trial states $\langle T_L|$ and $|T_R\rangle$ (see Equation (2.10)).

Using the ratio trick, instead of swapping just one region, the *ratio* of the swap operators for two different region is calculated. The regions are chosen such that they are close in size (this is important, as the difference in region sizes is the main factor affecting convergence of the measurement). The normalizations cancel out and we are left with,

$$\frac{\langle Swap_A \rangle}{\langle Swap_{A'} \rangle} = \frac{\langle \Psi \otimes \Psi | Swap_A | \Psi \otimes \Psi \rangle}{\langle \Psi \otimes \Psi | Swap_{A'} | \Psi \otimes \Psi \rangle} = \frac{\sum_{ij} \langle V_L^i | Swap_A | V_R^j \rangle}{\sum_{kl} \langle V_L^k | Swap_{A'} | V_R^l \rangle}. \quad (2.24)$$

This measurement will show improved convergence over (2.23) since, if regions A and A' are similar in size, the measurement $\langle V_L | Swap_A | V_R \rangle / \langle V_L | Swap_{A'} | V_R \rangle$ will have fewer possible values than $\langle V_L | Swap_A | V_R \rangle / \langle V_L | V_R \rangle$, and those values will have a smaller variance.

It is important to remember however that one is measuring a *ratio* of expectation values. To obtain $\langle Swap_A \rangle$, one must know the value of $\langle Swap_{A'} \rangle$. If $\langle Swap_{A'} \rangle$ was measured using $\langle Swap_{A'} \rangle / \langle Swap_{A''} \rangle$ then we also need to know $\langle Swap_{A''} \rangle$ to find $\langle Swap_{A'} \rangle$, and so on. Thus, the procedure is to measure a chain of ratios of region sizes building up to region A , beginning with a measurement of the bare *Swap* for a small region size, increasing the size of regions A and A' over several simulations in sequence. That is, we measure *Swap* for a sequence of different region sizes, A_1, A_2, \dots, A_n , where the number of lattice sites in A_{i+1} is greater than the number of sites in region A_i . Then, the Renyi EE of the final intended region A_n is calculated using

$$\begin{aligned} S_2(A_n) = & -\ln \left(\frac{\langle Swap_{A_n} \rangle}{\langle Swap_{A_{n-1}} \rangle} \right) - \ln \left(\frac{\langle Swap_{A_{n-1}} \rangle}{\langle Swap_{A_{n-2}} \rangle} \right) \\ & - \dots - \ln \left(\frac{\langle Swap_{A_2} \rangle}{\langle Swap_{A_1} \rangle} \right) - \ln (\langle Swap_{A_1} \rangle) \end{aligned} \quad (2.25)$$

where each ratio is calculated via Equation (2.24), and the last expectation value for A_1 via Equation (2.23).

Note that each term in the sum requires a separate VB QMC simulation since, although we can measure the *Swap* operator for any region A within one simulation, we can only use *one* region size A' in the denominator per simulation, since it directly affects the topology of the simulation cell as described below. The scaling cost of the ratio trick is therefore n ; however, the gain in sampling efficiency is demonstrated to more than compensate for this additional simulation cost.

2.4 The Loop-Ratio Algorithm

Initially the ratio trick was only employed using the double projector algorithm, a less efficient form of VB QMC than the loop algorithm [25]. However, with input from one of the pioneers of the VB QMC loop algorithm, Hans Gerd Evertz, we were able to modify the loop algorithm for use with the ratio trick [37]. This new algorithm was named the loop-ratio algorithm, combining the increased efficiency of the loop algorithm with the improved sampling of the ratio trick.

In order to make the necessary modifications to the loop algorithm, the system is replicated so that two (or α for S_α) non-interacting copies of $\langle V_L |$ and $|V_R\rangle$ are present, as is usual for measurements of the *Swap* (or permutation) operator [25]. Then, links in the simulation cell are reconnected as if there were a $Swap_{A'}$ operator permanently applied to the projected state $|V_R\rangle$, shown in Figures 2.2 and 2.3. This causes spins from the different non-interacting copies of the system to be connected via loops, which means they can be flipped together, and thus the spin states are sampled according to the swapped system $\langle V_L | Swap_{A'} | V_R \rangle$. The measurement of $\langle V_L | Swap_A | V_R \rangle / \langle V_L | Swap_{A'} | V_R \rangle$ is then accomplished by measuring an operator which swaps the states of the sites in region A that were *not* already swapped in region A' , assuming $A' \subset A$.

It is clear from the above then, why only one value of A' can be used for a given simulation, since it changes the topology of the simulation cell in a distinct way for a given A' . And so the region to be measured must be built up in small increments of A' with a series of simulations according to Equation (2.25).

2.5 Anomalies in the Entanglement Properties of the Square Lattice Heisenberg Model

The Heisenberg model (Section 1.2.2) is one of the most well studied models in condensed matter physics. But prior to 2010 there was not yet a suitable method with which to study entanglement using QMC. Entanglement scaling studies were restricted small systems using exact diagonalization, or quasi-1D systems with DMRG calculations, or analytical techniques requiring assumptions and approximations (outside of the few special cases that are analytically exactly solvable).

Implementing the *Swap* operator technique for measuring Renyi entropies in QMC made available to us a wealth of information about the entanglement scaling of the Heisenberg groundstate. We found there is more to the story than simply the area law scaling

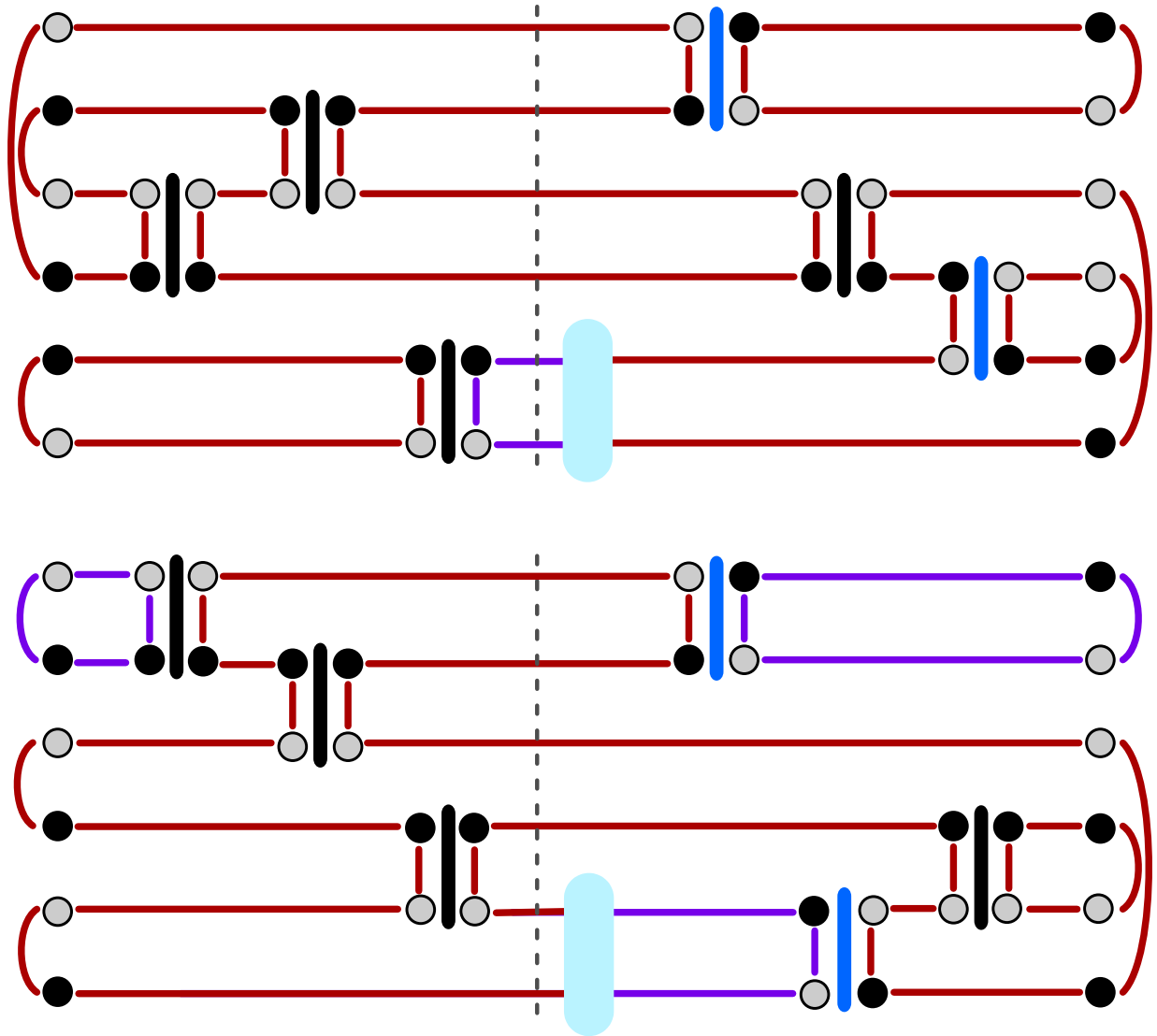


Figure 2.2: One possible simulation cell configuration for the loop-ratio algorithm on a 6-site system where $\alpha = 2$ and region A' contains the first two sites of the system. Spins between the usually non-interacting copies are connected through loops via the *Swap* operator (light blue). The red and purple links are used to show the connections between the sheets. The loop on the left side of the swap operator on the top sheet is connected to the right side on the bottom sheet and so forth.

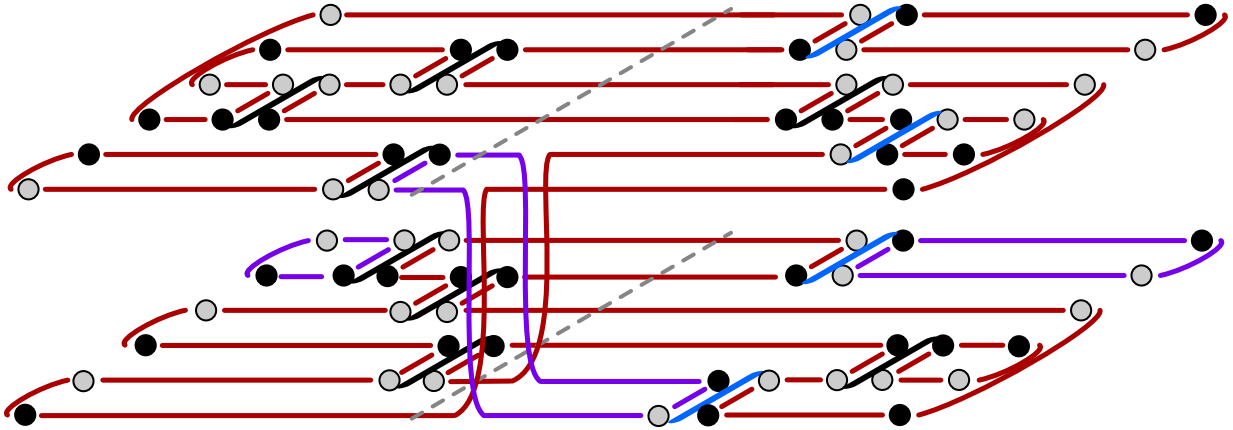


Figure 2.3: A three dimensional view of the loop-ratio simulation cell in Figure 2.2, showing the connections between the two simulation layers via the $Swap_A$ operator.

that was expected. There is also a subleading logarithmic correction due to the gapless Goldstone modes [37, 49], a subleading logarithm due to the presence of corners in a boundary, the coefficient of which could be universal [10], and an aspect-ratio dependent term which could point the way toward a new universal quantity analogous to the central charge found in 1D critical systems. These results are discussed below.

2.5.1 Results

We study the scaling of entanglement in the two dimensional square lattice spin- $\frac{1}{2}$ anti-ferromagnetic Heisenberg model using valence bond quantum Monte Carlo employing the loop-ratio algorithm [37].

Two different entanglement geometries are studied (shown in Figure 2.4 for a 6×6 lattice) the *strip* geometry and the *square* geometry [69]. The VB QMC is used to simulate the groundstate of $L \times L$ toroidal systems.

In the “strip” geometry region A is built up via the ratio trick adding successive $1 \times L$ strips until a region A of size $L/2 \times L$ is reached. For this geometry region A has no corners, since one dimension of the region wraps fully around the torus, and the length of the boundary between regions A and B is $\ell = 2L$.

The “square” geometry uses a similar method, starting from one site, and adding strips of sites to build successively larger square regions until the final region A of $L/2 \times L/2$ is

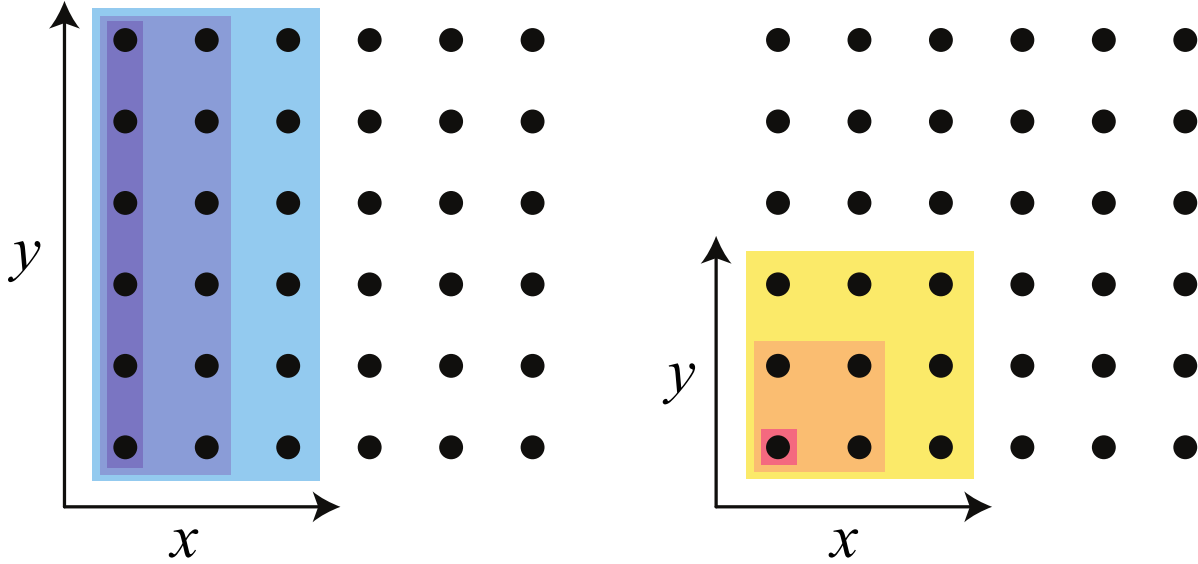


Figure 2.4: The strip (left) and square (right) geometries used to study entanglement in systems with periodic boundaries. The regions are built up using the ratio trick by adding successive strips or squares as illustrated.

reached. This geometry yields a region A with four corners, and the same boundary length of $\ell = 2L$.

Due to the use of the ratio trick, the region A s of interest must be built up using separate simulations according to Equation (2.25). Thus for each system size $L/2$ separate simulations are required to get to the intended region A .

Testing Convergence

The VB QMC algorithm in any of its forms requires a careful choice of the number of operators M applied to the trial state (see Equation (2.10)).

The choice of M involves a balance in algorithm efficiency versus accuracy. A large enough M is imperative for the algorithm to be able to converge to the correct result, but choosing too large an M will slow down the simulations by including unnecessary operators, and causing convergence to come much slower than is optimal.

The number is generally chosen to be proportional to the number of sites, N , so we work with the quantity $m = M/N$ when checking this convergence. Choosing a large

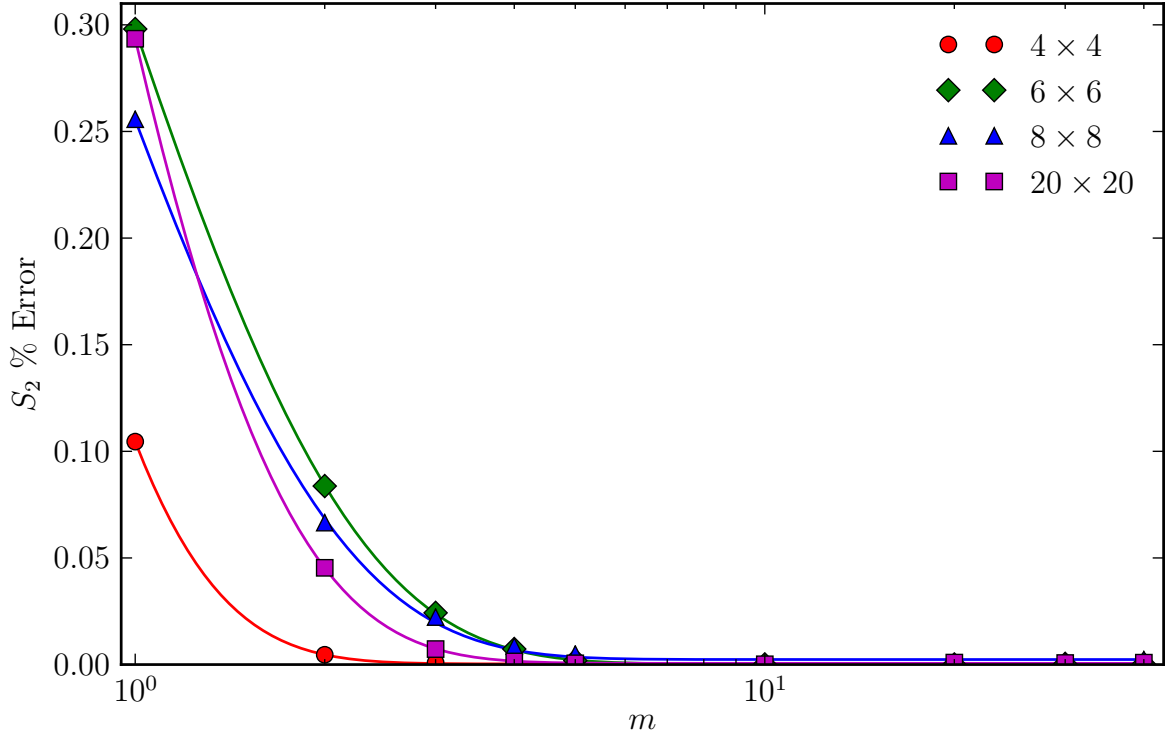


Figure 2.5: Percent error in S_2 versus the number of operators per site (m) for different $L \times L$ lattices. For $L = 4, 6, 8$ the lattices have open boundaries and region A is half the system using the strip geometry. The exact values were found using DMRG calculations [19]. The $L = 20$ lattice has periodic boundaries and A is a 2×2 square. The “exact” value is taken from the $m = 10$ simulation. Each data set was fit to an exponential function. The error bars are all significantly smaller than the data points used and were not included in this plot.

enough value of m ensures that each site is likely to have at least one, but ideally more, operators interacting with it. This way the projected state will be independent of the trial wavefunction used. The value of m is for *each* independent copy of the system, so for the measurement of the Renyi entanglement entropies that means the actual number of Hamiltonian operators in the operator list P_i is $4Nm = 4M$.

Figure 2.5 shows the measurement of S_2 for $L \times L$ square-lattice Heisenberg systems cut in half via the “strip” geometry, using the loop-ratio VB QMC algorithm. The smaller systems studied, $L = 4, 6, 8$, have open boundary conditions so they can be compared to exact results from DMRG calculations [19]. The 20×20 system is too large for DMRG and so the “exact” value is taken from the VB QMC simulations with $m = 10$, and the boundary conditions are periodic to reflect the geometries used in this QMC study.

From the plot, all system sizes are well converged to within 0.005% of the exact result by about $m = 5$. The subsequent data for this study uses a value of $m = 10$.

Area Law

Figure 2.6 shows examples of S_2 for regions A of both strip and square geometries of increasing width x for a 20×20 toroidal system. The length of the boundary for all strip regions in this plot is $\ell = 2L = 40$, whereas for the square regions $\ell = 4x$. The area law scaling (see section 1.3.2) of S_2 is apparent in the strip and square geometry results, as they both appear to approach a straight line with zero and non-zero slope respectively.

Subleading Logarithm

To determine the scaling of entanglement entropy in two dimensions with the length of the boundary ℓ , we examine $L \times L$ systems with periodic boundary conditions, the results of which are shown in Figure 2.7. The region A s are systematically built up according to the square and strip geometries as defined in Figure 2.4. In this case (as opposed to the plot in Figure 2.6), each data point in Figure 2.7 uses a region A with width $x = L/2$ proportional to the system size. This is done in an attempt to avoid dealing with the apparent aspect-ratio dependence of entanglement in gapless systems (discussed below) which, unlike for gapped systems, causes a deviation from the area law within a given system. This deviation can be seen for the strip geometry in Figure 2.6, and later in this section in Figure 2.8.

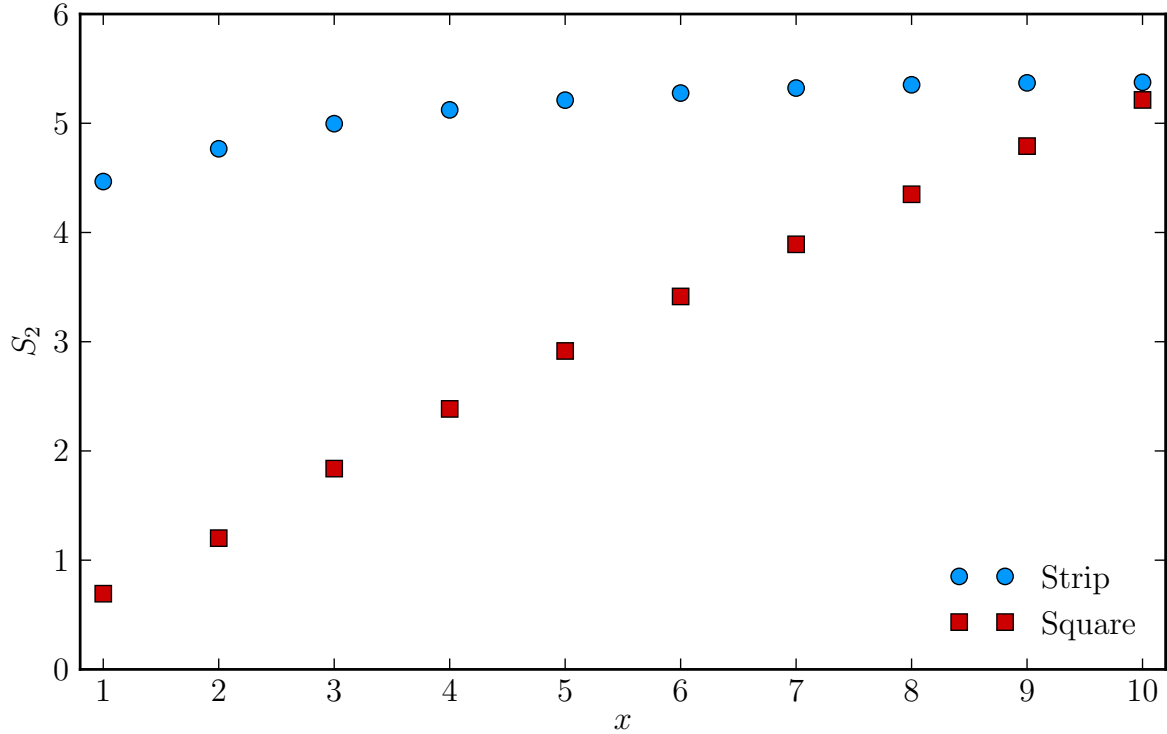


Figure 2.6: The second Renyi EE (S_2) for a 20×20 system with periodic boundaries versus the width (x) of region A for both the square and strip geometries. The boundary length does not change with the region width for strip geometry (since its height y traverses the periodic lattice), thus the entanglement entropy seems to approach a constant value. For the square geometry the boundary length is $4x$, and the entanglement entropy S_2 increases approximately proportionally. The scaling for both geometries becomes closer to linear in boundary length as the width of region A approaches half the system size.

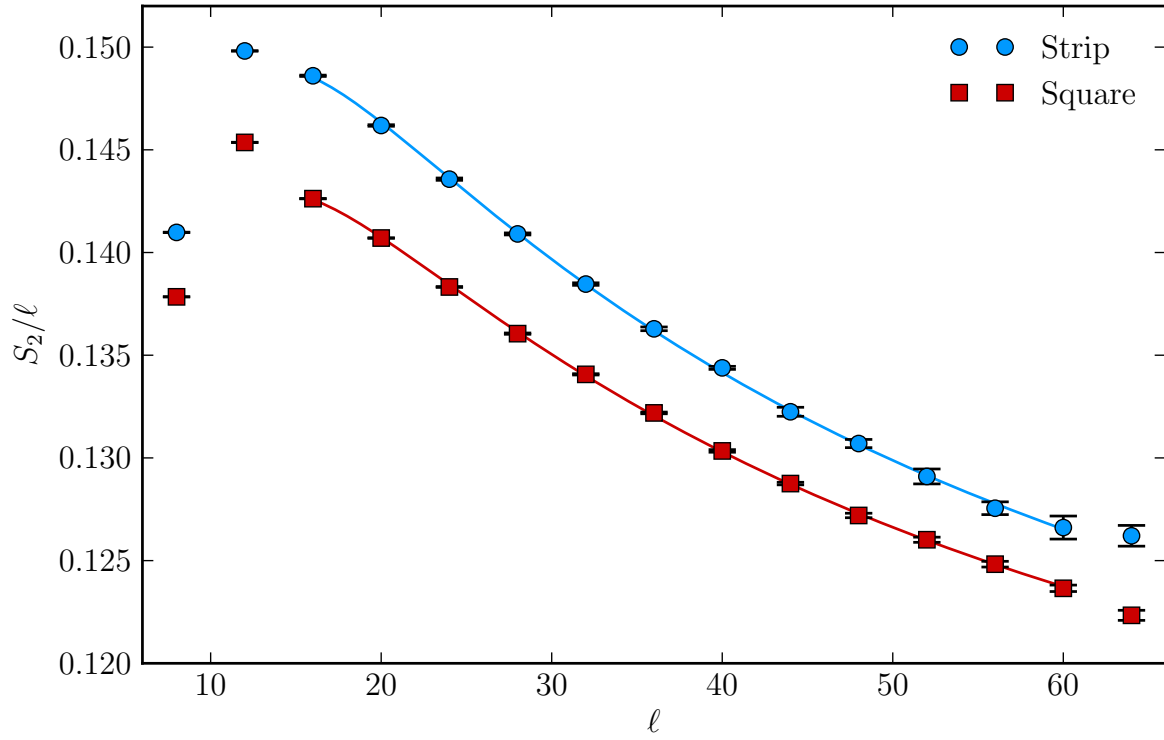


Figure 2.7: The entanglement entropy S_2 per unit boundary length (ℓ) vs ℓ for regions with square and strip geometries embedded in $L \times L$ systems with periodic boundary conditions. Region A has width $x = L/2$ for both geometries. Fits to Equation (2.26) are included and the coefficients found are listed in Table 2.2. The fits exclude the $\ell = 8, 12, 64$ data points.

As is clear from Figure 2.7, the data fit excellently to the function

$$\frac{S(\ell)}{\ell} = a + \frac{c}{\ell} \ln(\ell) + \frac{d}{\ell}, \quad (2.26)$$

(see Section 1.3.2 for more on 2D entanglement scaling) where ℓ is the length of the boundary between regions A and B , provided that the very smallest and largest lattice sizes are excluded. The values obtained for coefficients a, c , and d are listed below in Table 2.2.

geometry	a	c	$-d$
strip	0.0965(7)	0.74(2)	1.22(5)
square	0.0976(3)	0.64(1)	1.06(2)

Table 2.2: The coefficients a, c, d found by fitting the data in Figure 2.7 to Equation (2.26). The fits were done for both strip and square geometries at $x = L/2$.

After its discovery numerically, this subleading logarithm term for the strip geometry has been posited to be due to the presence of Goldstone modes in the Heisenberg model, with a predicted coefficient of $(d-1)N_G/2$, where d is the dimension of the system and N_G is the number of Goldstone modes [49]. For this system, in two dimensions, and with two Goldstone modes, this should give $c = 1$ where we see a distinctly lower value numerically. It is possible that this result is due to the finite system sizes used, or it could be the use of the second Renyi EE (S_2) instead of the first (S_1), which will give systematically lower values for anything other than maximally or minimally entangled states.

Corner Logarithm

The corner contribution to the subleading scaling of the entanglement entropy (Section 1.3.2), can be found by calculating the difference in the coefficient of the logarithmic term in Equation (2.26) for the square and the strip geometries.

$$\begin{aligned} c_{\text{corner}} &= \frac{1}{4} [0.64(1) - 0.74(2)] \\ &= -0.025(6) \end{aligned} \quad (2.27)$$

This value may be compared to coefficients obtained through other techniques, though there is little agreement.

Technique	c_{corner}	Reference
VB QMC	-0.025(6)	This work & [37]
Ising Series Expansion	-0.020(2)	[37]
Spin-Wave Theory	-0.0124	[37]
Scalar Field Theory	-0.0062	[10]

The scalar field theory should not be expected to agree, since it is for a non-interacting model which the Heisenberg model certainly is not. The spin-wave theory result should theoretically agree with the QMC result, but instead gives a lower value. The series expansion result, however, is in agreement with the Monte Carlo value.

In Sections 3.9.1 and 3.9.2 the corner term is studied in the transverse-field Ising model and the Heisenberg bilayer system. At the QCPs of these models the coefficient of the corner term should be universal.

Aspect-Ratio Dependence

Gapless wavefunctions typically have long-range correlations, so it is possible for the entanglement entropy to depend on the size and shape of the regions A and B . The 1D result (Equation (1.25)) is manifestly size-dependent, and here we see how a similar behaviour occurs in 2D.

By studying $L \times L$ torus systems with cylindrical region A_s (i.e. strip geometry) of dimensions $x \times L$ the boundary length is always $\ell = 2L$, but the ratio x/L changes. Figure 2.8 shows this shape dependence for system sizes from $L = 10$ to 40 (including only even L and excluding $L = 38$, which was not simulated). The results show a bow-like shape for each system, reflecting about $x = L/2$, as is necessary since $S_\alpha^A = S_\alpha^B$. The surprising part is that the bow-shape does not flatten out for larger sizes, indicating that there are contributions to entanglement on all length-scales in these systems. This curvature was first seen in Ref. [25] but not explored in detail (instead, using a fixed x/L the surprising subleading logarithmic term $\propto \ln(\ell)$ [discussed above] was found).

The data in Figure 2.8 are fit to the function

$$S_2 = c(L) \ln \left[\sin \left(\frac{\pi x}{L} \right) \right] + d, \quad (2.28)$$

analogous to the 1D CFT scaling in Equation (1.25). The coefficient c here, a universal number in the 1D case, is allowed to vary as a function of L . The constant d is able to absorb any multiplicative factors inside the logarithm, or any other additive terms.

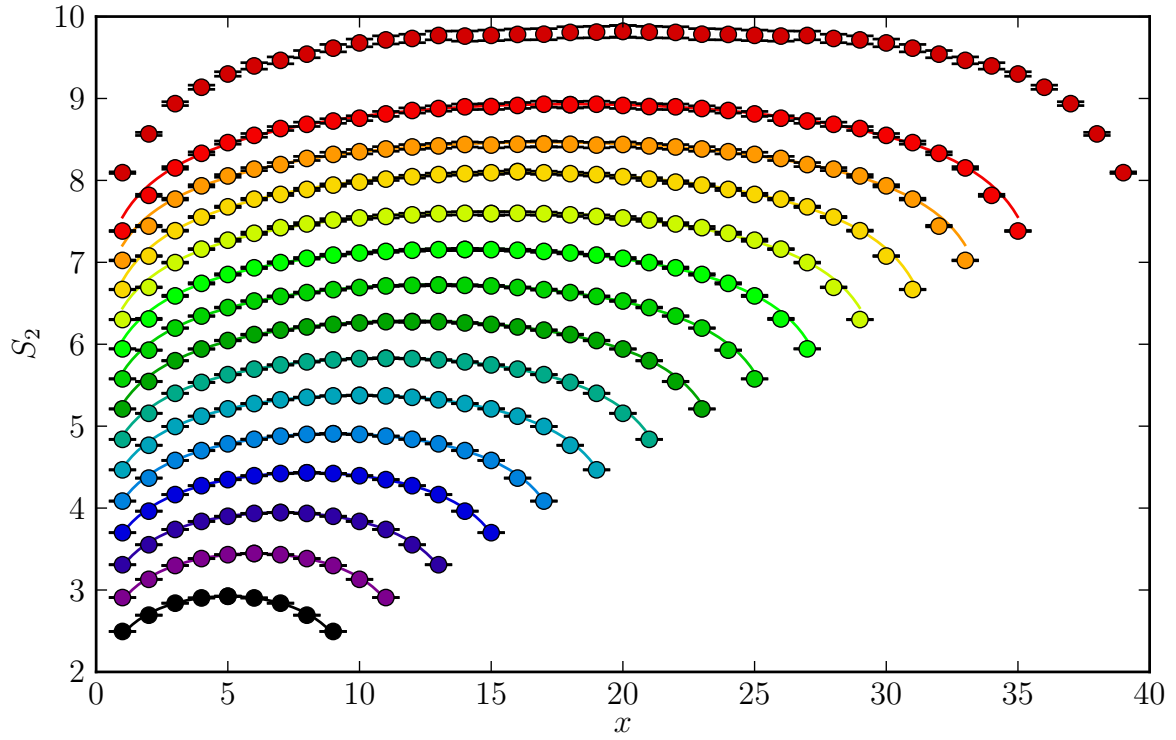


Figure 2.8: The entanglement entropy between a cylindrical region A and the remainder of the torus, on $L \times L$ systems for $L = 10, 12, 14, \dots, 34, 36,$ and 40 . As the width of region A (x) increases with respect to the length of the toroidal system (L) we see S_2 increase until it reaches a maximum values at $x = L/2$ and then the entanglement decreases in a symmetric fashion.

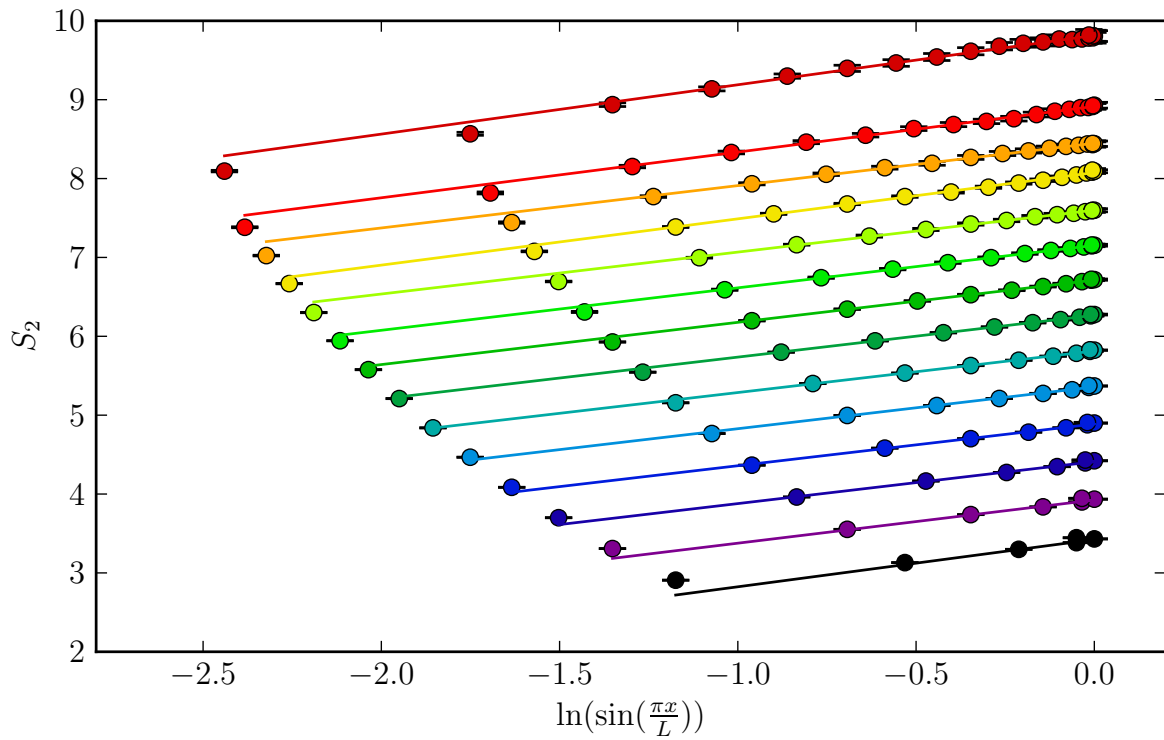


Figure 2.9: This figure contains the same data from Figure 2.8, plotted using the logarithm of the chord-length $x' = \sin(\pi x/L)$ on the x -axis. The shape of these rescaled Renyi-bows can be fit well by a straight line. The first two points are excluded in these fits. The slope of these lines gives us $c(L)$, which is plotted in Figure 2.10 (b).

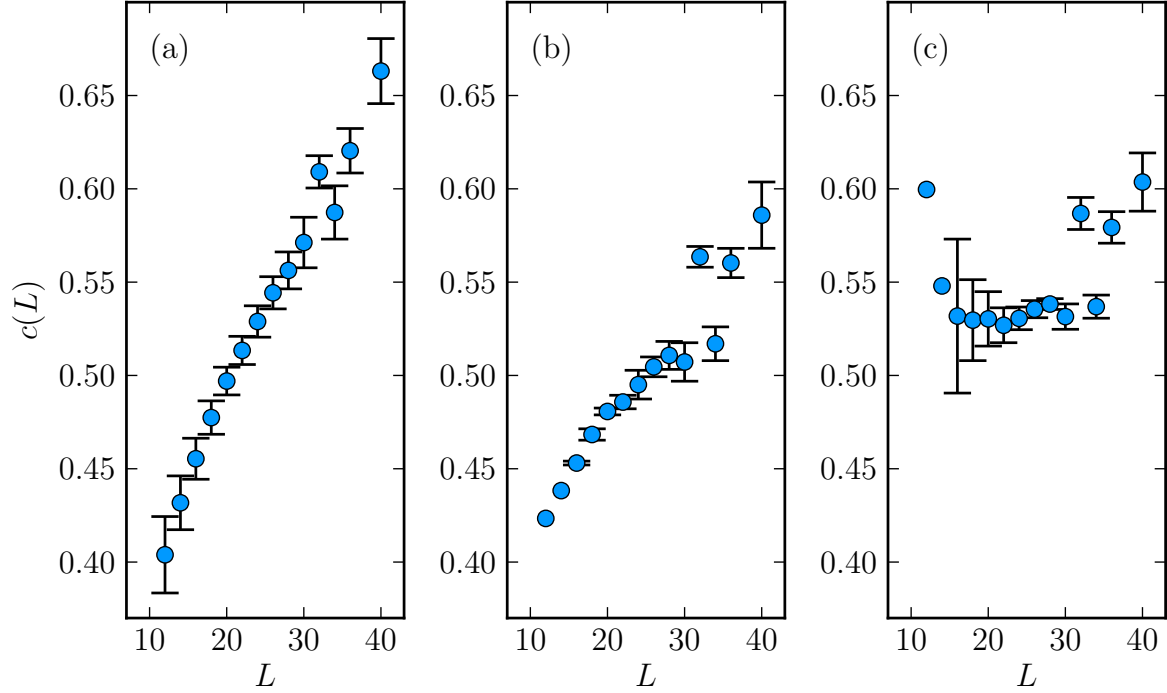


Figure 2.10: The coefficient $c(L)$ extracted from fitting the torus data in Figures 2.8 and 2.9 to $S_2 = c(L) \ln(\sin(\frac{\pi x}{L})) + d$ in three different ways:

- (a) Fitting all data points.
- (b) Excluding the first two data points on each side of the Renyi-bow.
- (c) Excluding the first two data points and fitting to $\ln(\sin(\frac{\pi x}{L-2})) + d$.

Figure 2.9 shows the same data, plotted in terms of the chord length now, where the x -axis is in units of $\ln(\sin(\pi x/L))$. The results become almost linear when plotted in this form, and are fit to the function above (Equation (2.28)), which is exactly a straight line on these axes.

Figure 2.10 shows the resulting coefficient $c(L)$ from these fits, using three slightly different techniques. The first method (Figure 2.10 (a)) uses all possible points from each system size for the fits. The second panel (Figure 2.10 (b)) excludes the first two points of Figure 2.9 of from each system size. This method leads to a significant flattening out of the coefficient $c(L)$ along with smaller errors, though the errors on the $L = 12$ and $L = 14$ systems are not calculated due to the small number of points in the fits. In the third

method, done “ad hoc”, the effective chord-lengths are changed slightly by subtracting two from L . The first two points are excluded, as with the second method, and the remaining points are fit to the function: $c(L) \ln \left[\sin \left(\frac{\pi x}{L-2} \right) \right] + d$. This method seems to give an almost constant value of $c(L) \approx 0.53$, though along with the fact that there is no physical motivation for this fitting method, the data are too noisy to draw any solid conclusions.

The second Renyi entropy at the very least displays an effective chord-length dependence over a large range of x for the $L \times L$ torus, though this apparent chord-length scaling may not be perfectly obeyed, nor is it expected to be, since unlike the 1D case where the CFT scaling prediction is valid, there is no CFT describing the entanglement scaling for the 2D Heisenberg antiferromagnet. This fact is manifest in deviations from straight-line behaviour in Figure 2.9. It is difficult to draw a firm conclusion regarding the statistical significance of any deviation from Equation (2.28) scaling in our present data, due to limited system sizes and stochastic error.

As illustrated in Figure 2.10, the coefficient probably does not approach a constant for the system sizes that we have studied, but rather has some functional dependence on L . This functional dependence may be linear or sub-linear – possibly behaving like $c(L) \sim L^p$ with $p \leq 1$. However, in order for this shape-dependent term to be universal in 2D, one expects c to approach a constant in the limit $L \rightarrow \infty$. That scenario could be supported by the QMC data if convergence were assumed to be very slow. Distinguishing between these two scenarios (and therefore the universality of this shape dependent term) is impossible on the system sizes studied, but could be done in future work.

2.5.2 Discussion

This work has shown that there is much more to the entanglement scaling of nearest-neighbour interacting systems than was previously thought.

This study confirmed that the scaling follows an area law (Figure 2.6), but with a large subleading logarithmic term (Figure 2.7). This logarithmic term, first discovered by the authors in Reference [25] is expected to be due to the presence of gapless Goldstone modes in the system. After the initial measurement, a theoretical calculation [49] found that the coefficient of this logarithm should be $(d-1)N_G/2 = 1$ for the Heisenberg model, in contrast with our value of 0.74(2). This discrepancy may be due to the finite lattice sizes used for this study. Currently members of our research group are working on a similar study of the XY model, which has only one Goldstone mode compared to Heisenberg’s two. If the XY model were to find a coefficient c of around or somewhat less than 1/2,

that would give evidence that this scaling prediction is correct and the discrepancy is due to small system sizes.

The coefficient of the logarithm due to the presence of corners in the boundary was determined for this model and compared to other values, though there is a significant lack of data to directly compare to. This corner coefficient could possibly be universal, meaning that it should give the same for models from the same universality class. The results from VB QMC and an Ising series expansion for the 2D Heisenberg model were found to be in agreement within error bars, but the spin-wave theory calculation, and the results from a free scalar field theory were not in agreement.

The aspect-ratio dependence for the Heisenberg model was studied on $L \times L$ toroidal lattices with a cylindrical region A , and compared to the 1D conformal field theory scaling. An almost-perfect logarithmic dependence of this shape-dependent term on the chord-length $\sin(\pi x/L)$ was found. It appears, however, that the coefficient of this term may have a size-dependence, rendering it non-universal. Other candidate shape functions exist in 2D that could have a universal coefficient [72].

The presence of this shape dependence means that one must take care in extracting subleading terms from the entanglement scaling. It is not sufficient to scale the boundary length within a single system size (as was the practice in Refs. [26, 29]), but instead the system must be scaled proportional to region A . If this type of aspect-ratio dependence is present in all gapless systems then researchers must take care when attempting to extract a quantity such as the topological entanglement entropy, an indicator of topological order in a system [44, 40], which so far has only been studied in gapped phases, lacking this shape dependence [33].

The fact that a complete characterization of the scaling behaviour in the Néel state remains a challenge, despite the large lattice sizes studied to date, underlines the absolute necessity for developing a range of complementary techniques for the study of entanglement entropy.

Chapter 3

Numerical Linked-Cluster Expansion

This Chapter includes results from references [38] and [39] presented anew for this thesis, along with original content not published elsewhere.

In the previous chapter we used large-scale quantum Monte Carlo (QMC) simulations to study the scaling of entanglement entropy in the 2D Heisenberg antiferromagnet. Here we develop a complementary method called the Numerical Linked-Cluster Expansion (NLCE). The NLCE is a technique which can be used to study any extensive property P of a lattice model in the thermodynamic limit (i.e. the infinite-sized lattice). It uses measurements of this “property” (energy, entropy, magnetization, etc.) from exact or nearly-exact numerical techniques on finite-sized systems. These results are then fed into a type of series expansion, which extrapolates to the thermodynamic limit by subtracting off the finite-size effects from the smaller clusters. When the model studied has a finite correlation length the NLCE will exponentially converge to the exact result per site in the thermodynamic limit \mathcal{P}/\mathcal{N} using only results from finite-sized systems. However, if the correlation length diverges, the NLCE will never reach the correct value of \mathcal{P}/\mathcal{N} , but can still approach that correct value with some expected scaling relation, allowing for extrapolation to the thermodynamic limit.

A key advantage of the NLCE method over quantum Monte Carlo (QMC) [47] and other types of series expansions [70] is that it can be used to calculate Renyi entropies for any α value including fractional values, and $\alpha \leq 1$, since one calculates the full density matrix.

Another advantage of the NLCE is that, unlike quantum Monte Carlo run with periodic boundary conditions [31] (a standard way to approach the thermodynamic limit) the NLCE

is able to analytically separate the Renyi entropies associated with linear boundaries and corners in boundaries.

This chapter begins by discussing the origins of the NLCE from series expansions in Section 3.1. Then the basics of the technique are discussed in Section 3.2. Everything to do with the choice of clusters used in linked-cluster expansions, how to find them and all their subclusters, and the best order in which to sum the series are all covered in Section 3.3. The following section (3.4) explains how to incorporate the entanglement measurement into NLCE. Then the various choices of numerical methods with which to solve clusters are discussed in Section 3.5. An example for the 1D NLCE case is worked out in Section 3.6. The convergence of the algorithm is covered in Section 3.7. Finally the entire algorithm is outlined in Section 3.8, and the results from studying the transverse-field Ising model and Heisenberg bilayer model are shown and discussed in Section 3.9.

3.1 Relation to High-Temperature Series Expansion

The derivation in this section is guided by Section 1.1 of Ref. [77], upon which I have expanded.

The Numerical Linked-Cluster Expansion (NLCE) is intimately tied to series expansion techniques, where the partition function of a system can be expanded in terms of some small parameter. In a high temperature series expansion $\beta = 1/T$ acts as this small parameter, and is used to expand out the exponential in the partition function. For the ferromagnetic Ising model the partition function is

$$\mathcal{Z} = \sum_{\{\sigma\}} e^{-\beta\mathcal{H}} = \sum_{\{\sigma\}} e^{\beta J \sum_{\langle ij \rangle} \sigma_i \sigma_j}. \quad (3.1)$$

The partition function includes a sum over the set of all possible Ising spin configurations $\{\sigma\}$ which can each be either ± 1 . Since all the Hamiltonian terms commute for this classical Ising model, we can turn the exponential of a sum into a product of exponentials,

$$\mathcal{Z} = \sum_{\{\sigma\}} \prod_{\langle ij \rangle} e^{\beta J \sigma_i \sigma_j}, \quad (3.2)$$

which can be rewritten using the Taylor expansion of the exponential, as

$$\mathcal{Z} = \sum_{\{\sigma\}} \prod_{\langle ij \rangle} \sum_{n=0}^{\infty} \frac{(\beta J)^n}{n!} (\sigma_i \sigma_j)^n. \quad (3.3)$$

When the product $|\beta J| < 1$ (corresponding to high temperatures) this sum will converge to the partition function for the ferromagnetic Ising model using a finite number of terms.

Equation (3.3) can be thought of as a sum over Hamiltonian terms acting on all the lattice links a number, $n_{i,j}$, of times for a bond between neighbouring sites i and j , where $n_{i,j}$ is an integer from 0 to ∞ . For a 4-site system this can be represented graphically as follows,

$$\mathcal{Z} = \sum_{\{\sigma\}} \sum_{n_{1,2}=0}^{\infty} \sum_{n_{2,3}=0}^{\infty} \sum_{n_{3,4}=0}^{\infty} \sum_{n_{4,1}=0}^{\infty} \frac{(\beta J)^{n_{1,2}+n_{2,3}+n_{3,4}+n_{4,1}}}{n_{1,2}!n_{2,3}!n_{3,4}!n_{4,1}!} \begin{array}{c} \text{---} n_{1,2} \text{---} \\ | \quad \quad | \\ n_{4,1} \quad \quad n_{2,3} \\ | \quad \quad | \\ \text{---} n_{3,4} \text{---} \end{array} \quad (3.4)$$

Expanding the sum out to $\mathcal{O}((\beta J)^2)$ one obtains

$$\begin{aligned} \mathcal{Z} = \sum_{\{\sigma\}} & \left[\begin{array}{c} \cdot \\ \cdot \\ \cdot \\ \cdot \end{array} + \beta J \left(\begin{array}{c} \text{---} \\ \cdot \\ \cdot \\ \cdot \end{array} + \begin{array}{c} \cdot \\ \text{---} \\ \cdot \\ \cdot \end{array} + \begin{array}{c} \cdot \\ \cdot \\ \text{---} \\ \cdot \end{array} + \begin{array}{c} \cdot \\ \cdot \\ \cdot \\ \text{---} \end{array} \right) \\ & + (\beta J)^2 \left(\begin{array}{c} \text{---} \\ \cdot \\ \cdot \\ \cdot \end{array} + \begin{array}{c} \cdot \\ \text{---} \\ \cdot \\ \cdot \end{array} + \begin{array}{c} \cdot \\ \cdot \\ \text{---} \\ \cdot \end{array} + \begin{array}{c} \cdot \\ \cdot \\ \cdot \\ \text{---} \end{array} + \begin{array}{c} \text{---} \\ \cdot \\ \cdot \\ \cdot \end{array} + \begin{array}{c} \cdot \\ \text{---} \\ \cdot \\ \cdot \end{array} + \begin{array}{c} \cdot \\ \cdot \\ \text{---} \\ \cdot \end{array} + \begin{array}{c} \cdot \\ \cdot \\ \cdot \\ \text{---} \end{array} \right) \\ & + \frac{(\beta J)^2}{2} \left(\begin{array}{c} \text{---} \\ \cdot \\ \cdot \\ \cdot \end{array} + \begin{array}{c} \cdot \\ \text{---} \\ \cdot \\ \cdot \end{array} + \begin{array}{c} \cdot \\ \cdot \\ \text{---} \\ \cdot \end{array} + \begin{array}{c} \cdot \\ \cdot \\ \cdot \\ \text{---} \end{array} \right) + \dots \end{array} \quad (3.5)$$

where a link between two sites j and k represents the Hamiltonian interaction $\sigma_j \sigma_k$.

The above derivation shows that the partition function can be expressed as a series of graphs with all possible numbers of interactions between neighbouring sites (assuming only nearest-neighbour interactions). From this one can see that it is possible to express the partition function using a separate sum for each ‘‘graph’’ or cluster of sites that can be embedded in the full system. Then one can sum up each of these contributions to get an equivalent expression for the partition function,

$$\mathcal{Z} = \sum_{\{\sigma\}} \sum_c \prod_{\langle ij \rangle \in c} \sum_{n_{i,j}=1}^{\infty} \frac{(\beta J)^{n_{i,j}}}{n_{i,j}!} (\sigma_i \sigma_j)^{n_{i,j}}. \quad (3.6)$$

The above can be directly compared with (3.3). Because the $n_{i,j}$ ’s no longer start from 0, the sum can no longer be written in the form of (3.1),

$$\mathcal{Z} = \sum_{\{\sigma\}} e^{-\beta \mathcal{H}} \neq \sum_{\{\sigma\}} \sum_c e^{-\beta \mathcal{H}_c}. \quad (3.7)$$

The right hand side of (3.7) results in overcounting many of the contributions to the partition function, since the contributions from each cluster c contain all contributions (diagrams) from every subcluster of sites s contained in cluster c .

Similar derivations to decompose sums over bond interactions into sums over different clusters of sites in a system can be shown for other types of series expansions. This discovery led to the predecessor of NLCEs, linked-cluster expansions (LCEs), where series expansions are used to solve for a property on each cluster and then the series expansion results are put into the linked-cluster expansion to obtain results in the thermodynamic limit.

The difference between LCEs and NLCEs is the use of numerical technique to exactly solve for the properties of the clusters in NLCE. (When first developed it was called the “exact linked-cluster expansion technique” [32].) This has the advantage that the cluster expansion does not inherit the limited radius of convergence of a series expansion, but instead is only limited by cluster size. In LCEs the series convergence is limited both by the smallness of a parameter (which gives a radius of convergence) *and* the cluster sizes used.

3.2 Linked-Cluster Expansions

An extensive property can be expressed as a sum over contributions from all possible connected clusters of sites c that can be embedded in the lattice \mathcal{L} [57, 55, 56, 77]. The property of interest (per site) in the thermodynamic limit for the given lattice model is expressed as a sum of the “weights” of all possible embeddable clusters,

$$\mathcal{P}/\mathcal{N} = \sum L(c)W_P(c) \quad (3.8)$$

where $L(c)$ is the lattice constant—the number of possible distinct embeddings of cluster c in the lattice \mathcal{L} —and $W_P(c)$ is the weight of cluster c for the property P .

The weight is defined recursively according to the inclusion-exclusion principle (see Section 3.3.1) as,

$$W_P(c) = P(c) - \sum_{s \in c} M(s)W_P(s) \quad (3.9)$$

where $P(c)$ is the property of interest measured for the finite cluster c . The sum is over all subclusters s of cluster c , that is, a cluster s which can be embedded in c . $M(s)$ is the multiplicity of subcluster s , indicating the number of possible ways that s can be embedded in c . $W_P(s)$ is the weight of the subcluster s . Clusters and embeddings will be discussed in detail in Section 3.3.

To calculate all the weights one must begin from the smallest cluster c_0 which has no subclusters. Then $W_P(c_0) = P(c_0)$ can be used to calculate the weight for the next largest

Clusters				Subcluster Multiplicity, $M(s)$								
id	$n_x \times n_y$	N	$L(c)$	(a)	(b)	(c)	(d)	(e)	(f)	(g)	(h)	(i)
(a)	1×1	1	1									
(b)	1×2	2	2	2								
(c)	1×3	3	2	3								
(d)	1×4	4	2	4	3	2						
(e)	2×2	4	1	4	4							
(f)	2×3	6	2	6	7	2		2				
(g)	2×4	8	2	8	10	4	2	3	2			
(h)	3×3	9	1	9	12	6		4	4			
(i)	3×4	12	2	12	17	10	3	6	7	2	2	
(j)	4×4	16	1	16	24	16	8	9	12	6	4	4

Table 3.1: The properties of all clusters up to a maximum n_x and n_y of four sites, including: an identifier, dimensions, number of sites N , lattice constant $L(c)$, and the multiplicity of their subclusters $M(s)$ (this is left blank for $M(s) = 0$).

cluster which contains only c_0 as a subcluster. Each weight represents the contribution to the property for a given cluster that cannot be expressed as a sum of contributions from smaller clusters, i.e. the unique contribution from that cluster.

Equations (3.8) and (3.9) completely define the NLCE technique. The series will converge when the clusters becomes large enough to encompass the system's correlation length. In the case of properties in critical systems, which do not fully converge for finite cluster sizes, an additional step of finite-size scaling the results as a function of cluster size must be performed.

3.3 Clusters

In this thesis a cluster of sites c is a set of sites connected by the given Hamiltonian interactions. If the Hamiltonian of the model contains only nearest-neighbour interactions of the same sign and strength for every bond then the connections in the clusters are identical to the connections in the underlying lattice. Figure 3.1 shows examples of four different clusters on a square lattice with nearest-neighbour interactions. Table 3.1 shows the properties of some rectangular, square-lattice clusters.

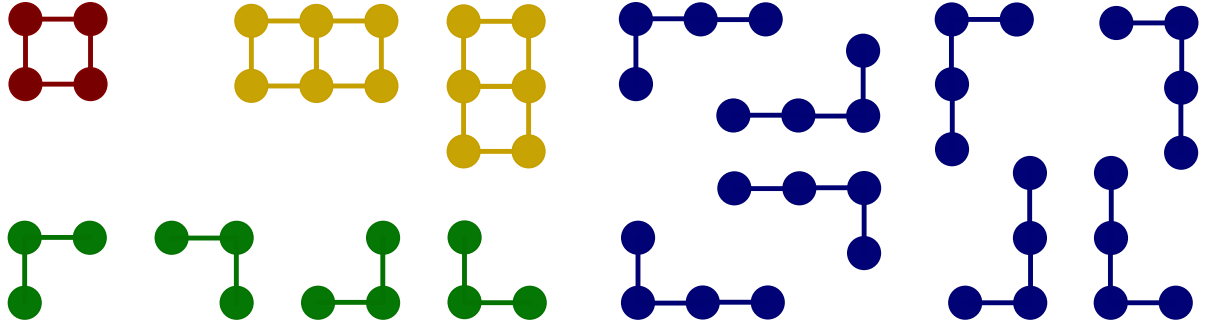


Figure 3.1: An illustration of four different clusters with different lattice constants for a square lattice. The red square has $L(c) = 1$ because it can only be embedded in the underlying lattice in one way. The yellow rectangle can be embedded in two different ways, related by a 90° rotation. The green cluster can be embedded in four ways, since rotations of 90° , 180° and 270° all give different embeddings. The blue L-shaped cluster has no symmetries on the square lattice. Rotations of any angle allowed by the lattice, and additionally reflections, give distinct embeddings leading to $L(c) = 8$.

3.3.1 Inclusion-Exclusion

The NLCE equations (3.8) and (3.9) can be thought of as a statement of the Inclusion-Exclusion Principle—a way of avoiding double counting. The principle states that the number of elements in the union of two finite sets $|A \cup B|$ is simply $|A| + |B| - |A \cap B|$. This gives intuition for why disconnected clusters need not be considered in NLCE calculations. They can be completely described by their unconnected components, $|A \cup B| = |A| + |B|$ where, as far as cluster weights go, A and B would be considered subclusters of $A \cup B$ already and thus subtracted off in equation (3.9). Their weight $W(c)$ is always zero, just as the number of elements in the intersection of disjoint sets is zero.

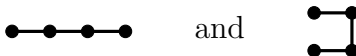
3.3.2 The Lattice Constant

The lattice constant $L(c)$ is the number of distinct ways a cluster c can be embedded in the lattice. A rotation or reflection could result in a possible embedding depending on the symmetry of c and the lattice. A simple translation will not lead to a different embedding in the infinite lattice \mathcal{L} .

In the case of transformations involving only rotations and reflections, on a square lattice the only possible values for $L(c)$ are 1, 2, 4 and 8. See Figure 3.1 for examples of

these four possibilities. A cluster with $L(c) = 8$ has no symmetries on the square lattice. The point group symmetries include successive 90° rotations, and reflections across the cluster's x - and y - axes, which can yield distinct embeddings. On the other hand, square clusters (including the 1 site cluster) will have $L(c) = 1$ because they are invariant under any of the previously mentioned operations.

We may also consider any clusters that are *topologically* equivalent to contribute to the lattice constant. For example,



are topologically equivalent for many standard properties such as energy, entropy, or magnetization, to name a few. For a group of clusters that give the same value of $P(c)$, it is only necessary to measure one of these clusters, and the other(s) can be accounted for by increasing the lattice constant.

It is important that measurements considered on a cluster obey the same symmetry, i.e. if $L(c) = 2$ then a measurement must give the same results for both orientations of the cluster, otherwise the two orientations should be considered separately with $L(c) = 1$ for each. Standard measurements, such as energy, would not normally depend on the orientation of the cluster. However we will see in Section 3.4 that this becomes important for simplifying the measurement of entanglement, which depends on spatial boundaries defined on the lattice.

3.3.3 General Clusters

Cluster expansions are usually done considering all possible clusters up to some maximum size. There are different ways of defining clusters. In a site-based definition any two sites which would normally have an Hamiltonian interaction between them will have a bond between those sites (representing the interaction). In the bond-based definition there does not necessarily need to be an interaction between all sites that would normally interact. For example the U-shaped cluster in the above section would be bond-based.

The extent of the clusters used in NLCE calculations is limited by two factors:

1. Generating a large list of clusters and their respective subclusters,
2. Solving for the property on large clusters, or a large number of clusters.

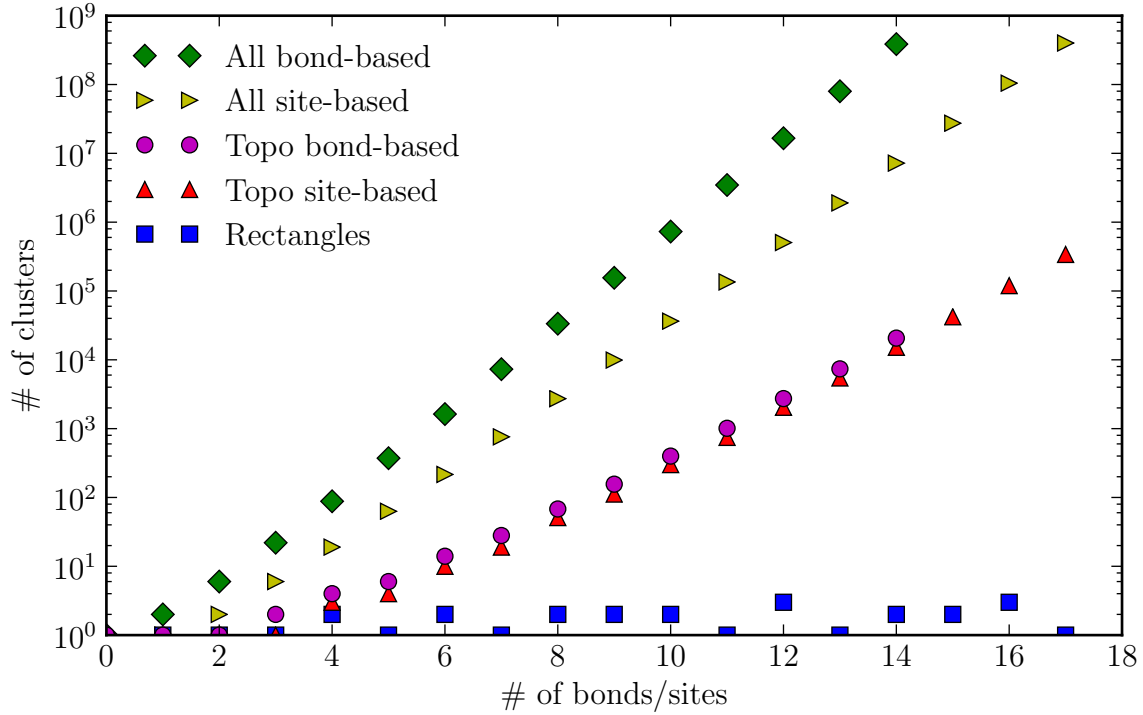


Figure 3.2: The number of distinct clusters on a square lattice with nearest-neighbour interactions as a function of the number of bonds or sites in the cluster. The plot shows the $\sum L(c)$ for bond-based and site-based clusters, as well as the number of topologically distinct clusters for each classification method. The number of clusters scales exponentially with the number of base units in the cluster. Numbers are taken from Refs. [55] and [77]. The blue squares at the bottom of the plot are the number of rectangular clusters for a given number of sites, the values of which range from 1 to 3 for up to 17 sites.

Generating all possible clusters and finding their subclusters is exponentially complex in the number of sites considered, since the number of clusters scales exponentially with the number of sites or bonds (see Figure 3.2). On a square lattice with only nearest-neighbour interactions, considering just clusters with 16 sites will yield 104,592,937 clusters, 119,561 of which are topologically distinct. There 386,458,826 clusters with 14 bonds (which could correspond to anywhere from 10 to 15 sites on a square lattice) of which 20,665 are topologically distinct. Figure 3.2 shows the number of site-based and bond-based clusters per bond or site, and the respective number of topologically distinct clusters. The process to find all distinct clusters and each possible subcluster can prove laborious, even for a computer. Following Ref. [77], the procedure to find all clusters and subclusters accounting for symmetrically or topologically equivalent clusters is briefly summarized below.

1. Generate a list of all symmetrically distinct clusters with n_c sites or bonds
 - (a) Start with all clusters of $n_c - 1$ sites or bonds and add 1 site or bond at the edge of the cluster in every possible position.
 - (b) Check that each new cluster is not already in the list. If not then add it.
2. Keep only clusters unrelated by point group symmetries. (Modify $L(c)$'s.)
 - (a) Apply each point group symmetry to every cluster generated in Step 1.
 - (b) Check if any of these 8 clusters (for a square lattice) is in the list from Step 2.
 - i. If so, increase $L(c)$ for that cluster.
 - ii. If not, add that cluster to the list.
3. Keep only topologically distinct clusters. (Modify $L(c)$'s again.)
 - (a) Generate the $(n_c)!$ possible adjacency matrices for a cluster of n_c sites.
 - (b) Check if any of these matrices already occur in the list of topologically distinct clusters.
 - i. If so, increase $L(c)$ for that cluster.
 - ii. If not, add that cluster to the list.
4. Find all subclusters.
 - (a) For each cluster from Step 3, for $n_s = \{1, 2, \dots, n_c - 1\}$ place n_s sites inside the cluster c in the $\binom{n_c}{n_s}$ possible ways.

- (b) Check if all sites are connected (ignore unconnected clusters).
 - (c) Add that cluster to the list of subclusters for c .
 - (d) Follow Steps 2 and 3 with the following modifications: $M(s)$ replaces $L(c)$, and translation within the cluster c is now a valid symmetry operation in Step 2.
5. Use the generated list of clusters, lattice constants, and subclusters to perform the NLCE.

It should be noted that, though time consuming, the process in Steps 1 - 4 need only be completed once before the NLCE can be done on any system possessing the same lattice and Hamiltonian symmetries.

The problem of checking if a certain cluster is equivalent to one already included in a list of clusters is related to the Graph Isomorphism Problem (GIP). It is not known whether the GIP is solvable in polynomial time in general, however for the special case of planar graphs (a class into which all 2D nearest-neighbour interacting lattice systems fall into) the solution *is* known to scale polynomially [14]. Checking the equivalence of two clusters is just part of each of the 4 steps, though. Each step also involves searching through a list of clusters, the number of which increases exponentially with the number of sites or bonds included, as displayed in Figure 3.2.

The purpose of finding clusters that are symmetrically related is to minimize the number of measurements of $P(c)$ on different clusters. It is not necessary to find lattice constants—one could instead study *all* clusters separately and assign them each $L(c) = 1$. Finding these cluster symmetries almost always improves the efficiency of the algorithm and allows one to go to larger cluster sizes. If it is the case that it is more efficient to measure $P(c)$ on 3×10^8 clusters than to find all topologically equivalent clusters and do 2×10^4 measurements, then Steps 1 - 4 should certainly be left out.

NLCE calculations are generally limited to around 16 sites for a square lattice system due to the problem of finding all possible clusters and subcluster. By contrast, the Lanczos algorithm can solve for the exact groundstate wavefunction of a system of up to 40 sites, or more depending on the system [43]. Thus, the useable numerical data for NLCE calculations is severely limited by the poor scaling of the cluster and subcluster finding algorithm.

One method of avoiding the arduous task of finding all topologically distinct clusters is to limit the type of clusters considered. It is possible to change the “base unit” of a cluster so that instead of one site or bond it is a plaquette of four sites and four bonds [55]. This significantly increases the sizes of clusters that can be considered, at the cost of

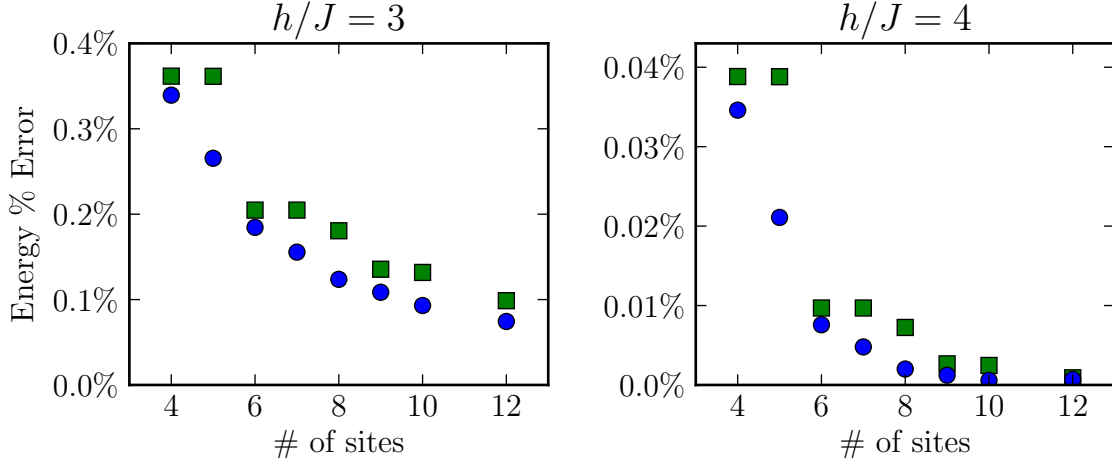


Figure 3.3: The percent error in the groundstate energy per site for the transverse-field Ising model from the NLCE using all clusters with up to 12 sites (blue circles) and just rectangular clusters up to 12 sites (green squares). The exact values for the energy in the thermodynamic limit were taken from quantum Monte Carlo results [30, 39]. The critical point for the quantum phase transition in this system is at $h/J = 3.044$ [54], so the left plot is very close to the critical point, while the plot on the right is relatively far away from the critical point.

excluding many clusters. If, however, the plaquette base unit is still able to capture all of the important physics of the problem then this change is an appropriate solution to push the technique to larger cluster sizes.

It is also possible to limit the geometries of the clusters in a different way. In this thesis the NLCE procedure is done using only $n_x \times n_y$ rectangular clusters (including 1D clusters). For clusters of up to 12 sites, the site-based and rectangular clusters are compared in Figure 3.3.

3.3.4 Rectangular Clusters

Limiting the NLCE calculation to only use rectangular clusters *greatly* simplifies the calculation, moving the computational bottleneck from the cluster and subcluster generation to the measurement of $P(c)$. Steps 1 - 4 above become almost completely trivial, and the number of different clusters for a given number of sites n_c is equivalent to the number of

pairs of factors one can find for n_c . The number of rectangles scales close to constant with the number sites (see the blue squares in Figure 3.2), with only 27 rectangular clusters *total* for $n_c = \{1, 2, \dots, 16\}$ as opposed to the $\sim 10^8$ unrestricted clusters. Finding the lattice constant becomes a simple check. Considering $n_x \times n_y$ rectangular clusters on a square lattice, $L(c)$ can only take two possible values: $L(c) = 1$ if $n_x = n_y$ or $L(c) = 2$ if $n_x \neq n_y$. A list of rectangular clusters up to a maximum width and height of 4 sites is shown in Table 3.1 along with $L(c)$ for each cluster and $M(s)$ for the subclusters of each cluster.

Using rectangular clusters, the calculation becomes entirely limited by the size of cluster on which $P(c)$ can be measured [39]. With exact diagonalization this could be somewhere around 16 sites, but if Lanczos is used instead to study the groundstate properties of the system then 40 site systems on a square lattice are possible [43]. Density matrix renormalization group calculations are mainly limited by the y -dimension of the cluster, not necessarily the total number of sites [75], so long skinny clusters oriented in the y -direction become the most challenging clusters to solve. Depending on the type of system it is not unprecedented to have widths of up to 12 or 14 sites in the y -direction, so it is possible for clusters of 100s of sites to be used. Monte Carlo also shows promise as a method of reaching larger cluster sizes, but as of yet it is still untested as an NLCE cluster solver.

One might think that reducing the number of clusters in the calculation so drastically would cause important information to be discarded, possibly affecting the results of the expansion. Figure 3.3 addresses this concern, by comparing results from the two methods. The figure shows the percent error in the NLCE value for the groundstate energy of the TFIM using all clusters up to 12 sites and using only rectangular clusters of up to 12 sites. Near the critical point at $h/J = 3$ the correlations are long range (the correlation length $\xi \rightarrow \infty$ at the QCP) and neither group of clusters converges to the exact groundstate energy (found via quantum Monte Carlo [30, 39]) by 12 sites. It can be seen that the subset of rectangular clusters has larger error, but the difference is within 0.03% at 12 sites. Away from the critical point, at $h/J = 4$ where the correlation length becomes shorter, both groups of clusters have captured the groundstate energy to within 0.001% at 12 sites.

Both plots also show a step-like pattern in the rectangular clusters as a function of the number of sites, while for general clusters the curve is smooth. This is a result of the small number of clusters included in the expansion when we are restricted to rectangles. For the prime numbers of sites (where one sees this step) there is only one new cluster being considered and it is always a 1D cluster. One dimensional clusters will generally not contribute much to the expansion and therefore they will not significantly affect the results. Square clusters and clusters for which n_x (the number of sites in the x -direction)

Clusters			Order			Length-scale		
id	$n_x \times n_y$	$L(c)$	\mathcal{O}_G	\mathcal{O}_A	\mathcal{O}_Q	ℓ_G	ℓ_A	ℓ_Q
(a)	1×1	1	1	2	2	1	1	1
(b)	1×2	2	2	3	5	1.414	1.5	1.581
(c)	1×3	2	3	4	10	1.732	2	2.236
(d)	1×4	2	4	5	17	2	2.5	2.915
(e)	2×2	1	4	4	8	2	2	2
(f)	2×3	2	6	5	13	2.445	2.5	2.550
(g)	2×4	2	8	6	20	2.828	3	3.162
(h)	3×3	1	9	6	18	3	3	3
(i)	3×4	2	12	7	25	3.464	3.5	3.536
(j)	4×4	1	16	8	32	4	4	4

Table 3.2: The orders and associated length-scales for clusters of up to $n_x, n_y = 4$.

is close in magnitude to n_y will tend to give the largest contributions in most types of systems, as can be seen in Figure 3.3 by focusing on the points for 4, 6, 9 and 12 sites.

It seems clear that the benefit of restricting ourselves to rectangular clusters outweighs any possible loss of information caused thereby. And the restriction allows for much larger cluster sizes to be reached. On the square lattice one is restricted to around 16 sites when attempting to consider general clusters, whereas with rectangular clusters up to 26-site [38] and 40-site clusters [39] have been studied, and even 100-site clusters could be within reach [74].

3.3.5 Definition of Order

In an NLCE calculation, it is sometimes necessary to define an *order*, a way of grouping together clusters of similar sizes. Originating as an analogue to the “order” of a series expansion calculation, this quantity tells us the proper sequence in which to add clusters to the NLCE sum in Equation (3.8). In 1D it is obvious that clusters with less sites would be added to the sum first, but in 2D one does not necessarily know whether a 4×5 cluster comes before or after a 3×7 cluster.

The order also allows one to assign a length-scale ℓ related to the largest order included in a calculation. At a quantum critical point for example, this allows for the study of NLCE data as a function of length-scale, giving scaling relationships that can be extrapolated towards the thermodynamic limit.

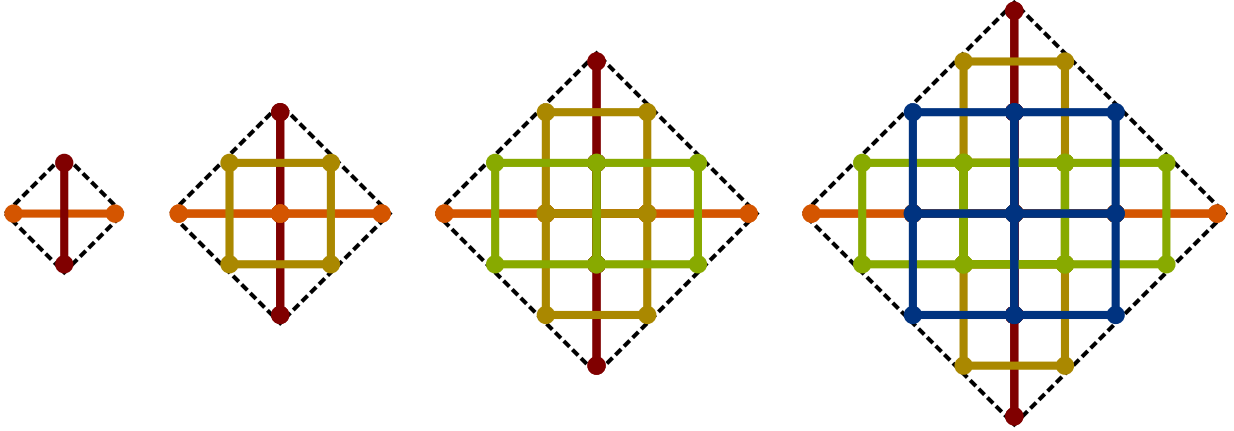


Figure 3.4: Clusters of the same order \mathcal{O}_A graze the sides of diamonds. Note that the representation of clusters here differs from Figs 3.5 – 3.7, where a “site” is defined as a 1×1 unit square. Here sites are zero dimensional points separated by 1 unit length bonds. The decision of which definition to use is not all that important as long as one is consistent.

There are many possible ways of defining an order for a given cluster c . The two definitions that have been implemented in NLCE calculations so far [38, 39], the arithmetic \mathcal{O}_A and geometric \mathcal{O}_G orders, are defined below. For a rectangular cluster of size $n_x \times n_y$,

$$\mathcal{O}_A = n_x + n_y \quad \Rightarrow \quad \ell_A = \frac{1}{2}(n_x + n_y) = \frac{1}{2}\mathcal{O}_A \quad (3.10)$$

$$\mathcal{O}_G = n_x n_y \quad \Rightarrow \quad \ell_G = (n_x n_y)^{\frac{1}{2}} = \sqrt{\mathcal{O}_G} . \quad (3.11)$$

The first definition \mathcal{O}_A (3.10) is equal to the sum of the number of sites in the x - and y -directions for each cluster. It can also be seen as selecting out clusters that will graze the edges of a diamond of with a width and height of $n_x + n_y - 2$ lattice spacings (and edge-length of $(n_x + n_y - 2)/\sqrt{2}$). See Figure 3.4 for an example of cluster groupings for \mathcal{O}_A . Note that if we choose to represent the clusters such that sites are 1×1 squares with no space between them (a convention that will be used for the remainder of this chapter), then \mathcal{O}_A is instead defined as a group of clusters that graze the edges of a diamond with width and height \mathcal{O}_A , not $\mathcal{O}_A - 2$. The associated length-scale for the arithmetic order is half the sum of the edge lengths, or the average of the two edge lengths.

From Equation (3.11), for geometric orders \mathcal{O}_G , clusters are grouped together based on the number of sites they contain, since the number of sites in a cluster $N_c = n_x n_y$ for a rectangular cluster. Then the associated length-scale for a given geometric order is equal to the square-root of the number of sites $\ell_G = \sqrt{n_x n_y}$. Analogous to the diamond definition

for \mathcal{O}_A , the clusters that make up an order of \mathcal{O}_G will all fit inside a set of hyperbolic curves, as shown in Figure 3.5 (a).

The different types of orders are related to their corresponding length-scales through averages. For \mathcal{O}_A the length-scale ℓ_A is defined as the *Arithmetic* mean of n_x and n_y , while for \mathcal{O}_G the length-scale is equal to the *Geometric* mean of n_x and n_y . Following this convention it is also possible to define a length-scale in terms of the *Quadratic* mean,

$$\mathcal{O}_Q = n_x^2 + n_y^2 \Rightarrow \ell_Q = \sqrt{\frac{1}{2}(n_x^2 + n_y^2)}. \quad (3.12)$$

This corresponds to clusters that will fit inside a circle of diameter $\sqrt{2} \cdot \ell_Q$. Table 3.2 gives the values of the different orders and length-scales for rectangular clusters up to $n_x = n_y = 4$. As expected, all three definitions give the same length-scales for square clusters where they are simply averages of two equal numbers ($n_x = n_y$). It is the non-square clusters for which the values will differ.

In one dimension it is not necessary to choose a definition of order as it is obviously characterized entirely by the number of sites in a chain. In two dimensions it is intuitive to continue to use the total number of sites in each cluster N_c as a definition of order (\mathcal{O}_G). This intuition is reinforced by the fact that the method used to solve clusters, Lanczos, is restricted to a maximum number of sites, thus limiting the NLCE to a maximum \mathcal{O}_G . Upon further investigation we found that the expected scaling of quantities such as energy and the line entanglement (below) scale as one would normally expect if we use the assumption that the length-scale $\ell = \sqrt{N_c}$ (see Figure 3.16 for example). It is only when one looks at the clusters included for a given geometric order (which include relatively long 1D clusters along with much smaller square and rectangular clusters) that it seems there may be a better method for defining a length-scale.

The arithmetic order \mathcal{O}_A was conceived with the intention of creating a better definition of length-scale, and was used in our most recent NLCE calculations [39]. The idea behind the quadratic order is that it is the most natural definition of length-scale, since all of the possible correlations considered by an NLCE calculation with a given \mathcal{O}_Q will fit inside a certain radius. So far this idea has not yet been tested, and it has the drawback that it focuses on the most difficult clusters to solve, the large square clusters with the largest number of sites. For a given value of ℓ the quadratic definition of order will actually throw out additional clusters that the arithmetic order would include. Similarly the arithmetic order will include less clusters than the geometric order will. Basically, the arithmetic and quadratic orders will throw out extra clusters that are computationally “free”, or at least much easier to calculate than the larger, less one dimensional clusters, with the intention of defining a more accurate length-scale for a given NLCE calculation. The longer 1D

clusters included in \mathcal{O}_G do not end up with a large weight in the NLCE calculations, so including them may not significantly change the results, as was seen in [39], and Figures 3.16 - 3.20.

Figures 3.5 - 3.7 show different ways to visualize the three cluster orders: \mathcal{O}_G , \mathcal{O}_A , and \mathcal{O}_Q . Figures 3.5 (a) - (c) show the bounding envelopes for orders with integer ℓ (the black lines) plotted along with shaded clusters where each 1×1 block represents one site. Clusters are shaded corresponding to the smallest integer ℓ that they are less than or equal to (i.e. the clusters with non-integer ℓ have been rounded up to the next integer), while the square clusters are always exactly equal to an integer ℓ (see Table 3.2). Figure 3.5 (d) shows the envelopes corresponding to the different types of orders plotted together for $\ell = 1$ to 24.

Figure 3.6 represents the envelopes of Figure 3.5 in a different way. The clusters are now centred at the origin instead of having their bottom left corner on the origin, and only the $\ell = 5$ envelopes are shown for each type of cluster ordering. The figures in 3.7 are similar those in 3.6 but they only show a zoomed in view, excluding the long 25-site 1D clusters that would be included for the geometric order. These figures serve to emphasize how skewed the geometric definition of order is while still being associated with the same length-scale as the other two definitions. Clearly the quadratic order would give the most physical definition for a length-scale, but it has the drawback that it emphasizes clusters for which almost any numerical technique will have the most trouble solving. Since the NLCE places a small weight on clusters that do not contribute much to the system in the thermodynamic limit, including these low weight clusters in a given order will not significantly skew the results. Therefore it is likely that there will not be much difference in the results between these three different definitions.

3.4 Measuring Entanglement

Entanglement requires a type of a special measurement in the NLCE, because it is a spatially dependent quantity. As discussed in Section 1.1, measuring entanglement requires the division of the system into two regions, A and B . The entanglement between these regions is quantified using the Renyi entanglement entropies,

$$S_\alpha = \frac{1}{1-\alpha} \ln \text{Tr}(\rho_A^\alpha). \quad (3.13)$$

Typically in the NLCE procedure, which is used to study systems in the thermodynamic limit, the boundary between the regions is defined as an infinite line, separating the infinite

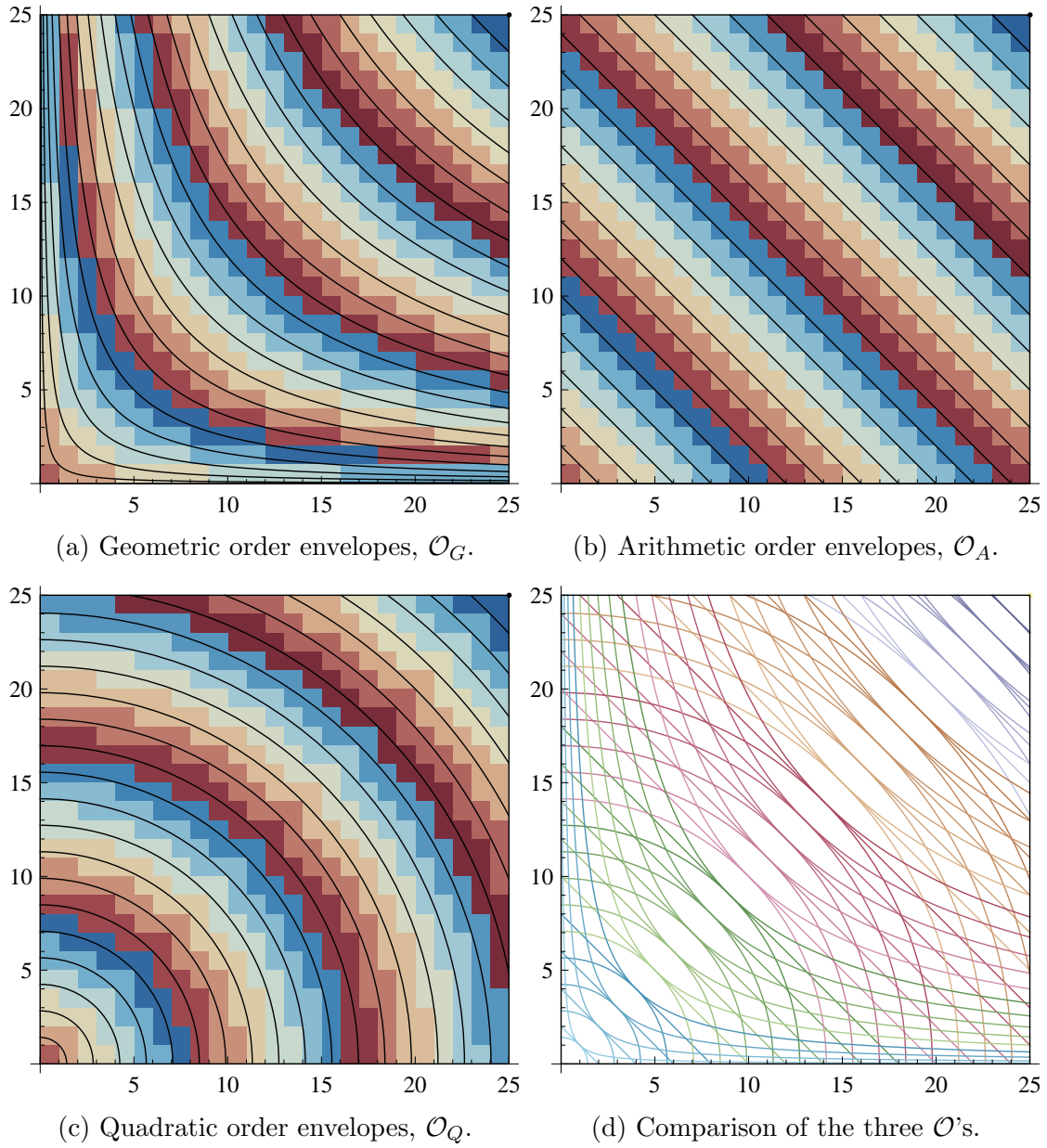
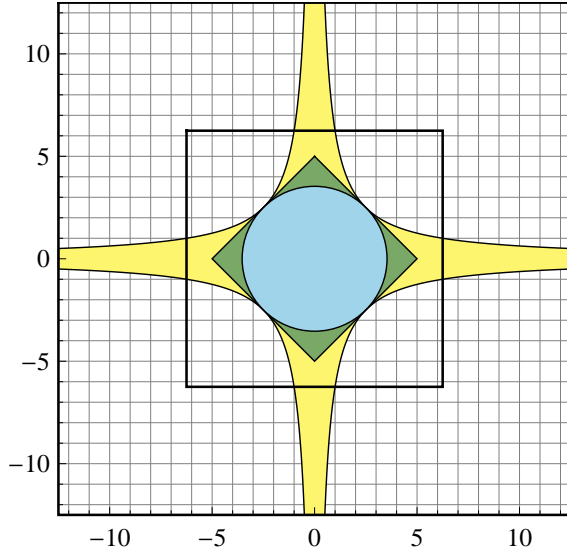
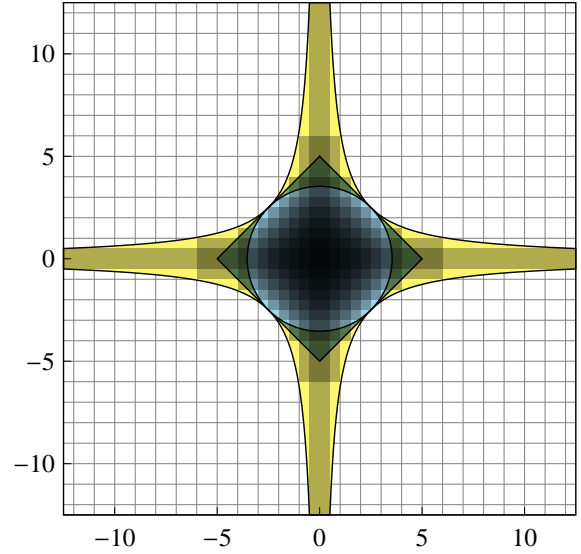


Figure 3.5: The different methods of classifying clusters by order \mathcal{O} . Lines indicate integer length scales and shaded boxes represent clusters. The colours correspond to the smallest integer length-scale that a cluster is not larger than.



(a) The three envelopes for $\ell = 5$. The inner square is the cutoff for ℓ_G when 1D clusters are not included, and the outer square is the cutoff including 1D clusters.



(b) The shaded boxes represent the largest clusters with $\mathcal{O}_G \leq 25$, $\ell_G \leq 5$.

Figure 3.6: These three coloured regions show the areas inside which clusters less than or equal to a given order would fit, using the three definitions of order discussed: \mathcal{O}_A (green square), \mathcal{O}_G (yellow shape bounded by hyperbolic curves), and \mathcal{O}_Q (teal circle). The x - and y -axes represent the number of sites in the width (n_x) and height (n_y) of a given cluster. These envelopes assume that the width of one site is one unit and there is no distance between sites. The outer bounding box is the cut-off for all possible clusters of \mathcal{O}_G , and the inner box is the cut-off if no 1D clusters are included.

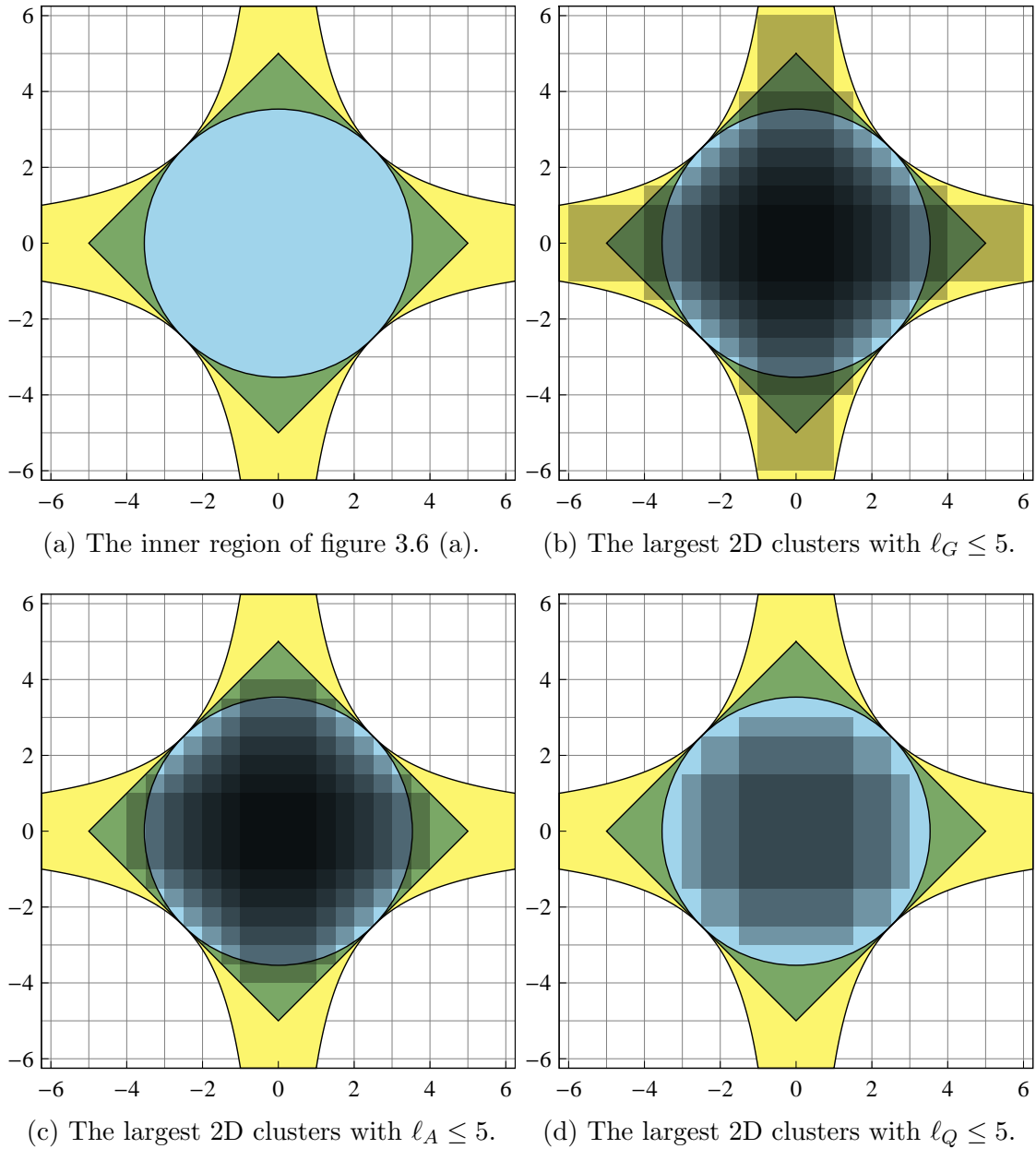


Figure 3.7: These figures show a zoomed in version of Figure 3.6 with the shaded regions indicating the largest possible clusters with $\ell \leq 5$ excluding 1D clusters, for each of the different types of orders.

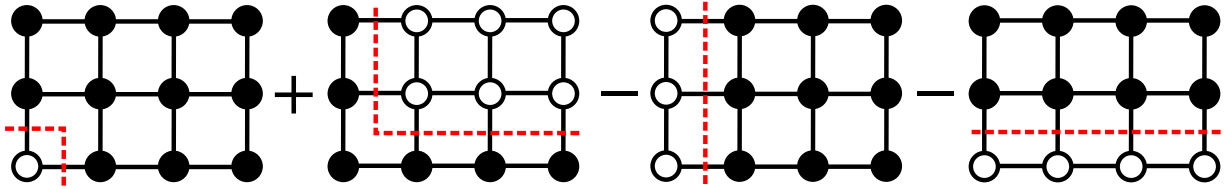


Figure 3.8: Entanglement cuts to measure the corner term for the first plaquette of this 12-site cluster. For the full contribution from this 4×3 cluster, a similar series of 4 entanglement measurements would be done for each of the 6 plaquettes in the cluster. The corresponding mathematical representation is shown in Equation (3.15).

plane into two infinite half-planes. While it is possible to define a closed boundary inside of which is the entirety of region A , the results would only begin to differ from that of an infinite boundary once the size of the clusters considered approach the size of region A , so they could “see” both sides of the region. Studying an infinite line, the results become meaningful at much smaller cluster sizes.

In this chapter I will discuss two types of boundaries:

- an infinite straight line \longleftrightarrow running in the x or y direction,
- an infinite line with a 90° corner $\begin{array}{l} \longleftarrow \\ \downarrow \end{array}$ containing either the first or third quadrant.

These geometries can be combined to analytically separate the Renyi entropies associated with lines and corners. When the subsystem A is a half-plane, one obtains only the entropy associated with the line. When the subsystem A is a quadrant, it contains both line and corner contributions. A suitable choice of subdivision of the system into half-planes and corners is sufficient to isolate the corner contribution from every graph. The combination of boundaries needed to isolate the corner contribution is shown in Figure 3.8. This allows for a more accurate determination of each term than is possible in QMC, where e.g. the dominant “area law” can easily overwhelm subleading terms such as corner contributions. For more information on the corner term see Sections 1.3.2 and 2.5.1.

In general, entanglement measurements in the NLCE are done by considering every distinct way that the chosen boundary can intersect a cluster. This is because the boundary breaks the translational invariance of the infinite system, and each different intersection

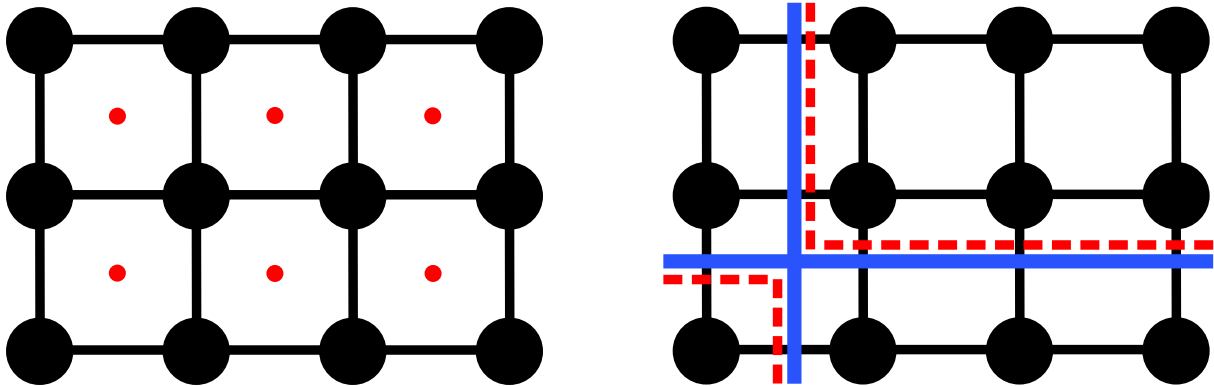


Figure 3.9: **(Left)** The red dots denote the centres of each of the six plaquettes in this 4×3 cluster. A contribution to the corner entanglement must be measured using each of them. **(Right)** Another way of depicting the entanglement cuts from Figure 3.8. The red dashed lines represent opposing 90° corner cuts which are added to the contribution $V_{1,1}^1$ and $V_{3,2}^2$, while the solid blue intersecting lines are the two perpendicular line contributions L_1^y and L_1^x which are subtracted off.

must be taken into account. It also it serves to make the entanglement an extensive quantity as required by the NLCE, since there are $(n_x - 1) \times (n_y - 1)$ entanglement measurements for an $n_x \times n_y$ cluster.

Line Entanglement

To measure the entanglement across a line running in the y -direction, L^y , for a given cluster we use

$$P(c) = \sum_{i=1}^{n_x-1} S_\alpha(L_i^y), \quad (3.14)$$

where c is an $n_x \times n_y$ cluster and L_i^y denotes a region A including i columns of the cluster. This measurement can be simplified for most rectangular clusters. Since $S_\alpha(A) = S_\alpha(B)$ for a pure groundstate wavefunction, we have $S_\alpha(L_i^y) = S_\alpha(L_{n_x-i}^y)$ which can approximately halve the number of measurements required. Analogously, the 90° corner boundary will have its own symmetries that can be exploited to reduce the total number of measurements required.

As mentioned in Section 3.3.2, if a cluster has lattice constant $L(c) > 1$, any measurements on that cluster must share the same symmetry, or else $L(c)$ must be modified for that

cluster. This becomes especially important to consider for entanglement measurements, where a cluster is divided into two spatial regions. In the example above (Equation (3.14)), of the entanglement across a vertical line, the two orientations of a non-square cluster will give different results. This problem can be remedied by instead calculating the sum of the entanglement due to a vertical line and that due to a horizontal line. A second, but equivalent, method would be to always treat $n \times m$ clusters as distinct from $m \times n$ clusters and measure entanglement across only a line in the y direction, for example. Both techniques require the same computational effort, but use different methods of bookkeeping.

Corner Entanglement

The entanglement due to a 90° corner in a boundary is isolated by subtracting off the entanglement contributions from the linear portions of the boundary. This is done by subtracting the entanglement due to the lines L^x and L^y , from entanglement across opposing lines with 90° vertices (V^1 and V^2), as shown in Figures 3.8 and 3.9. (Note that V^1 represents an infinite line separating the lower left quadrant from the rest of the plane, while V^2 separates the upper right quadrant from the rest of the plane.) To fully cancel off any line contributions to the entanglement we calculate the corner entanglement \mathcal{V}_α of an $n_x \times n_y$ cluster c using

$$\begin{aligned}
2\mathcal{V}_\alpha(c) &= \sum_{i=1}^{n_x-1} \sum_{j=1}^{n_y-1} [S_\alpha(V_{i,j}^1) + S_\alpha(V_{i,j}^2)] \\
&\quad - (n_y - 1) \sum_{i=1}^{n_x-1} S_\alpha(L_i^y) - (n_x - 1) \sum_{j=1}^{n_y-1} S_\alpha(L_j^x), \tag{3.15}
\end{aligned}$$

where $V_{i,j}^1$ denotes a region A including an $i \times j$ -site region of cluster c . In all cases in this thesis the two boundaries $V_{i,j}^1 = V_{i,j}^2$ will give the same results, though for non-rectangular clusters or a non-uniform Hamiltonian interaction it is possible that these two boundaries could give different results.

Though we follow Equation (3.15) to extract the corner entanglement, it is more intuitive to say that we measure the four terms in Figure 3.9 (right) for each of the plaquettes (Figure 3.9 (Left)), which easily extends to clusters of other shapes and sizes. In practice, due to the symmetry of the rectangular clusters, all V^2 measurements will already be done by V^1 . The number of measurements required can be further reduced for a square cluster, where $V_{i,j} = V_{j,i}$ for both V^1 and V^2 .

Though the above technique could be used for QMC on systems with open boundary conditions, the QMC does not have a numerical way to deal with the edge effects as the NLCE does. The edge effects are generally the reason numerical practitioners opt to use periodic boundary conditions, but for a system with periodic boundaries the shapes of the regions A and B would need to be changed, since an infinite line with a 90° angle would not give two separate regions on a torus. The technique is better suited to the NLCE, but it may be possible to find a better way to isolate the corner entanglement using QMC simulations.

3.5 NLCE Cluster Solvers

The NLCE is a method for summing results on finite clusters to get the result in the thermodynamic limit, but the technique does not specify where the finite size results must come from. In this thesis two techniques are used to extract finite-cluster results for the NLCE calculations, the Lanczos method and density matrix renormalization group (DMRG) calculations, though it is certainly possible to use other techniques together with the NLCE.

3.5.1 Lanczos & Full Diagonalization

In previous NLCE studies [57, 55, 56], generally the Lanczos algorithm [42] was used to obtain the full groundstate wavefunction of a cluster c , $|\Psi_c\rangle$. To extract the entanglement entropy for each of the different entanglement cut geometries (see Figures 3.8 and 3.9 for examples) one must take a partial trace of the full density matrix $\rho = |\Psi_c\rangle\langle\Psi_c|$ over the states in region B . The procedure to extract the Renyi entanglement entropies from the groundstate wavefunction is described in Section 1.5 in terms of Tensor Diagram Notation.

In Bra/Ket notation the partial trace is done by rewriting the groundstate vector in matrix form,

$$|\Psi_c\rangle = \sum_i a_i |\psi_c^i\rangle \rightarrow M_c = \sum_{j,k} a_{jk} |\psi_c^{Aj}\rangle \langle \psi_c^{Bk}|, \quad (3.16)$$

where a_i , a_{jk} are numerical coefficients normalized such that $\sum |a_i|^2 = \sum |a_{jk}|^2 = 1$, $\{\psi_c^i\}$ are basis vectors for the full cluster of both regions A and B , and $\{\psi_c^{Aj}\}$ and $\{\psi_c^{Bk}\}$ are the basis vectors of region A and B respectively. Computationally, this means constructing a matrix in which the rows represent the region A basis states and the columns represent the B basis states. Then, running through $|\Psi_c\rangle$, each entry is assigned to an element of M_c .

where $\psi_c^i = \psi_c^{A_j} \otimes \psi_c^{B_k}$. From there, obtaining the reduced density matrix simply requires multiplying this matrix by its conjugate transpose,

$$\begin{aligned} \rho_A &= M_c M_c^\dagger = \sum_{i,j} \sum_{k,l} a_{ij} a_{kl}^* |\psi_c^{A_i}\rangle \langle \psi_c^{B_j} | \psi_c^{B_l}\rangle \langle \psi_c^{A_k} | \\ &= \sum_{i,j,k} a_{ij} a_{kj}^* \langle \psi_c^{B_j} | \psi_c^{B_j}\rangle |\psi_c^{A_i}\rangle \langle \psi_c^{A_k} |. \end{aligned} \quad (3.17)$$

The order of multiplication $M_c M_c^\dagger = \rho_A$ or $M_c^\dagger M_c = \rho_B$ is chosen by which will result in the smaller reduced density matrix, since one final diagonalization must be done to extract its eigenvalues. M_c will have the dimensions $\text{Dim}(A) \times \text{Dim}(B)$, so if $\text{Dim}(A) > \text{Dim}(B)$ we choose ρ_B , otherwise we choose ρ_A .

The diagonalization of the reduced density matrix must give the full eigenvalue spectrum; this requires a more computationally expensive algorithm than Lanczos which only returns the largest eigenvalue(s). Finding the full spectrum is preferable if one wishes to calculate multiple Renyi EEs. If one only requires one or a small number of different EEs then it may be more efficient to raise the reduced density matrix to a the power of the α 's required. Then simply taking the trace of the undiagonalized matrix (instead of diagonalizing it first) and summing up the different powers of the eigenvalues is another way to obtain S_α . In our NLCE studies we use the NLCE to calculate Renyi EEs for ~ 200 values of α , so the full diagonalization is more computationally efficient.

The above method is limited by computer memory and time, and it is suitable mainly for smaller clusters. It is imperative to use a good linear algebra library as it will significantly improve the speed and performance of this algorithm. For this work the Eigen C++ template library [20] was used to measure entanglement entropy on clusters of up to 30 sites with Lanczos and exact diagonalization.

Of course, other measurements can also be done using the Lanczos method, with less difficulty as they would not require an additional diagonalization or multiple spatial divisions for a given cluster (unless it is another spatial quantity being considered, such as a correlation function).

3.5.2 Density Matrix Renormalization Group

For larger clusters DMRG is a nearly ideal cluster solver for entanglement entropies [65]. Unlike exact diagonalization and Lanczos, DMRG is not necessarily limited by the total number of sites in the cluster. Instead, the DMRG traverses the system along a one

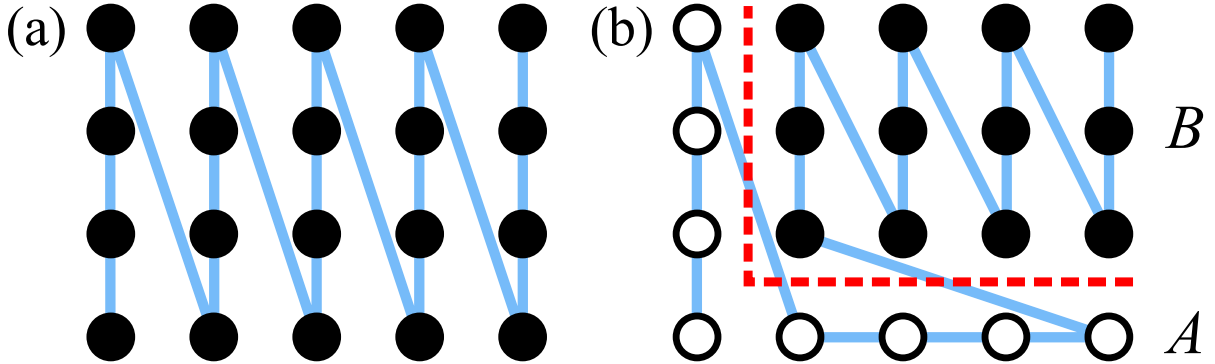


Figure 3.10: A typical path (a) used within DMRG for computing the groundstate of a 5×4 cluster. An irregular path (b) is needed to obtain the corner boundary dividing the system into regions A and B as shown.

dimensional path, an example of which is shown in Figure 3.10(a) for the 5×4 cluster. For a path like this, moving first along the shorter dimension n_y and second along the longer one n_x , the DMRG scales exponentially in n_y but scales much more favourably in n_x (e.g. linearly in n_x if the system is gapped) [73].

One key advantage of using DMRG to compute entanglement entropy is that as part of the algorithm the reduced density matrix is already obtained and diagonalized for a different bipartition of the system at every step, and no further calculation or diagonalization is required, as it is for the Lanczos. A related drawback is that the bipartitions calculated automatically correspond to cutting the one dimensional DMRG path at each bond, and therefore different and atypical DMRG paths need to be used to get all the required entanglement boundaries (see Figure 3.10(b)).

The path in Figure 3.10(a) provides two inequivalent vertical line cuts on the 4th and 8th bonds of the DMRG path, $L_1^y = L_4^y$ and $L_2^y = L_3^y$. The same path includes corner cuts separating sites in the first column from the rest of the system, $V_{1,1}^1$, $V_{1,2}^1$, and $V_{1,3}^1$. To get the L_i^x cuts the DMRG path must run in the less efficient direction, following the longer dimension first and then the shorter one, which scales exponentially in the longer dimension. Other corner cuts, such as the one separating the system into the regions A and B of Figure 3.10(b), require modifying the DMRG path. Paths that differ from the standard zigzag typically increase the computational cost for the DMRG to reach a fixed accuracy since short-range interactions in the two dimensional Hamiltonian are mapped to much longer-ranged interactions in the one dimensional model traversed by the DMRG.

A basic method for determining which paths will be more difficult for the DMRG to

converge to a given accuracy is to find the two interacting sites (nearest-neighbour in our case) with the longest path distance between them. The most efficient paths will minimize this number. In Figure 3.10(b) the bottom right site has to traverse 10 bonds before it is connected to the site directly above it. The statement that the DMRG scales exponentially in n_y for Figure 3.10(a) can be generalized to say that the DMRG scales exponentially in the longest path connection between neighbouring sites. A good strategy for entanglement measurements is to minimize the DMRG path distance between neighbouring sites along the entanglement boundary, since interactions closer to the boundary will generally have a larger effect on the convergence of the measurement than those far from the boundary.

Though many geometries required are not ideal for the DMRG algorithm, this method is still an improvement over Lanczos and exact diagonalization. In the NLCE study of the Heisenberg bilayer system below (Section 3.9.2) DMRG was used to reach system sizes of up to 40 sites, compared to only 30 sites with the Lanczos method. Bilayer systems are actually incredibly difficult for the DMRG, due to the addition of a third dimension over-which the 1D path must traverse the sites. More recent projects, not included in this thesis have seen clusters of up to 100 sites solved. The scaling of the algorithm is dependent on both the Hamiltonian model and on the aspect ratios of the clusters included, and the DMRG method can excel under the correct conditions.

3.5.3 Quantum Monte Carlo

Though quantum Monte Carlo (QMC) simulations have not yet been used as part of an NLCE study, there is no reason why they could not be. The NLCE algorithm requires that very accurate values of measurements be used, and with the necessity of the ratio trick (Section 2.3.2) to measure the entanglement for larger regions, using QMC could increase the computational time required for the NLCE by orders of magnitude. On the other hand, the typical system sizes reached by valence bond QMC are up to 1600 sites, so in comparison, a mere 100 site cluster would not require many iterations of the ratio trick in order to converge to an accuracy comparable to Lanczos or DMRG. The main drawback of QMC as an NLCE cluster solver is that it can only be used to measure integer Renyi entanglement entropies starting at $\alpha = 2$, where the computational difficulty is multiplied as α is increased.

3.6 NLCE in One Dimension

One dimensional (1D) systems are a special case for the NLCE, which works out to an almost trivial result. All subclusters of a 1D system can be labeled by their length n , and can be embedded in the infinite chain in only one way, thus $L(n) \equiv 1$ and

$$\mathcal{P}/\mathcal{N} = p(\infty) = \sum_{n=1}^{\infty} W(n). \quad (3.18)$$

The cluster weights are

$$W(1) = P(1) \quad (3.19)$$

$$W(2) = P(2) - 2W(1) = P(2) - 2P(1) \quad (3.20)$$

$$W(3) = P(3) - 2W(2) - 3W(1) = P(3) - 2P(2) + P(1) \quad (3.21)$$

\vdots

$$W(n) = P(n) - 2W(n-1) - 3W(n-2) \cdots - nW(1) \quad (3.22)$$

$$= P(n) - 2P(n-1) + P(n-2) \quad [n \geq 3]. \quad (3.23)$$

Defining sums of all weights up to a maximum order n_{\max} of the NLCE as

$$p(n_{\max}) = \sum_{n=1}^{n_{\max}} W(n), \quad (3.24)$$

then for $n > 1$

$$p(n) = P(n) - P(n-1). \quad (3.25)$$

The best estimate of the property per site for a 1D chain in the thermodynamic limit is simply equal to the difference between the values of the property on the two largest chains! All contributions from smaller sizes are cancelled out. It is interesting to observe from Eq. (3.25) that in 1D, the NLCE is nothing but the “subtraction trick” used in DMRG calculations to estimate bulk properties in the thermodynamic limit from finite systems with open boundary conditions [39, 73].

Unfortunately in 2D cluster weights do not simplify as in the 1D case, and all terms (even those from the smaller clusters) need to be included in Equation (3.8).

3.7 Convergence

The value of the weight $W(c)$ is an indicator of the convergence of the NLCE. In a system with no broken symmetries and a finite correlation length, the weights should decrease exponentially with cluster size, once these sizes exceed the correlation length. This would lead to an exponential convergence of the NLCE with cluster size, or length-scale ℓ . At (and near) a critical point, where the correlation length becomes large compared to the sizes of clusters we can study, the weights will vary as a power of the cluster size. This will lead to an algebraic convergence with order for quantities like groundstate energy and entanglement entropies, requiring a careful extrapolation. Some quantities will diverge at the critical point, but even for divergent properties, the NLCE can extract useful information if one can reach orders large enough for the property to be fit to a known scaling relation. The fact that some quantities converge and others diverge is analogous to convergence or divergence of a series expansion at its radius of convergence [39, 68].

3.7.1 Finite Size Scaling of Results

At critical points where correlation lengths diverge, though the NLCE will not converge directly to the thermodynamic limit results, we can still use it to obtain useful information. This is where the orders and length-scales defined in Section 3.3.5 become useful. The results can be fit to known scaling relations as a function of the cluster length-scale ℓ [21], corresponding to the maximum cluster sizes included in the NLCE sum of Equation (3.8). An example of this type of calculation is shown for the Heisenberg bilayer model in Figure 3.16.

It should be stressed that the NLCE is not a calculation for a finite size system, rather a systematic approximation for the thermodynamic limit, where the rectangles provide a way to sum up contributions from different length scales corresponding to the order of the cluster. NLCE can systematically encapsulate significantly larger-range correlations than conventional finite-size studies of toroidal clusters done with Lanczos diagonalization [38].

3.8 The Computational Process

This section outlines the steps required as part of an NLCE algorithm including the order in which they should be executed. The steps of the algorithm are listed below, and an equivalent flowchart is shown in Figure 3.11.

1. Determine which clusters are needed $\{c\}$ and their embeddings $L(c)$ in the lattice \mathcal{L} (Section 3.3).
2. Find subclusters $\{s\}$ for each cluster and their multiplicities $M(s)$. (See procedure in Section 3.3.3 for general clusters. This task is much simpler for rectangular clusters (Section 3.3.4).
3. Solve all clusters and measure the property $P(c)$.
 - (a) If $P(c)$ is entanglement (Section 3.4):
 - i. Determine entanglement cuts required for each cluster, $\{A_i\}$.
 - ii. $P(c) = \sum_i S_\alpha(A_i)$ for all entanglement cuts.
4. Calculate weights $W(c)$ starting from smaller clusters and building up (Equation (3.9)). For a given cluster, the weights of each of its subclusters must be calculated before its own weight can be calculated.
5. Sum weights to get P/N :
 - (a) Calculate partial sums for each order (Section 3.3.5)
 - or
 - (b) Calculate the full sum (Equation (3.8)).
6. If 5. (a) was chosen: Finite-size scale results based on known scaling relations (Section 3.7.1) to get the final results in the thermodynamic limit.

With the exception of Steps 1 and 2, which could be combined into a single program, each step should basically be its own component. Step 3, solving clusters, will be its own self-contained numerical algorithm, or possibly a collection of algorithms applied to cluster shapes and sizes for which they are best suited. In Step 4, the results of Steps 1 and 2 should be read in along with the results from Step 3, in order to sum up the results from the subclusters to obtain weights for each cluster. Step 5 is highly dependent of the choice of cluster order \mathcal{O} , so the weights for each cluster from Step 4 should never be thrown out, but saved so they can be summed using different methods. Step 6 is again its own component, which will be done differently for each different measurement, since the scaling relations will change based on the property that is studied. This step can be done separately for each different type of cluster order used in Step 5.

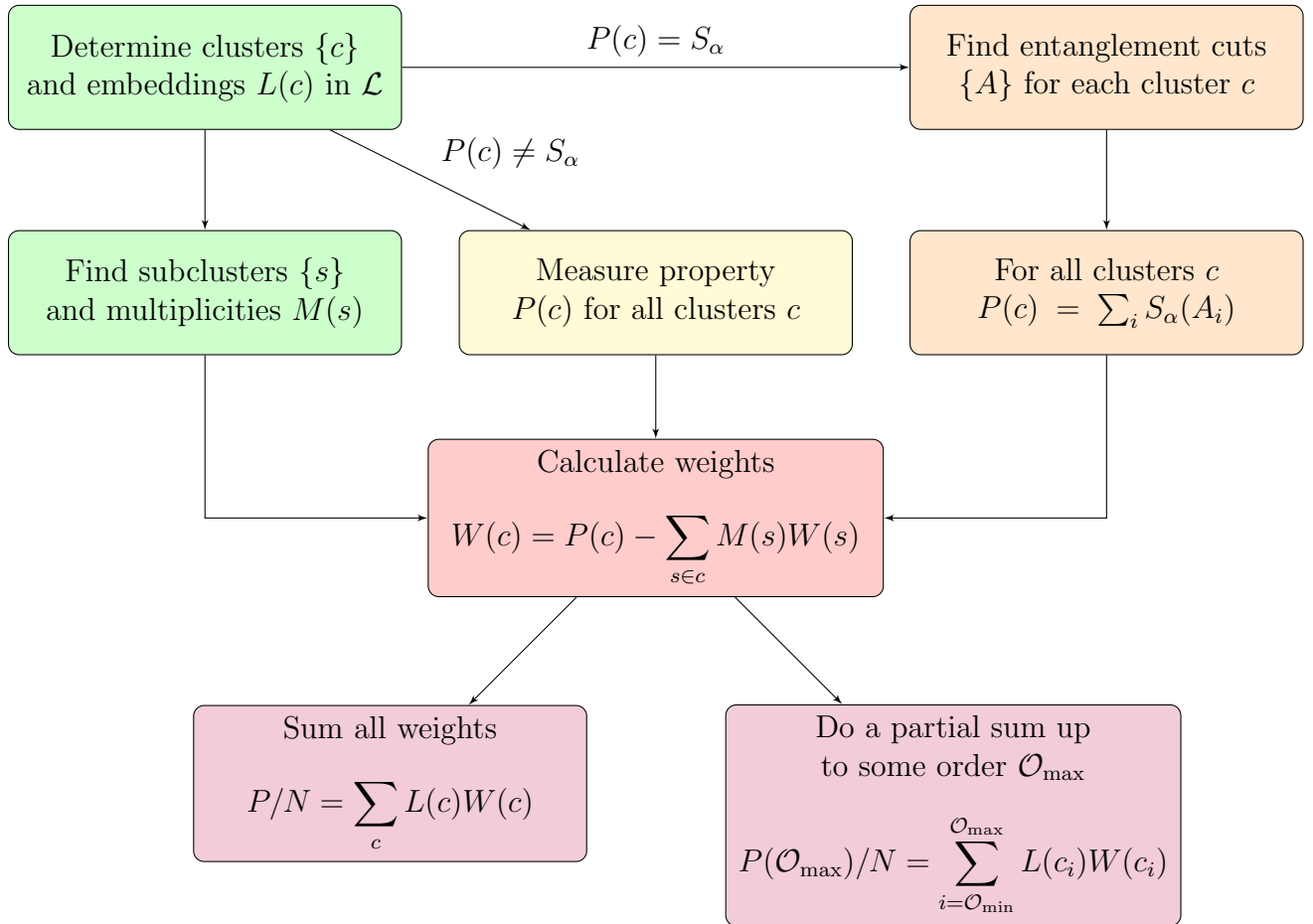


Figure 3.11: A flowchart outlining the steps necessary for the NLCE procedure. One should begin from the top left.

3.9 Entanglement Scaling at Quantum Critical Points

Quantum critical points (QCPs) exhibit some of the most highly entangled states in condensed matter physics [58]. This high degree of entanglement can be a challenge for some numerical methods [81], but it can also be viewed as a resource to detect and classify them. In particular, it is believed that the subleading scaling terms of the Renyi entanglement entropies contain universal coefficients [10, 48]. These universal terms can be studied in quantum many-body models using numerical techniques, such as quantum Monte Carlo (QMC) simulations or exact diagonalization, and compared to quantum field theories as a way of determining the universality class of a QCP. Thus, it is important to have unbiased numerical methods that can calculate these universal numbers for a quantitative comparison to field theories, models, and perhaps some day, experimental studies [8, 1].

This section shows results using the numerical linked-cluster expansion technique to study the subleading term in the Renyi entanglement entropies due to the presence of a 90° corner in the boundary between regions A and B for the transverse-field Ising model (Section 1.2.4) at its QCP and the Heisenberg bilayer model (Section 1.2.3) at its QCP. (In general it may be illuminating to study the coefficient for angles other than 90° , however that would require working with a different type of lattice, so for now we limit ourselves to this one angle.) These results are compared to predictions from field theories [38, 49] and to results from a variety of numerical techniques. The corner entanglement from the two models are compared and there is evidence that its coefficient is a universal number that yields the number of degrees of freedom necessary to represent the underlying model through quantum field theory [39].

The NLCE is performed using rectangular clusters, with both Lanczos and density matrix renormalization group (DMRG) calculations employed to measure the Renyi entanglement entropies (EEs) for arbitrary real Renyi index α on the clusters. The results are extrapolated as a function of the order of the calculation, to obtain universal pieces of the entanglement entropy associated with lines and corners at the quantum critical points of these two models. The NLCE is shown to be one of the few methods capable of accurately calculating universal properties of arbitrary Renyi entropies at higher dimensional critical points.

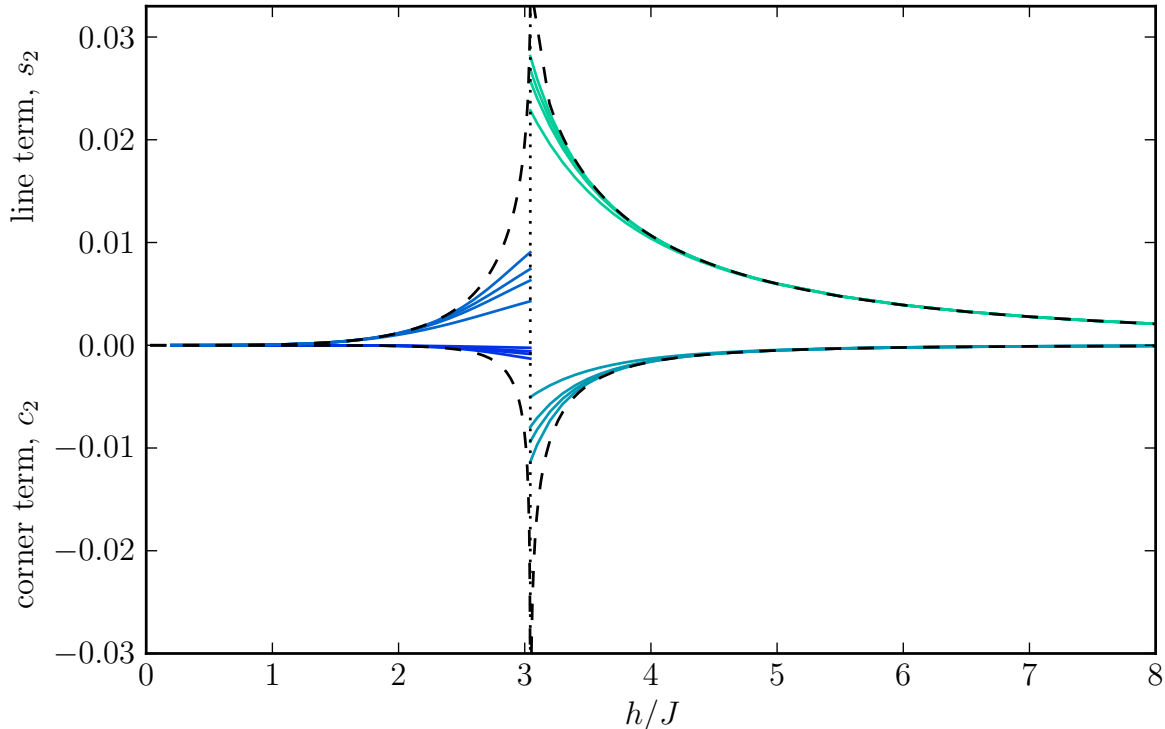


Figure 3.12: The entanglement due to a corner c_2 and entanglement due to a line s_2 as a function of h/J for the second Renyi entanglement entropy using both high field and low field NLCE, and truncating to orders $\mathcal{O}_G = 8, 12, 16,$ and 24 . The dotted line denotes $(h/J)_c = 3.044$ and the dashed lines show the series expansion results [70].

3.9.1 The Transverse Field Ising Model

We use the NLCE to study the scaling of the Renyi entanglement entropies at the quantum critical point of the 2D transverse-field Ising model (TFIM) (Section 1.2.4),

$$H = -J \sum_{\langle ij \rangle} \sigma_i^z \sigma_j^z - h \sum_i \sigma_i^x. \quad (3.26)$$

This model has a quantum critical point at $(h/J)_c = 3.044$ [54], at which most of this section is focused.

First however, Figure 3.12 shows results as a function of h/J for line s_2 (3.14) and corner c_2 (3.15) EEs for different maximum orders. The dashed line shows the results from

a series expansion calculation [70]. The series expansion values were calculated only for the second Renyi EE, and not for a range of EEs simultaneously as the NLCE can accomplish.

Note the difference in values on either side of the critical point. In order to improve convergence for $h < h_c$, it is necessary to include a static ordered moment for the sites on the outside of the cluster, i.e. it is as if each cluster is surrounded by a row of extra sites which are all spin up, for example. These extra sites interact with the sites around the edge of the cluster via the first term in the Hamiltonian (3.26), breaking the spin up / spin down degeneracy. This is analogous to a low field series expansions, where the small parameter in the expansion is the field, and we therefore call it *low field* NLCE. For $h \geq h_c$ no such boundary field is needed and we call it *high field* NLCE.

Each of the low field and high field corner term calculations and line term calculations show results truncated to orders 8, 12, 16, and 24, where the geometric order \mathcal{O}_G (3.11) is used. The results increase in magnitude as they increase in order. Away from the critical point the NLCE results converge to the series expansion results at a low order, but closer to the critical point where the correlation length diverges, the NLCE is still increasing as a function of order up to $\mathcal{O}_G = 24$.

For the remainder of this chapter we will focus on the regime at and near the quantum critical point, using the high field NLCE for the TFIM, which has the advantage over the low field expansion near the QCP as those results are much closer to the series expansion values for lower orders.

Corner Term

As discussed in Section 1.3.2, the corner term a_α is expected to harbour a universal quantity in its coefficient. The NLCE technique is used to measure this quantity and extract the coefficient for a range of Renyi EEs for the TFIM at its QCP. The scaling of entanglement, then, for this system should look like,

$$S_\alpha = d\ell + a_\alpha \ln(\ell) + b, \tag{3.27}$$

where the first term is the non-universal area law scaling, the second term is the universal entanglement due to the presence of a corner [10] and the final term is a non-universal additive constant. Using the NLCE technique we are able to cancel off the $d\ell$ area law term, isolating the entanglement due to a corner, $c_\alpha = a_\alpha \ln(\ell) + b$.

Figure 3.13 shows the behaviour of the corner term c_α at the QCP for select values of α . The corner terms c_α are shown vs $1/\ell_G$, plotted on a logarithmic scale so the linear

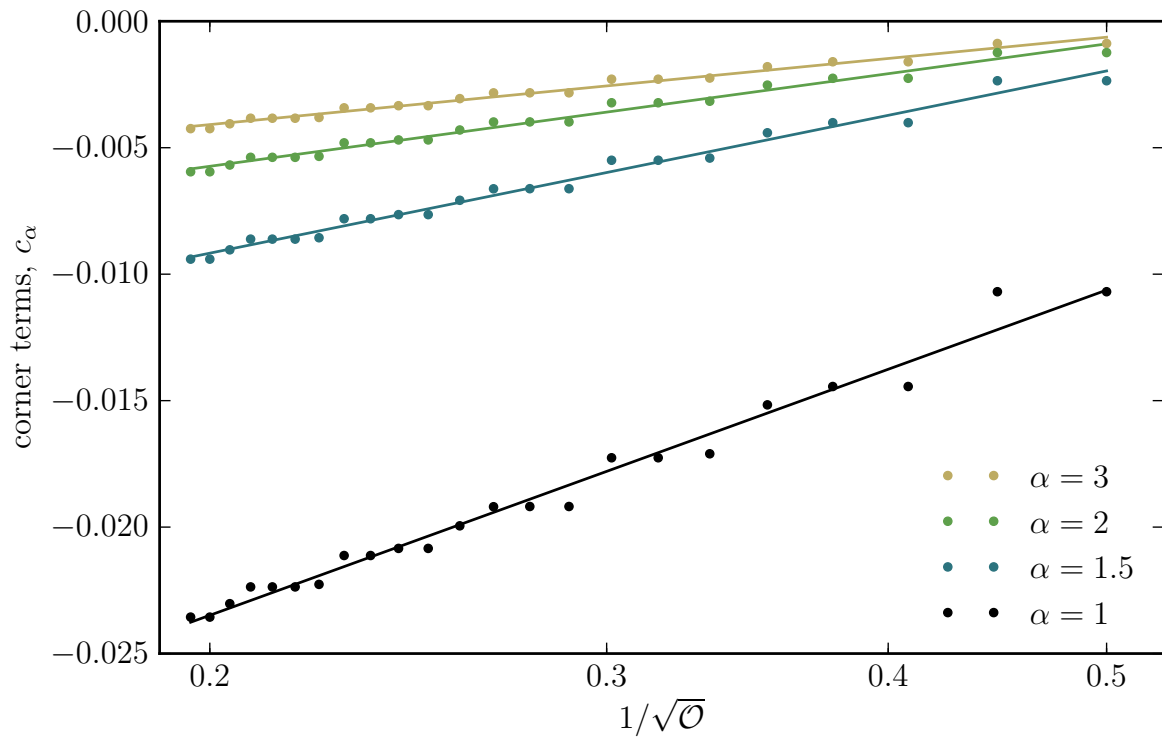


Figure 3.13: The corner term c_α for $\alpha = 1, 1.5, 2, 3$ along with fits to $a_\alpha \ln \sqrt{\mathcal{O}_G} + b_\alpha$ plotted vs $1/\sqrt{\mathcal{O}_G}$ on a logarithmic scale.

behaviour is obvious. The slopes of these linear fits are universal terms a_α for each value of α .

Figure 3.14 shows the resulting coefficients a_α from fits of c_α to $a_\alpha \ln(\sqrt{\mathcal{O}_G}) + b_\alpha$ as a function of Renyi index. Each value of α requires a separate fit. The figure shows data truncated to orders $\mathcal{O}_G = 10, 14, 18, 22$, and 26 , along with shaded regions indicating the error in a_α from each fit. The error used is the square root of the covariance matrix entry for a_α from the fit using `numpy.polyfit` of the SciPy python library [34]. This estimate assumes that the data is normally distributed, but as one can see from Figure 3.13 it is not. In fact the NLCE data for each order has no statistical error, and would only have error due to the numerical imprecision of stored values *or* due to an imperfect definition of length scale in relation to the orders of clusters used (i.e. the step-like distribution seen in Figure 3.13).

Figure 3.15 shows the untruncated results up to $\mathcal{O}_G = 26$ (the largest order calculated for the TFIM) along with values of this universal constant a_α , as calculated by other methods. The coefficient a_2 has been calculated for the 2D TFIM using several different numerical methods. In Ref. [70], series expansion found $a_2 = -0.0055(5)$ ¹. Zero-temperature projector QMC calculations report $-0.006(2)$ [31]. Our current NLCE calculation gives $-0.0052(2)$ —a number consistent with the series expansion and QMC results.

This value of a_2 for the TFIM has been compared several times in the past literature to the value calculated analytically by Casini and Huerta for a free scalar field theory, $a_2 = -0.0064$ [9]. Although this is numerically close to the NLCE value of -0.0052 , in fact one should not expect correspondence since this is an interacting model that is not described by a free Gaussian fixed point. Rather, one would need a calculation of the quantity in an interacting theory (the “Wilson-Fisher” fixed point) to see a proper correspondence, though so far no such calculation has been done.

The universal term a_1 has been calculated once previously using a tensor network variational ansatz called the “tensor tree network” (TTN), by Tagliacozzo and co-workers [76]. Their value for the universal coefficient is $a_1 = -0.0095(1)$. The value from free scalar field theory is -0.012 [10]. The value from the present NLCE work up to order $\mathcal{O} = 26$ is $a_1 = -0.0140(4)$, a number as close as the TTN result to the free field value, though above instead of below it.

¹Note that the value of -0.011 ± 0.001 reported in Ref. [70] is actually due to two corners, not one.

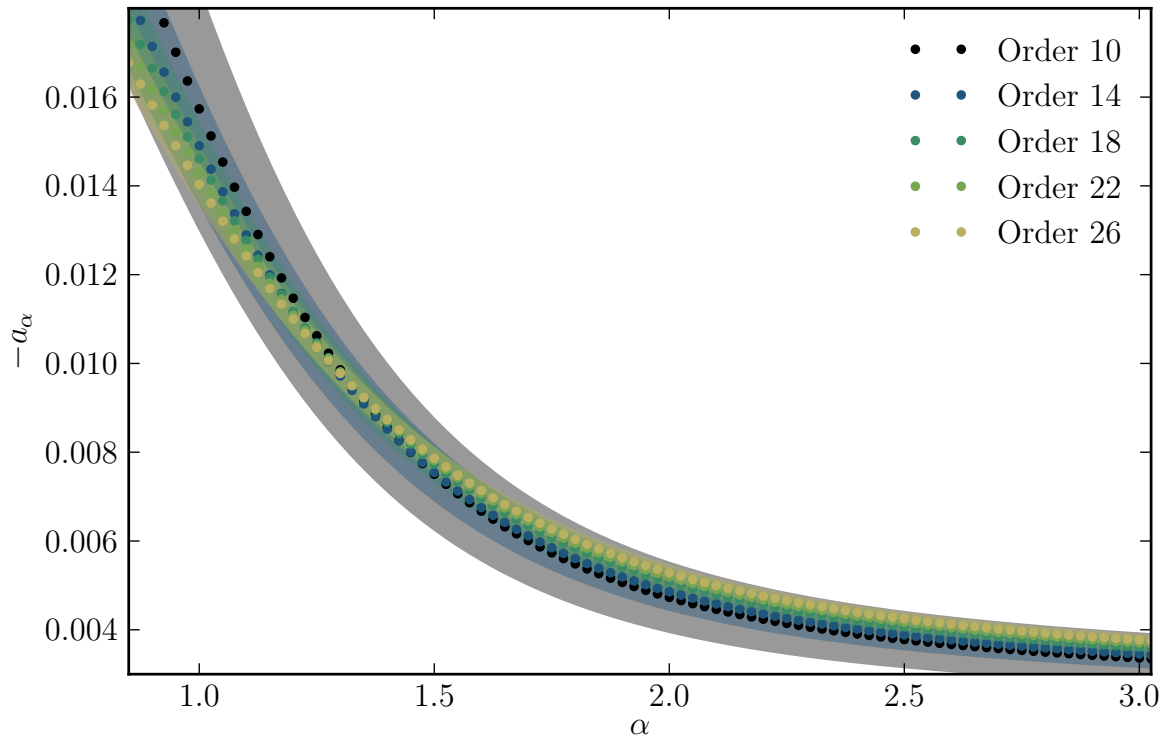


Figure 3.14: The coefficient $-a_\alpha$ from fitting c_α (examples shown in Figure 3.13) to the function $a_\alpha \ln \sqrt{\mathcal{O}_G} + b_\alpha$. These fits were done over a range of α s with the order \mathcal{O}_G truncated to 10, 14, 18, 22, and 26. The shaded regions signify the error in the fits, calculated using the covariance matrix.

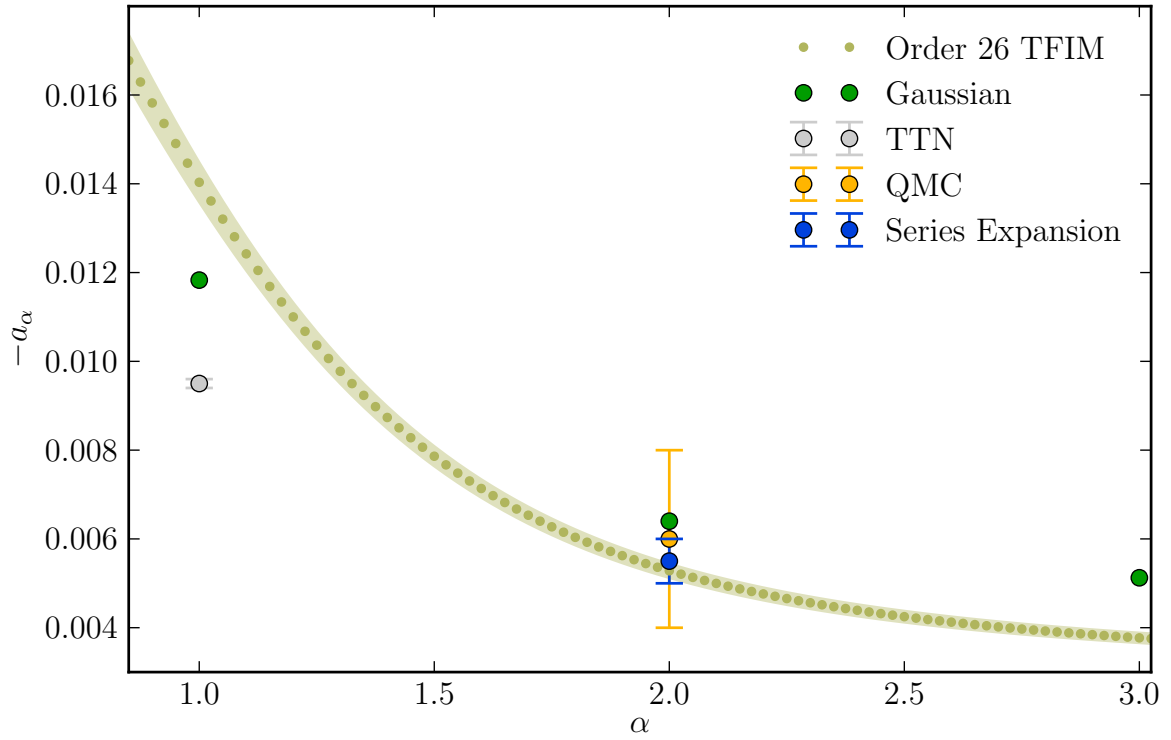


Figure 3.15: The coefficient $-a_\alpha$ from fitting c_α to the function $a_\alpha \ln \sqrt{\mathcal{O}_G} + b_\alpha$ for orders up to $\mathcal{O}_G = 26$ plotted along with other numerical estimates of $-a_\alpha$ from free scalar field theory (“Gaussian”) [10], tensor tree network (“TTN”) [76], T=0 QMC [31], and Series Expansion [70]. Error from the fits is indicated by the yellow shaded region.

3.9.2 The Heisenberg Bilayer

In this section we study the entanglement on a square lattice Heisenberg bilayer system (Section 1.2.3) at its QCP, $(J_{\perp}/J)_c = 2.5220$ [83]. Each cluster used in the calculation is an $n_x \times n_y \times 2$ array of sites, where $n_x, n_y \geq 1$. The second layer of the bilayer lattice does not change the NLCE calculations from the strictly 2D NLCE, other than doubling the number of sites in a given cluster, increasing the computational expense of solving each cluster.

DMRG calculations (performed using the code of M. Stoudenmire) are used to solve clusters of greater than 30 sites, while Lanczos is used for all smaller clusters. Each DMRG calculation kept up to 10,000 states or enough states to obtain a truncation error below 10^{-12} , whichever occurred first. (In DMRG simulations the truncation error is the difference between the trace of the generated reduced density matrix of the system and one, i.e. the sum eigenvalues of ρ_A that are discarded in the simulation. When the truncation error is zero the DMRG calculation is equivalent to performing Lanczos.) The only exception was one of the irregular paths for the $4 \times 5 \times 2$ cluster for which we only managed 8000 states (due to memory constraints) for a truncation error of 1.4×10^{-9} , which is still quite accurate. The accuracy of difficult clusters can be benchmarked by comparing the energy between the cluster with an irregular path (see Figure 3.10) or a less efficient path such as a cluster for which $n_y > n_x$, with the same cluster with the standard zigzag path. For the $4 \times 5 \times 2$ cluster with the difficult irregular path, for example, we still obtained the energy within a relative error of 10^{-9} compared to the $5 \times 4 \times 2$ result, which is essentially exact to numerical precision.

The subleading logarithmic term in the Renyi entanglement entropy resulting from a corner of angle 90° in the boundary between regions A and B on the Heisenberg bilayer is measured using NLCE. These results are compared to the above results for the quantum critical point in the 2D transverse-field Ising model on the square lattice [38], in order to examine the relation between the two.

Before discussing results for the Renyi EEs, an initial check of the NLCE procedure for the Heisenberg bilayer is performed. Figure 3.16 shows the groundstate energy per site in the Heisenberg bilayer at its QCP. The points are calculated using the NLCE with both arithmetic and geometric orders. These data are plotted versus $1/\ell$ (using the corresponding definitions ℓ_A and ℓ_G) so that the extrapolation to the thermodynamic limit uses $1/\ell \rightarrow 0$. The results are fit to $1/\ell^3$ following the lead of Sen and Sandvik [61] who fit the finite temperature Heisenberg bilayer energy to a function of $1/T^3$ at low temperatures, where T plays the role of the correlation length [67].

Each dataset is fit to the function $E_0(\ell) = b/\ell^3 + E_0(\infty)$, where b is some constant and

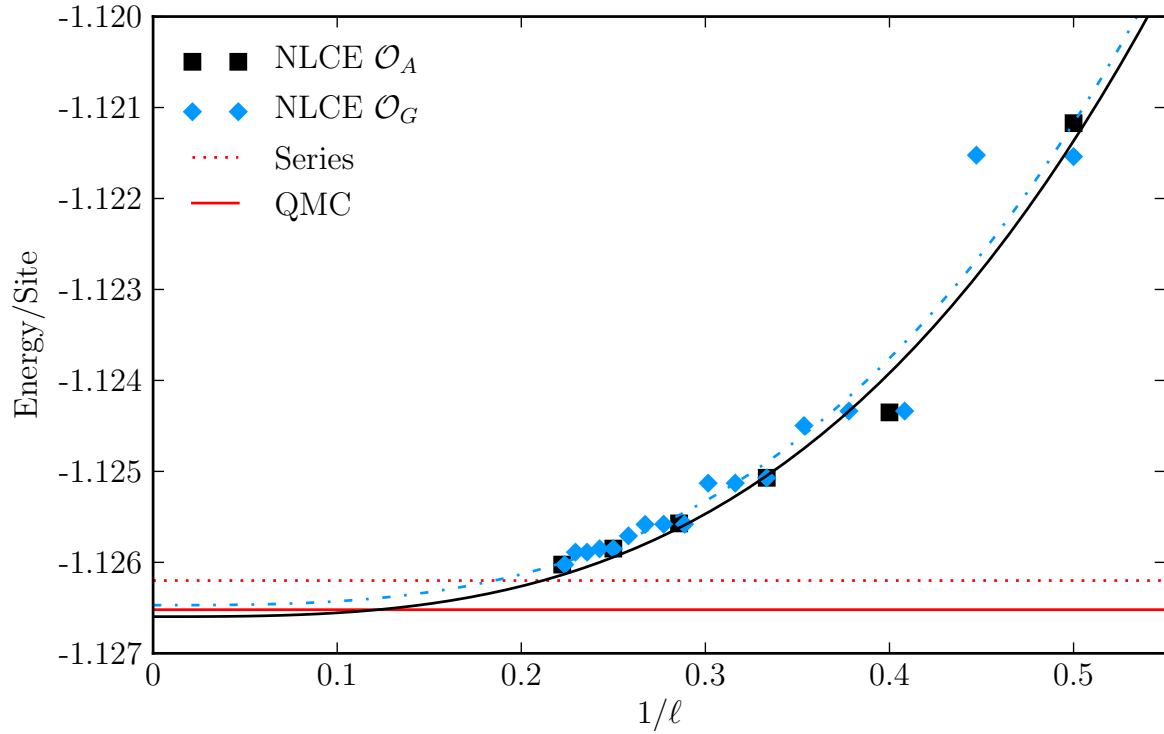


Figure 3.16: The energy per site for the Heisenberg bilayer system at its quantum critical point as a function of $1/\ell$ along with fits to $b/\ell^3 + d$ for some constants b and d . The resulting values of d give predictions for the groundstate energy in the thermodynamic limit, $E_0(\infty)$. The horizontal lines are predictions for $E_0(\infty)$ from series expansion [67] and quantum Monte Carlo [61].

$E_0(\infty)$ is the predicted groundstate energy per site in the thermodynamic limit. For the two different fits we find,

$$\begin{aligned}\mathcal{O}_A : E_0(\infty) &= -1.1266(2) \\ \mathcal{O}_G : E_0(\infty) &= -1.1265(2).\end{aligned}$$

Even though relatively small cluster sizes are included in this extrapolation, we see that both values of $E_0(\infty)$ are very close to two independent calculations from complementary, but very different techniques. First, from series expansions, Pade extrapolations lead to a value of $E_0(\infty) = -1.1262$ [67] at $(J_\perp/J)_c = 2.5220$. Second, from large-scale unbiased quantum Monte Carlo, Sen and Sandvik [61] reveal a highly accurate value of $E_0(\infty) = -1.1265201(5)$ at the quantum critical point, which is again consistent with the NLCE results.

Corner Term

As discussed in Section 1.3.2 and above in Section 3.9.1 the entanglement due to the presence of a corner in the boundary between regions A and B harbours a universal coefficient, a_α . By measuring that coefficient in the Heisenberg bilayer system as well as the 2D TFIM, we are examining two different universality classes which should yield distinct values.

For each value of the Renyi index α , we extract the value of $a_\alpha(90^\circ)$ directly from fits of this corner entropy to

$$c_\alpha(\ell) = a_\alpha \ln \ell + b_\alpha. \quad (3.28)$$

The raw NLCE data for this quantity is shown in Figure 3.17, for several values of α . Data are plotted for two definitions of order, \mathcal{O}_A and \mathcal{O}_G , and separate fits are performed for each value of α to Equation (3.28), as a function of the cluster length scale ℓ , to extract a_α and b_α . Using \mathcal{O}_A results in a systematically higher value of b_α , though the difference decreases as α increases.

Using this fitting procedure, results for the log-coefficient a_α are plotted in Figures 3.18–3.20. Each of these figures includes comparisons between three different models: the 2D TFIM at its QCP [38] (yellow line), the free field theory at its Gaussian fixed point [10] (green circles), and the Heisenberg bilayer at its QCP [39]. The Heisenberg bilayer results are divided by 3 to emphasize how remarkably closely they then correspond to the TFIM data.

The first figure, 3.18, shows results truncating the geometric orders from $\mathcal{O}_G = 10, \dots, 20$. The errors in the fits are denoted by the shaded regions with the corresponding colour.

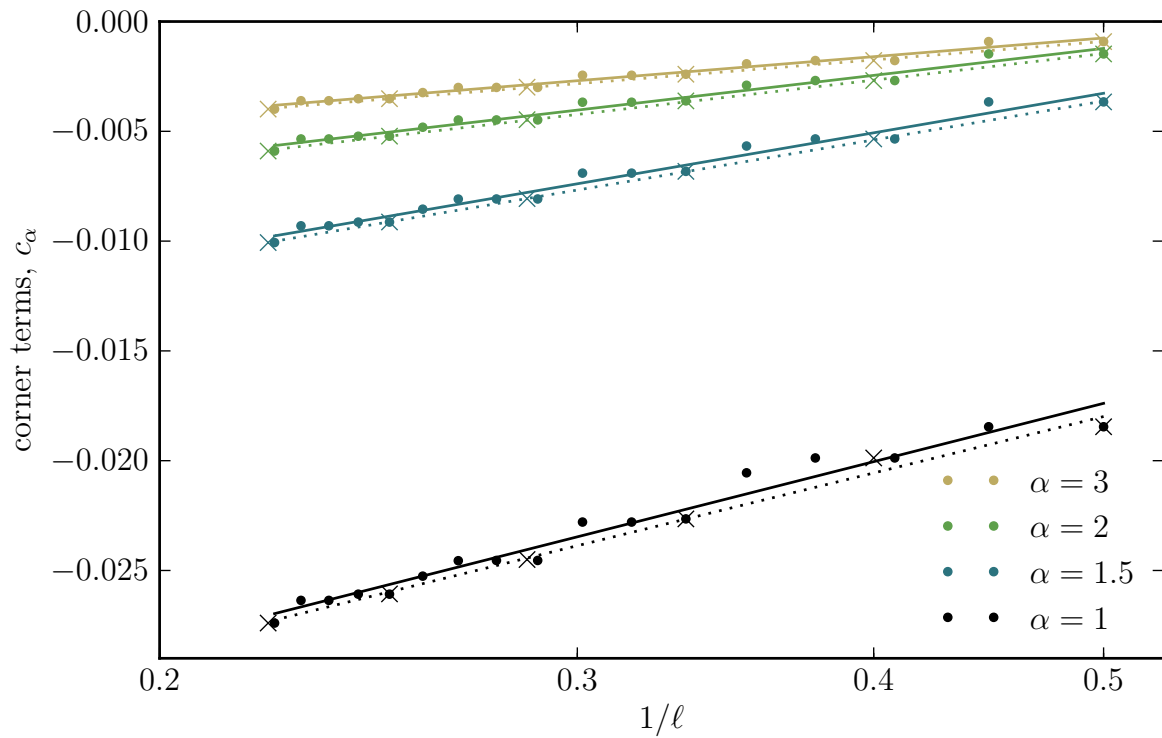


Figure 3.17: The corner term c_α for $\alpha = 1, 1.5, 2, 3$ along with linear fits plotted vs $1/\sqrt{\mathcal{O}}$ on a logarithmic scale. The arithmetic orders are denoted by the \times 's and the corresponding fits are shown with dotted lines. The filled circles represent the geometric order points, and the solid lines are the fits to these points.

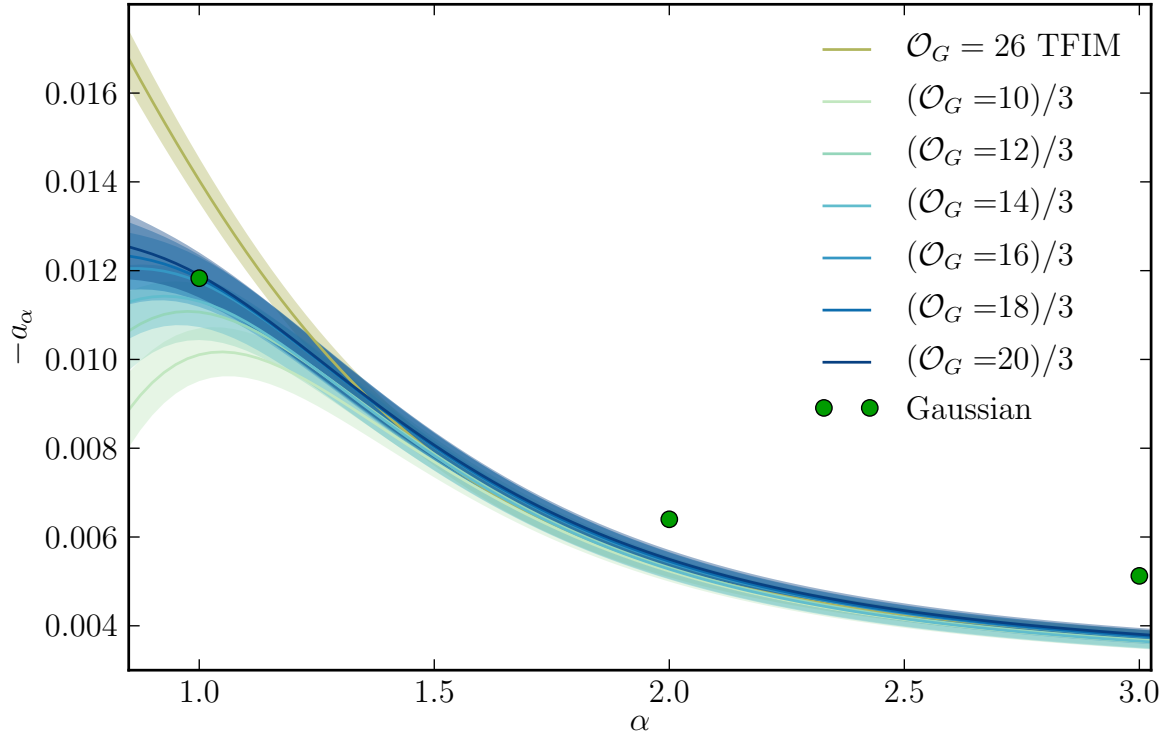


Figure 3.18: Results for $a_\alpha/3$ from fitting bilayer corner term data c_α to (3.28) for geometric orders $\mathcal{O}_G = 10, 12, 14, 16, 18, 20$. Errors in the fits are shown by the shaded regions with the corresponding colour. TFIM results are plotted in yellow, and the green points are analytical results for a free field theory [10].

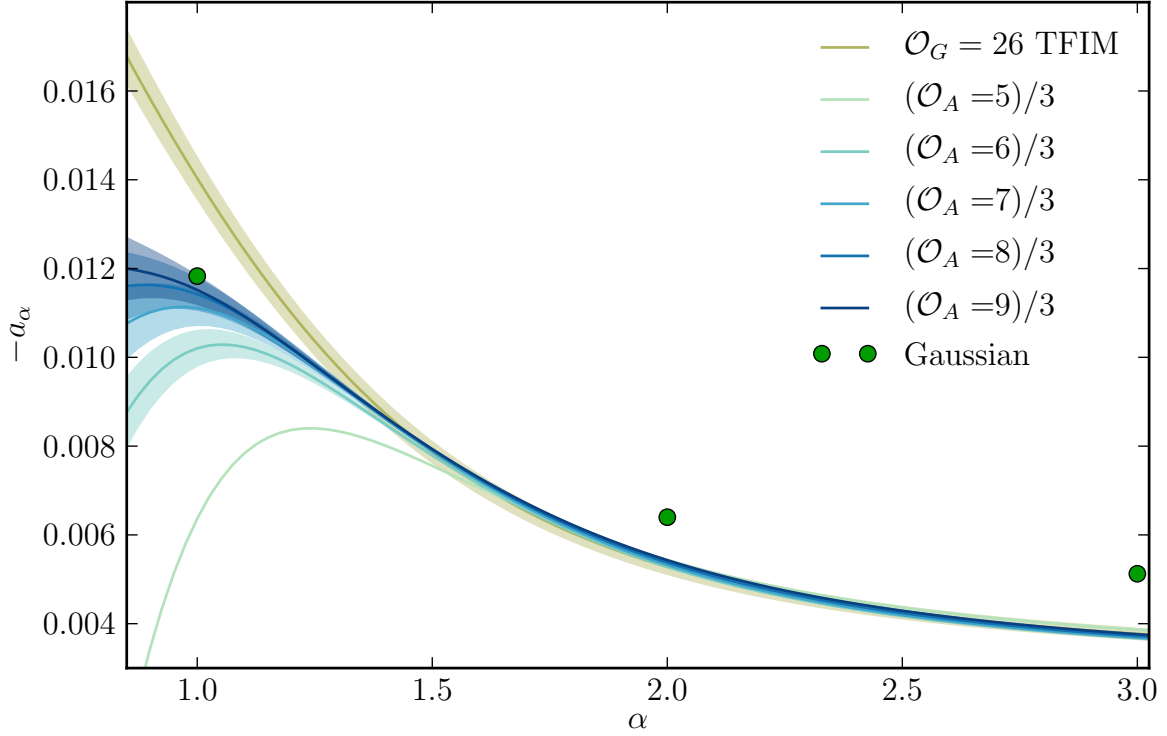


Figure 3.19: Results for $a_\alpha/3$ from fitting bilayer corner term data c_α to (3.28) for arithmetic orders $\mathcal{O}_A = 5, 6, 7, 8, 9$. Errors in the fits are shown by the shaded regions with the corresponding colour. TFIM results are plotted in yellow, and the green points are analytical results for a free field theory [10].

One can see that as higher orders are included in the fits to (3.28) the coefficient a_α is mainly affected in the range of small α and not much change occurs for larger α . This may indicate that the discrepancy between the bilayer and TFIM results would disappear upon the inclusion of larger cluster sizes in the bilayer.

Figure 3.19 shows the same information as Figure 3.18, but now uses the arithmetic definition of order. These data show a more drastic change as the maximum order included in the calculation is reduced only because arithmetic orders contain a larger number of clusters per order as the order is increased. The line with the least amount of data does not even include error bars because the data set only contains two points per α , $\mathcal{O}_A = 4$ containing the 2×2 cluster, and $\mathcal{O}_A = 5$ containing the 2×3 cluster.

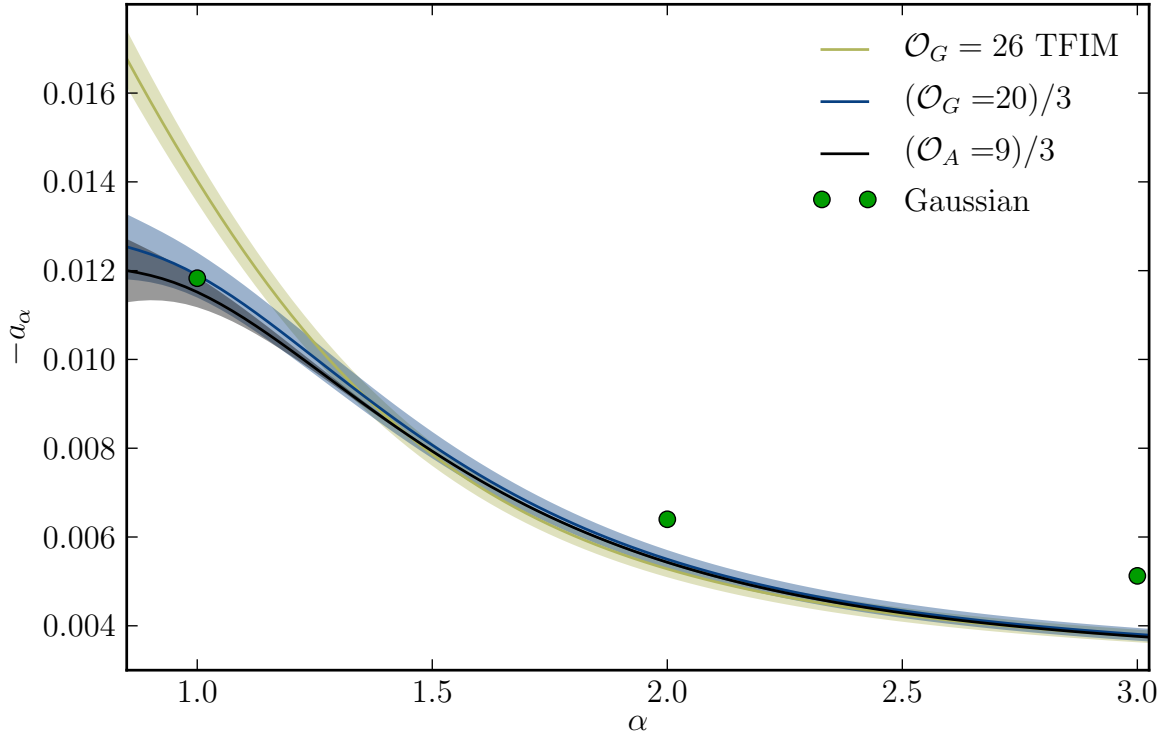


Figure 3.20: Results for $a_\alpha/3$ from fitting bilayer corner term data c_α to (3.28) for the untruncated geometric and arithmetic orders $\mathcal{O}_G = 20$ and $\mathcal{O}_A = 9$. Errors in the fits are shown by the shaded regions with the corresponding colour. TFIM results are plotted in yellow, and the green points are analytical results for a free field theory [10].

The final corner coefficient Figure, 3.20 includes only the fits using the untruncated data, up to: $\mathcal{O}_A = 9$ and $\mathcal{O}_G = 20$.

The error bars shown in Figures 3.18 - 3.20 are meant to be a guide to the reader. They are calculated as the standard deviation of the data from the linear fits to $\mathcal{V}_\alpha(\ell) = a_\alpha \log \ell + b_\alpha$, examples of which are shown in Figure 3.17. This error is then assigned to a_α , although strictly speaking it also depends on b_α . As with any study of this kind which incorporates functional extrapolations using relatively small cluster sizes, significant uncertainty related to the precise data series included in the fit remains, and is not represented by the error bars in these figures.

It is worth noting that (as shown in the previous section) the NLCE results [38] for the second Renyi entropy S_2 in the TFIM were independently benchmarked against series-expansion [70] and QMC data [29, 31] obtained through a replica trick procedure. Both calculations yield a coefficient a_2 consistent with the NLCE to within numerical errors. The unbiased QMC data were obtained from a much different fitting procedure involving a square subregion A with four corners embedded in a toroidal lattice; thus the match with the NLCE is particularly striking, and gives confidence that the NLCE procedure is working.

3.9.3 Discussion

This work has employed the numerical linked-cluster expansion technique (NLCE) [57, 55, 56], modified to use only rectangular clusters so as to shift the computational bottleneck of the algorithm from the problem of finding all clusters and subclusters to the problem of solving those clusters. The NLCE technique has also been modified to measure the Renyi entanglement entropies, which breaks the translational symmetry of all clusters on the infinite plane, and thus adds to each measurement an extra sum over translations of the cluster across a boundary. Modifying the type of clusters considered is not an uncommon practice for linked-cluster expansion (though usually it just amounts from replacing the site or bond base-unit with a plaquette), however the NLCE technique had not been used to study entanglement before this work on the TFIM in 2013 [38].

This technique has been used to study the entanglement entropy due to the presence of a 90° corner in a boundary, which was predicted [10] to yield a term that scales logarithmically with the length-scale of the system, the coefficient of which is said to be universal. The coefficient of the logarithmic term, a_α was extracted at the quantum critical points of two models, the transverse-field Ising model (TFIM) and the Heisenberg bilayer model.

For the TFIM this coefficient was measured on clusters of up to 26 sites, and NLCE results were compared to results from free scalar field theory [10], tensor tree network (TTN) [76], T=0 QMC [31], and series expansion [70]. The QMC, TTN, and series expansion results were all specifically for the TFIM. The large discrepancy between the TTN results and our NLCE results is likely due to a limited bond dimension for the TTN which cuts off the tail of the reduced density matrix that (as discussed below for the bilayer results) the $\alpha < 1.5$ EEs rely heavily upon compared to the larger α EEs. The series expansion results and QMC results, however, both agree with the NLCE results within errors (Figure 3.15).

The free scalar field theory results are not expected to agree with the NLCE TFIM results as they are from a non-interacting field theory, while the TFIM is certainly a model of strong interactions, and thus the field theory values should not accurately capture the entanglement characteristics of the TFIM. The free field theory results, which we only have values of a_α for $\alpha = 1, 2$, and 3, show a similar shape to our results for the TFIM and a similar magnitude, but do not agree within our NLCE error bars. However, based on the shape of the a_α versus α curve in relation to the results from non-interacting field theory in Figure 3.15, it is possible that $\alpha = 2$ may not be the optimal Renyi index to make comparisons when looking for a universal coefficient with which to distinguish different classes of models, as the values are close in that range. Note particularly the QMC results, which have the largest error bars, are not actually able to distinguish between the TFIM and field theory values. It is possible that larger alpha values (e.g. S_3) might be more suitable to distinguish the free field theory this interacting theory.

In the Heisenberg bilayer system the corner coefficient a_α is studied, both as a function of truncation order, and compared to the TFIM and free field theory results. It is found that the $\alpha < 1.5$ regime of a_α is very sensitive to the truncation order used, which is not the case for the TFIM. The $\alpha > 1.5$ portion of the coefficient a_α is found to be much less sensitive to the truncation order used, converging at a relatively low order. This is not entirely surprising, as the $\alpha < 1.5$ Renyi EEs are much more sensitive to the tail of the entanglement spectrum. And, at least for gapped systems, it has been argued that the closer a reduced density matrix eigenstate's eigenvalue is to the tail of the entanglement spectrum, the further it probes the system away from the cut [80].

Another striking fact to notice between these two models is that the bilayer corner coefficient is almost precisely three times the magnitude of the TFIM coefficient. This result has been hypothesized to be the coefficient a_α counting *degrees of freedom* in the underlying field theories describing these two models. The Heisenberg bilayer at its QCP can be described by an $O(3)$ ϕ^4 field theory, where the field ϕ has three components. The TFIM, on the other hand can be represented by an $O(1)$ scalar field theory where ϕ has only one component. Currently we are working on an NLCE calculation at an $O(2)$ critical

point in order to further test this hypothesis.

It is clear from Figure 3.20 that some uncertainty remains regarding the relationship between the data for $\alpha \lesssim 1.5$. Though it seems possible, considering how that region is still increasing in magnitude as more orders are included, that this “droop” may disappear, it remains possible that deviations, corrections, or even a phase transition in α may change the factor of three relationship in this region [48]. Despite the uncertainties, these results give substantial support to the hypothesis that a_α for the Heisenberg bilayer at its critical point is approximately three times the value for the TFIM at its critical point.

Thus the NLCE has been used to study this universal coefficient at two different quantum critical points, and has been shown to be an ideal tool for numerically extracting subleading terms in the Renyi EEs.

3.9.4 Future Work

Since the development of the NLCE entanglement measurement in 2013 [38], we have barely scratched the surface of what this technique is capable of.

One interesting problem, and a good “check” of the results in Chapter 2, would be to use the NLCE to study the 2D Heisenberg model. The corner term, which may or may not be universal, could be extracted directly and compared to the numerical value from QMC as well as to the TFIM and bilayer data. The 2D Heisenberg model is not a critical system as those two systems are, but it does have a diverging correlation length and a large amount of entanglement. The Heisenberg entanglement entropy on a torus is around a factor of 3 – 4 times greater than that of the TFIM at its QCP [35, 31]. It would be interesting to see whether the corner term behaves universally as it does for the TFIM and bilayer models.

Additionally, the line term for this model could be measured to obtain a more accurate value for the universal subleading logarithm due to the presence of Goldstone modes. The coefficient of this term was predicted to be exactly 1 for the Heisenberg model [49], but VB QMC studies yielded a result closer to 0.74 [37]. The NLCE should in principle be able to obtain a more accurate value if the discrepancy is due to the limited system sizes in the QMC study.

Another study, which I have mentioned previously in this chapter, is the study of an $O(2)$ quantum critical point in order to give further evidence toward the argument that the factor of three in the corner coefficient of the bilayer model compared to the TFIM is due to the counting of degrees of freedom in the underlying field theory. If this is the case

then an $O(2)$ model should yield a factor of two in this coefficient. This project is currently underway using DMRG as the cluster solving technique up to system sizes of 100 sites.

A different idea is to move back toward the “roots” of NLCE by changing the types of clusters studied once again. Instead of restricting the clusters to a rectangular shape one could instead build clusters out of square plaquettes. This would significantly decrease the number of clusters from the general case, but increase the complexity and number of clusters compared to the rectangular case. This method might be suitable to study the 2D Heisenberg model where some of the symmetry of the Hamiltonian is restored when different groups of sites are considered. It could also solve problems in systems that do not converge (as with the Heisenberg model) when including odd-width clusters, due to the fact that the wavefunction between the even and odd width cases on small scales changes so dramatically, though another solution to that problem would be to include a staggered field around the boundary of the clusters, similar to the *low field* expansion mentioned earlier.

One property of the NLCE technique that I have failed to mention thus far is that it can be used to study systems which suffer from the infamous “sign problem” in QMC. The sign problem is a term for the difficulty of accruing negative weights in a QMC simulation, or weights which have a random sign. These weights are intended to be interpreted as a probability, which is no longer reasonable when they are not all of the same sign, thus the sign problem makes a model impossible to study via QMC. On the other hand, exact techniques like Lanczos are not subject to the sign problem. Using Lanczos or DMRG as the cluster solver, one could explore models with the sign problem, such as frustrated models, or spin liquid states, using NLCE.

Chapter 4

Conclusions

Entanglement scaling is a concept fundamental to the study of quantum many-body systems, that we have only been able to probe with the recent advent of large-scale simulation techniques for the measurement of Renyi entanglement entropies.

Important among these techniques (especially for 2D and higher) was the implementation of the “replica trick” into quantum Monte Carlo (QMC) in 2010 by the author and collaborators [25]. This paper has spawned a multitude of related studies, accruing 109 citations in approximately four years, and has inspired numerous researchers to adapt their own unique flavours of Monte Carlo to include this measurement [27, 31, 46, 51, 66, 78, 79, 88].

Additionally, in this thesis we have introduced a new method for studying the scaling of entanglement in quantum many-body systems using a numerical linked-cluster expansion (NLCE). We have simplified this technique by restricting the types of clusters used, generalized the traditional NLCE to allow for the adoption of any numerical cluster solver, and implemented measures for the Renyi entropies using Lanczos and DMRG. The combination of NLCE with QMC will be a powerful method for future studies and could compete with traditional finite-size scaling using toroidal lattices. Furthermore, this thesis has only shown the tip of the iceberg when it comes to NLCE. This technique can be used to study previously intractable problems such as those with the infamous “sign problem” preventing simulation through QMC. Even in cases where results diverge instead of converging, the numericist is still gaining information on how the state behaves as system sizes grow. Compared to other methods of finite size scaling (such as studying increasingly large toroidal systems) I believe one will find that the NLCE technique gives the most pristine view of the thermodynamic limit.

The simulation work contained in this thesis has shone light on key properties of the

scaling of entanglement in the interacting quantum many-body models studied. First, we have confirmed the leading-order “area law” scaling for spin systems, meaning that the Renyi entanglement entropies scale predominantly with the size of the boundary between the entangled regions. Second, this thesis has identified the subleading scaling terms to be of utmost importance in identifying and characterizing gapless phases of interacting models. For example, subleading logarithmic terms, with universal coefficients, can identify Goldstone modes in systems with continuous broken symmetry, or the presence of a corner in the entanglement boundary at a quantum critical point.

Such subleading terms will play a crucial role in future endeavours to use the entanglement entropy to identify and classify phases and phase transitions in many-body systems. An awareness of the terms discussed in this thesis is necessary to study any additional entanglement behaviour that might be uncovered in exotic condensed matter systems.

After perusing this thesis, the reader may be left to wonder whether the subject material is actually condensed matter, or quantum information. My answer is “both” and “neither”. In borrowing well established concepts from quantum information to construct an alternative and potentially more natural way of understanding phases in condensed matter systems, it is the manifestation of the emerging field of physics, quantum many-body theory, that relies on ideas and concepts from both.

References

- [1] Dmitry A. Abanin and Eugene Demler. Measuring entanglement entropy of a generic many-body system with a quantum switch. *Physical Review Letters*, 109:020504, Jul 2012.
- [2] Fabien Alet, Sylvain Capponi, Nicolas Laflorencie, and Matthieu Mambrini. Valence bond entanglement entropy. *Physical Review Letters*, 99:117204, Sep 2007.
- [3] K S D Beach and Anders W Sandvik. Some formal results for the valence bond basis. *Nuclear Physics B*, 750:142, 2006.
- [4] J. S. Bell. On the Einstein Podolsky Rosen paradox. *Physics*, 1(3):195–200, 1964.
- [5] Pasquale Calabrese and John Cardy. Entanglement entropy and quantum field theory. *Journal of Statistical Mechanics: Theory and Experiment*, 2004(06):P06002, 2004.
- [6] Pasquale Calabrese and John Cardy. Entanglement entropy and conformal field theory. *Journal of Physics A: Mathematical and Theoretical*, 42(50):504005, 2009.
- [7] John Cardy. The ubiquitous ‘c’ : from the Stefan–Boltzmann law to quantum information. *Journal of Statistical Mechanics: Theory and Experiment*, 2010(10):P10004, 2010.
- [8] John Cardy. Measuring Entanglement Using Quantum Quenches. *Physical Review Letters*, 106:150404, 2011.
- [9] H Casini. private communication. 2012.
- [10] H Casini and M Huerta. Universal terms for the entanglement entropy in 2+1 dimensions. *Nuclear Physics B*, 764(3):183–201, March 2007.

- [11] Xie Chen, Zheng-Cheng Gu, and Xiao-Gang Wen. Local unitary transformation, long-range quantum entanglement, wave function renormalization, and topological order. *Physical Review B*, 82(15):155138, October 2010.
- [12] Bob Coecke. Quantum picturalism. *Contemporary Physics*, 51(1):59–83, 2010.
- [13] Valerie Coffman, Joydip Kundu, and William K. Wootters. Distributed entanglement. *Physical Review A*, 61:052306, Apr 2000.
- [14] S Datta, N Limaye, and P Nimbhorkar. Planar graph isomorphism is in log-space. *Computational Complexity*, . *CCC . th Annual IEEE Conference*, 2009.
- [15] J. Eisert, M. Cramer, and M. B. Plenio. *Colloquium: Area laws for the entanglement entropy*. *Reviews of Modern Physics*, 82:277–306, Feb 2010.
- [16] Steven T. Flammia, Alioscia Hamma, Taylor L. Hughes, and Xiao-Gang Wen. Topological entanglement rényi entropy and reduced density matrix structure. *Physical Review Letters*, 103:261601, Dec 2009.
- [17] Eduardo Fradkin and Joel E Moore. Entanglement Entropy of 2D Conformal Quantum Critical Points: Hearing the Shape of a Quantum Drum. *Physical Review Letters*, 97:050404, August 2006.
- [18] Dimitri Gioev and Israel Klich. Entanglement Entropy of Fermions in Any Dimension and the Widom Conjecture. *Physical Review Letters*, 96:100503, 2006.
- [19] Ivan González. private communication. 2010.
- [20] Gaël Guennebaud, Benoît Jacob, et al. Eigen v3. <http://eigen.tuxfamily.org>, 2010.
- [21] C J Hamer and A C Irving. Cluster expansions in the (2+1)D Ising model. *Journal of Physics A: Mathematical and General*, 17(8):1649–1664, June 1984.
- [22] C J Hamer, J Oitmaa, and Z Weihong. Restoration of symmetry in the spectrum of the bilayer Heisenberg antiferromagnet. *Physical Review B*, 85, 2012.
- [23] Alioscia Hamma, Radu Ionicioiu, and Paolo Zanardi. Ground state entanglement and geometric entropy in the kitaev model. *Physics Letters A*, 337(1–2):22 – 28, 2005.
- [24] Matthew B Hastings. private communication. 2010.

- [25] Matthew B. Hastings, Iván González, Ann B. Kallin, and Roger G. Melko. Measuring renyi entanglement entropy in quantum monte carlo simulations. *Physical Review Letters*, 104:157201, Apr 2010.
- [26] Johannes Helmes and Stefan Wessel. Entanglement entropy scaling in the bilayer Heisenberg spin system. arXiv:1403.7395 [cond-mat.str-el], March 2014.
- [27] C. M. Herdman, P.-N. Roy, R. G. Melko, and A. Del Maestro. Particle entanglement in continuum many-body systems via quantum monte carlo. *Physical Review B*, 89:140501, Apr 2014.
- [28] Christoph Holzhey, Finn Larsen, and Frank Wilczek. Geometric and renormalized entropy in conformal field theory. *Nuclear Physics B*, 424(3):443 – 467, 1994.
- [29] Stephan Humeniuk and Tommaso Roscilde. Quantum Monte Carlo calculation of entanglement Rényi entropies for generic quantum systems. *Physical Review B*, 86:235116, 2012.
- [30] Stephen C Inglis. private communication. 2013.
- [31] Stephen C Inglis and Roger G Melko. Entanglement at a two-dimensional quantum critical point: a $T = 0$ projector quantum Monte Carlo study. *New Journal of Physics*, 15(7):073048, July 2013.
- [32] A C Irving and C J Hamer. Methods in hamiltonian lattice field theory (II). Linked-cluster expansions. *Nuclear Physics B*, 230(3):361–384, 1984.
- [33] Sergei V. Isakov, Matthew B. Hastings, and Roger G. Melko. Topological entanglement entropy of a bose-hubbard spin liquid. *Nature Physics*, 7(10):772–775, 10 2011.
- [34] Eric Jones, Travis Oliphant, Pearu Peterson, and Others. SciPy: Open Source Scientific Tools for Python. 2001.
- [35] Hyejin Ju, Ann B Kallin, Paul Fendley, Matthew B Hastings, and Roger G Melko. Entanglement scaling in two-dimensional gapless systems. *Physical Review B*, 85:165121, Apr 2012.
- [36] Ann B Kallin. Measuring entanglement entropy in valence bond quantum monte carlo simulations. Master’s thesis, University of Waterloo, 2010.

- [37] Ann B Kallin, Matthew B Hastings, Roger G Melko, and Rajiv R P Singh. Anomalies in the entanglement properties of the square-lattice Heisenberg model. *Physical Review B*, 84:165134, 2011.
- [38] Ann B Kallin, Katharine Hyatt, Rajiv R P Singh, and Roger G Melko. Entanglement at a Two-Dimensional Quantum Critical Point: A Numerical Linked-Cluster Expansion Study. *Physical Review Letters*, 110(13):135702, March 2013.
- [39] Ann B Kallin, E M Stoudenmire, Paul Fendley, Rajiv R P Singh, and Roger G Melko. Corner contribution to the entanglement entropy of an $O(3)$ quantum critical point in 2+1 dimensions. arXiv:1401.3504 [cond-mat.str-el], January 2014.
- [40] Alexi Kitaev and John Preskill. Topological Entanglement Entropy. *Physical Review Letters*, 96(11):110404, 2006.
- [41] V Korepin. Universality of Entropy Scaling in One Dimensional Gapless Models. *Physical Review Letters*, 92(9):096402, March 2004.
- [42] C Lanczos. An iteration method for the solution of the eigenvalue problem of linear differential and integral operators. *J. Res. Natl. Bur. Stand.*, 45(4):255–282, 1950.
- [43] Andreas M. Läuchli, Julien Sudan, and Erik S. Sørensen. Ground-state energy and spin gap of spin-1/2 kagomé-heisenberg antiferromagnetic clusters: Large-scale exact diagonalization results. *Physical Review B*, 83:212401, Jun 2011.
- [44] Michael Levin and Xiao-Gang Wen. Detecting Topological Order in a Ground State Wave Function. *Physical Review Letters*, 96(11):110405, 2006.
- [45] Yu-cheng Lin and Anders W Sandvik. Definitions of entanglement entropy of spin systems in the valence-bond basis. *Physical Review B*, 82(22):224414, December 2010.
- [46] Jeremy McMinis and Norm M. Tubman. Renyi entropy of the interacting fermi liquid. *Physical Review B*, 87:081108, Feb 2013.
- [47] Roger G Melko, Ann B Kallin, and Matthew B Hastings. Finite-size scaling of mutual information in Monte Carlo simulations: Application to the spin-1/2 XXZ model. *Physical Review B*, 82(10):100409, September 2010.
- [48] Max A Metlitski, Carlos A Fuertes, and Subir Sachdev. Entanglement entropy in the $o(n)$ model. *Physical Review B*, 80:115122, Sep 2009.

- [49] Max A Metlitski and Tarun Grover. Entanglement Entropy of Systems with Spontaneously Broken Continuous Symmetry. arXiv:1401.3504 [cond-mat.str-el], December 2011.
- [50] M A Nielsen and I L Chuang. *Quantum computation and quantum information*. Cambridge University Press, 2000.
- [51] Jiquan Pei, Steve Han, Haijun Liao, and Tao Li. The rényi entanglement entropy of a general quantum dimer model at the rk point: a highly efficient algorithm. *Journal of Physics: Condensed Matter*, 26(3):035601, 2014.
- [52] Roger Penrose. Applications of negative dimensional tensors. *Combinatorial mathematics and its applications*, (221244), 1971.
- [53] Didier Poilblanc and Norbert Schuch. Simplex \mathbb{Z}_2 spin liquids on the kagome lattice with projected entangled pair states: Spinon and vison coherence lengths, topological entropy, and gapless edge modes. *Physical Review B*, 87:140407, Apr 2013.
- [54] H Rieger and N Kawashima. Application of a continuous time cluster algorithm to the two-dimensional random quantum Ising ferromagnet. *The European Physical Journal B - Condensed Matter and Complex Systems*, 9(2):233–236, 1999.
- [55] Marcos Rigol, Tyler Bryant, and Rajiv R P Singh. Numerical linked-cluster algorithms. I. Spin systems on square, triangular, and kagomé lattices. *Physical Review E*, 75:061118, 2007.
- [56] Marcos Rigol, Tyler Bryant, and Rajiv R P Singh. Numerical linked-cluster algorithms. II. t-J models on the square lattice. *Physical Review E*, 75:061119, 2007.
- [57] Marcos Rigol, Rajiv R P Singh, and Tyler Bryant. Numerical Linked-Cluster Approach to Quantum Lattice Models. *Physical Review Letters*, 97(18):187202, November 2006.
- [58] Subir Sachdev. *Quantum Phase Transitions*. Cambridge University Press, 2011.
- [59] Anders W. Sandvik. Ground state projection of quantum spin systems in the valence-bond basis. *Physical Review Letters*, 95:207203, Nov 2005.
- [60] Anders W Sandvik. Computational Studies of Quantum Spin Systems. pages 1–204, 2010.
- [61] Anders W Sandvik. private communication. 2013.

- [62] Anders W Sandvik and K S D Beach. *Computer Simulation Studies in Condensed-Matter Physics XX*. Springer, Berlin, 2008.
- [63] Anders W Sandvik and H G Evertz. Loop updates for variational and projector quantum Monte Carlo simulations in the valence-bond basis. *Physical Review B*, 82(2):024407, 2010.
- [64] U. Schollwöck. The density-matrix renormalization group. *Reviews of Modern Physics*, 77:259–315, Apr 2005.
- [65] U. Schollwöck. The density-matrix renormalization group in the age of matrix product states. *Annals of Physics*, 326(1):96–192, 2011.
- [66] Alexander Selem, C. M. Herdman, and K. Birgitta Whaley. Entanglement entropy at generalized rokhsar-kivelson points of quantum dimer models. *Physical Review B*, 87:125105, Mar 2013.
- [67] Rajiv Singh. private communication. 2013.
- [68] Rajiv Singh. private communication. 2014.
- [69] Rajiv R P Singh, Matthew B Hastings, Ann B Kallin, and Roger G Melko. Finite-Temperature Critical Behavior of Mutual Information. *Physical Review Letters*, 106(13):135701, March 2011.
- [70] Rajiv R P Singh, Roger G Melko, and Jaan Oitmaa. Thermodynamic singularities in the entanglement entropy at a two-dimensional quantum critical point. *Physical Review B*, 86:075106, 2012.
- [71] H Francis Song, Stephan Rachel, and Karyn Le Hur. General relation between entanglement and fluctuations in one dimension. *Physical Review B*, 82(1):012405, July 2010.
- [72] Jean-Marie Stephan, Hyejin Ju, Paul Fendley, and Roger G Melko. Entanglement in gapless resonating-valence-bond states. *New Journal of Physics*, 15(1):015004, 2013.
- [73] E M Stoudenmire. private communication. 2014.
- [74] E M Stoudenmire, Ravi Johal, Ann B Kallin, and Roger G Melko. (in progress), 2014.
- [75] E M Stoudenmire and Steven R White. Studying Two-Dimensional Systems with the Density Matrix Renormalization Group. *Annual Review of Condensed Matter Physics*, 3(1):111–128, 2012.

- [76] L Tagliacozzo, G Evenbly, and G Vidal. Simulation of two-dimensional quantum systems using a tree tensor network that exploits the entropic area law. *Physical Review B*, 80:235127, 2009.
- [77] Baoming Tang, Ehsan Khatami, and Marcos Rigol. A short introduction to numerical linked-cluster expansions. *Computer Physics Communications*, 184(3):557 – 564, 2013.
- [78] Norm M. Tubman and Jeremy McMinis. Renyi entanglement entropy of molecules: Interaction effects and signatures of bonding. arXiv:1204.4731 [cond-mat.str-el], 2012.
- [79] Norm M. Tubman and D. ChangMo Yang. Direct calculation of the entanglement spectrum in quantum monte carlo with application to *ab initio* hamiltonians. arXiv:1402.0503 [cond-mat.str-el], 2014.
- [80] A M Turner, F Pollmann, and E Berg. Topological phases of one-dimensional fermions: An entanglement point of view. *Physical Review B*, 2011.
- [81] G Vidal. Class of Quantum Many-Body States That Can Be Efficiently Simulated. *Physical Review Letters*, 101(11):110501, September 2008.
- [82] G Vidal, J Latorre, E Rico, and Alexi Kitaev. Entanglement in quantum critical phenomena. *Physical Review Letters*, 2003.
- [83] L Wang, KSD Beach, and Anders W Sandvik. High-precision finite-size scaling analysis of the quantum-critical point of $S = 1/2$ Heisenberg antiferromagnetic bilayers. *Physical Review B*, 73, 2006.
- [84] Zheng Weihong. Various series expansions for the bilayer $S = 1/2$ Heisenberg antiferromagnet. *Physical Review B*, 55(18):12267–12275, May 1997.
- [85] Xiao-Gang Wen. Topological Order: From Long-Range Entangled Quantum Matter to a Unified Origin of Light and Electrons. *ISRN Condensed Matter Physics*, 2013:20, 2013.
- [86] Steven R White. Density matrix formulation for quantum renormalization groups. *Physical Review Letters*, 69(19):2863–2866, November 1992.
- [87] Christopher J Wood, Jacob D Biamonte, and David G Cory. Tensor networks and graphical calculus for open quantum systems. arXiv:1111.6950 [quant-ph], 2011.

- [88] Yi Zhang, Tarun Grover, Ari Turner, Masaki Oshikawa, and Ashvin Vishwanath. Quasiparticle statistics and braiding from ground-state entanglement. *Physical Review B*, 85:235151, Jun 2012.
- [89] Huan-Qiang Zhou, Thomas Barthel, John Ove Fjærestad, and Ulrich Schollwöck. Entanglement and boundary critical phenomena. *Physical Review A*, 74(5):050305, November 2006.